PolyPublie
Polytechnique Montréal

POLYTECHNIQUE MONTRÉAL
UNIVERSITÉ D'INGÉNIERIE

Titre: Title:	Optical Rotary Sensors for Avionic Applications
Auteur: Author:	Tahereh Ahmadi Tameh
Date:	2017
Type:	Mémoire ou thèse / Dissertation or Thesis
Référence: Citation:	Ahmadi Tameh, T. (2017). Optical Rotary Sensors for Avionic Applications [Thèse de doctorat, École Polytechnique de Montréal]. PolyPublie. https://publications.polymtl.ca/2524/

Document en libre accès dans PolyPublie
Open Access document in PolyPublie

URL de PolyPublie: PolyPublie URL:	https://publications.polymtl.ca/2524/
Directeurs de recherche: Advisors:	Raman Kashyap, & Mohamad Sawan
Programme: Program:	génie électrique

Ce fichier a été téléchargé à partir de PolyPublie, le dépôt institutionnel de Polytechnique Montréal
This file has been downloaded from PolyPublie, the institutional repository of Polytechnique Montréal

https://publications.polymtl.ca

UNIVERSITÉ DE MONTRÉAL

OPTICAL ROTARY SENSORS FOR AVIONIC APPLICATIONS

TAHEREH AHMADI TAMEH

DÉPARTEMENT DE GÉNIE ÉLECTRIQUE

ÉCOLE POLYTECHNIQUE DE MONTRÉAL

THÈSE PRÉSENTÉE EN VUE DE L'OBTENTION

DU DIPLÔME DE PHILOSOPHIAE DOCTOR

(GÉNIE ÉLECTRIQUE)

AVRIL 2017

© Tahereh Ahmadi Tameh, 2017.

UNIVERSITÉ DE MONTRÉAL

ÉCOLE POLYTECHNIQUE DE MONTRÉAL

Cette thèse intitulée:

OPTICAL ROTARY SENSORS FOR AVIONIC APPLICATIONS

présentée par: AHMADI TAMEH Tahereh

en vue de l'obtention du diplôme de: Philosophiae Doctor

a été dûment acceptée par le jury d'examen constitué de:

M. AKYEL Cevdet, D. Sc. A., président

M. KASHYAP Raman, Ph. D., membre et directeur de recherche

M. SAWAN Mohamad, Ph. D., membre et codirecteur de recherche

M. LAURIN Jean-Jacques, Ph. D., membre

M. AZAÑA José, Ph. D., membre externe

DEDICATION

To my love, Mehdi

To my parents

To my sisters

ACKNOWLEDGEMENTS

First, I would like to express my sincere gratitude to my thesis supervisors, Prof. Raman Kashyap and Prof. Mohamad Sawan, who gave me an opportunity to pursue the Ph.D. studies at the Polytechnique Montréal. This Ph.D. project could not be accomplished without their continuous support, their consistent encouragement, their inspiring guidance, and their extraordinary foresight.

I would like to thank Mr. Yann Le Masson from Bombardier and Mr. Franck Gansmandel from Thales for their wonderful mentorships.

I am also very grateful to all the personnel at the Poly-Grames Research Center, especially all the technicians including Mr. Jules Gauthier, Mr. Steve Dubé, Mr. Traian Antonescu, and Mr. Maxime Thibault. My gratitude extends to Mrs. Rachel Lortie for her assistance with all the administrative works and also to Mr. Jean-Sébastien Décarie for his technical support for solving all the IT problems.

My special thanks go to the members of the examination jury for reading my thesis and providing their invaluable comments.

I would like to thank all the colleagues in the Poly-Grames Research Center, in particular, Dr. Amirhossein Tehranchi and Dr. Jerome Poulin as well as NSERC-CREATE Integrated Sensor Systems (ISS) group at McGill University.

Last but not least, I would like to dedicate this thesis to my husband Seyed Mehdi Mozayan who was always by my side.

RÉSUMÉ

Cette thèse concerne des nouveaux capteurs optiques dédiés aux systèmes de contrôle de vol d'avions «fly-by-wire (FBW)». Les capteurs de déplacement sont utilisés dans les systèmes de contrôle de vol pour détecter la distraction du pilote, les déplacements de l'actionneur et ceux de la surface de vol. Actuellement, les capteurs « Rotary variable displacement transducers - RVDTs» utilisés dans les systèmes de contrôle de vol d'avions FBW sont les capteurs basés sur des circuits magnétiques et électroniques analogiques. Donc, une interface électronique est nécessaire pour la démodulation et numérisation des signaux reçus. Par conséquent, des paires de fils longs torsadés sont utilisés pour connecter le RVDT à l'ordinateur installé à bord de l'avion. Les paires de fils torsadés sont lourds et sensibles aux interférences électromagnétiques (IEM) et aux coups de foudre qui peuvent se produire pendant le vol. Nous proposons des capteurs optiques intelligents pour réduire le poids de l'avion, la consommation du carburant pour un environnement vert, l'IEM et pour utiliser moins de pièces métalliques afin de protéger davantage l'avion contre les coups de foudre.

La conception des encodeurs de capteurs optiques rotatifs (Optical rotation sensors - ORSs) est basée sur trois exigences importantes, soient la fiabilité, la linéarité, et l'exactitude de mesures. Ces capteurs intégrés dans le système de vol doivent être intelligents. Pour la fiabilité, la réponse du capteur est calculée à partir du ratio des deux puissances optiques ou celui de la différence divisée par la somme de ces deux puissances optiques. Cependant, pour la linéarité, la réponse du capteur consiste en une relation linéaire avec le paramètre à mesurer qui est l'angle de rotation. Quant à l'exactitude, l'erreur doit être moins de 1% sur toute la gamme de mesures. De plus, pour un capteur intelligent, le capteur basé sur des circuits analogiques, les convertisseurs au monde numérique et l'étape de démodulation doivent être emballés dans un boîtier commun.

Dans un premier prototype, un capteur de déplacement ratio-métrique, auto-référant, analogique et optique a été proposé pour les applications avioniques. La position de rotation est déterminée par le ratio de deux puissances lumineuses réfléchie et transmise qui rendent le capteur indépendant de fluctuations de puissance. L'encodeur multi-gradient original proposé compense pour l'usage d'une source non-uniforme.

En se servant d'un substrat en verre de format circulaire avec traitement antireflet, de diamètre extérieur de 27mm, nous avons réalisé le motif de l'encodeur par dépôt d'aluminium. Les résultats

expérimentaux montrent que le ratio des puissances transmise et réfléchie a une précision de 0.53% sur toute la gamme, correspondant aux spécifications des applications avioniques. En plus, il est expérimentalement prouvé que l'opération ratio-métrique n'est pas affectée pas le changement de la puissance de la source ce qui le rend fiable pour les applications avioniques. L'optimisation supplémentaire de design fera de ce type de capteur un excellent choix pour les futures applications nécessitant des capteurs de déplacement légers et écologiques.

Dans le second prototype, nous présentons un ORS auto-référé à large gamme. Pour atteindre la haute fiabilité requise pour l'utilisation aérospatiale, l'encodeur rotatif fonctionne en mode ratio-métrique ce qui le rend insensible à la variation de puissance de la source de lumière utilisée. Ce capteur a une plage de fonctionnement plus élevé que celui du RVDT actuellement utilisé dans les avions FBW. L'encodeur de l'ORS proposé est fabriqué sur un substrat de verre avec traitement antireflet en utilisent l'aluminium. Les résultats expérimentaux prouvent que la précision du capteur est de 0.8% sur tout le contour de 0° à 356.5°. Comparé au RVDT ayant une précision de 1% sur une plage de 80º, la plage d'opération de l'ORS proposé est au moins 4 fois meilleure que celle du RVDT. Nous avons prouvé également l'insensibilité du capteur contre les fluctuations de source, ce qui confirme qu'il est auto-référé.

Finalement, le premier prototype de notre ORS intelligent proposé pour les applications FBW est implémenté et utilisé pour détecter les changements au niveau du cockpit et le mouvement de surfaces de contrôle de vol. L'encodeur rotatif, le système optique, les circuits électroniques, et un microcontrôleur regroupant des convertisseurs analogique/numériques (ADC) sont assemblés dans un seul boitier de 80mm x 80mm x 50mm. Pour simuler les changements aux niveaux du cockpit et des surfaces de contrôle de vol, an actionneur est tourné à l'aide d'un ordinateur et les signaux résultants en sortie sont récupérés en utilisant le bus sériel universel (USB). Le traitement du signal nécessaire est fait en deux étapes; filtrage par logiciel et prélèvement de la puissance optique à partir des signaux mesurés et numérisés. Les résultats expérimentaux montrent que le capteur a une sensibilité de 17.5 mV/V/degré et une précision de 0.5% sur toute la gamme de 180º. En plus, nous avons testé la fiabilité du capteur en examinant sa réponse lors du changement de la puissance de la lumière appliquée à son entrée et nous avons démontré que ce capteur est très fiable, une exigence vitale pour les applications avioniques. Le capteur remplit les exigences d'applications avioniques, il requiert peu d'entretien, il est plus résistant aux IEM et il est très léger.

ABSTRACT

This thesis is on novel optical sensors for smart sensor system needed in flight control system (FCS) of fly-by-wire (FBW) aircraft. Displacement sensors are needed in FBW-FCS to detect pilot inceptors, actuator displacements, and flight control surface movement. Currently, the sensors used for rotary variable displacement transducers (RVDTs) are analog electronic sensors, hence an electronic interface is needed for demodulation and digitization of analog signals. As a result, long twisted wires are drawn from the sensor to the flight control computer (FCC) interface which are heavy and susceptible to electromagnetic interference (EMI) and lightning strike. By proposing smart optical sensors, we aim to reduce the aircraft weight to decrease the fuel usage towards a greener environment, reduce EMI, and protect the aircraft against a lightning strike by using fewer metallic parts.

The encoders of the optical rotation sensors (ORS) are designed based on three important requirements of reliability, linearity, and accuracy. In addition, they must be smart sensors to be integrated into the smart sensor system needed in FBW aircraft. For reliability requirements, the designed sensor response is the ratio of two optical powers or the ratio of the difference to the sum of two optical powers. For linearity requirement, the sensor response must be a linear relation with the measurand which is the rotation angle. For accuracy requirement, the error should be less than 1% over the full range. In addition, for a smart sensor, the analog sensor and the electronics for digitization and demodulation have to be packaged into a single housing.

In the first design, an optical, analog, self-referencing, ratio-metric, smart displacement sensor is proposed for avionic applications. The position of rotation is determined by an encoder by the ratio of the transmitted and reflected light powers, which makes the sensor independent of power fluctuations. A single multi-gradient encoder design compensates for the use of a non-uniform source. An anti-reflection coated glass window with the outer diameter of 27mm is used with an encoder pattern mapped on it using aluminum deposition. The experimental results show that the ratio of the transmitted and reflected powers has an accuracy of 0.53% over the full range, matching the specifications for avionic applications. It is also experimentally shown that the sensor operates ratio-metrically and is not affected by the change in the source power which makes it highly reliable

for avionic applications. Further optimization of the design will make this type of sensor an excellent choice for future lightweight and greener aircraft technology.

In the second design, we present a self-referenced broad range ORS for avionics applications. To achieve the high reliability required for aerospace use, the rotary encoder operates ratio-metrically to make it insensitive to source light power variation. This sensor has a larger operating range than RVDTs currently used in FBW aircraft. The ORS encoder is fabricated on an anti-reflection coated glass substrate with a reflective aluminum coating. Experimental results show that the sensor accuracy is 0.8% over the full rotation range from 0° to 356.5°. Compared to RVDTs, which have an accuracy of 1% over a full range of only 80°, the operating range of the proposed ORS is at least two times better than RVDTs. We also test the insensitivity of the sensor to source fluctuations which confirms that the sensor is self-referenced.

Finally, the first prototype of our proposed smart ORS for FBW applications is implemented and used to detect simulated cockpit inceptors or flight control surfaces movement. A rotary encoder, optical setup, electronic circuits, and a microcontroller with built-in analog to digital converters (ADCs), are assembled in a single housing with dimensions of 80mm x 80mm x 50mm. To simulate cockpit inceptors or flight control surfaces displacement, an actuator is rotated by a computer controlled driver and the output voltages are sent to the computer using a universal serial bus (USB). Signal processing is performed in two steps: software filtering and optical power extraction from the measured digitized voltages. Experimental results show that the sensor has the sensitivity of 17.5 mV/V/deg. and an accuracy of 0.5% over the full range of 180°. Moreover, we test the sensor reliability by examining the sensor response while changing the input power of the light source and we demonstrate that the sensor is highly reliable, a vital requirement for avionic applications. The sensor not only meets the requirements for avionic application but also it is smart which leads to less maintenance, less EMI, and huge weight reduction.

TABLE OF CONTENTS

LIST OF TABLES

LIST OF FIGURES

LIST OF SYMBOLS AND ABBREVIATIONS

AC	Alternating current
ADC	Analog to digital converter
AFCS	Automatic flight control system
AM	Amplitude Modulation
AOI	Angle of incidence
AR	Anti-reflection
COTS	Components off the shelf
EMI	Electro-Magnetic Interference
FBL	Fly-by-light
FBW	Fly-by-wire
FCC	Flight control computer
FCS	Flight control system
HF	High frequency
ISS	Integrated sensor system
LAN	Local area network
LD	Laser diode
LED	Light emitting diode
LPF	Low pass filter
LVDT	Linear variable displacement transducers
MAGFET	Magnetic field effect transistor
MEMS	Microelectromechanical systems
MOA	Minute of Angle
MR	Magneto-resistive

MTBF	Mean time between failures
OD	Optical density
OPAMP	Operational amplifier
ORS	Optical rotary sensor
PCB	Prototype circuit board
PCX	Plano-concave
PD	Photodiode
PM	Permanent magnet
PR	Photo-resist
RC	Resistance-capacitor
RMS	Root mean square
RPM	Revolution per minute
RVDT	Rotary variable displacement transducers
SNR	Signal to noise ratio
TIA	Trans-impedance amplifier
USB	Universal serial bus
UV	Ultra-violet
VHF	Very high frequency

CHAPTER 1 INTRODUCTION

1.1 Project overview

This research started in September 2012 in collaboration with a research and development project, AVIO402, related to the technological development plan of industrial partners, Thales Canada Inc., and Bombardier Aerospace Inc., for next generation avionic systems. For the first year, this project was funded by AVIO402. For the next two years, from September 2013 to August 2014, it was funded by the NSERC-CREATE training program in integrated sensor systems (ISS).

This project is in the design and fabrication of optical sensors for avionic applications especially for pilot input control applications, in particular, rotation and translation sensing in fly-by-wire (FWB) flight control systems (FCS). FCSs are operated based on position sensors for detecting pilot controls, actuator displacements, and flight control surfaces movement. The sensors currently used in FCS are fully analog Rotary/Linear Variable Differential Transducer (R/LVDT) working on electromagnetic principles. Therefore, it is expected that the optical equivalent smart position sensors will be used to connect to high-performance standard digital avionics data buses to get rid of heavy electrical wiring cables between sensors and the flight control computer (FCC). In responding to these technological challenges, this project aimed to develop lightweight and high-reliability optical displacement sensors to replace the current position sensors to provide enhanced performance while reducing the cost of deployment and maintenance. Therefore, smart sensor requirements for avionic systems have been considered in the research presented here.

In the following section, a short introduction to FCS will be presented in order to know where the rotation sensors are used in this system.

1.2 Introduction to FCS

FCS is responsible for control of actuators in flight control surfaces [1] such as rudders and elevators in the tail and ailerons in the wings of aircraft. Movement of certain flight control surfaces results in changing of aerodynamic force and consequently alteration of aircraft's attitude in relation to three axes: yaw, roll, and pitch [1]. Aircraft axes are shown in Figure 1.1 and explained as follows:

- Roll axis is for turning around the longitudinal axis.
- Yaw axis is for turning right and left.
- Pitch axis is for taking off and landing.

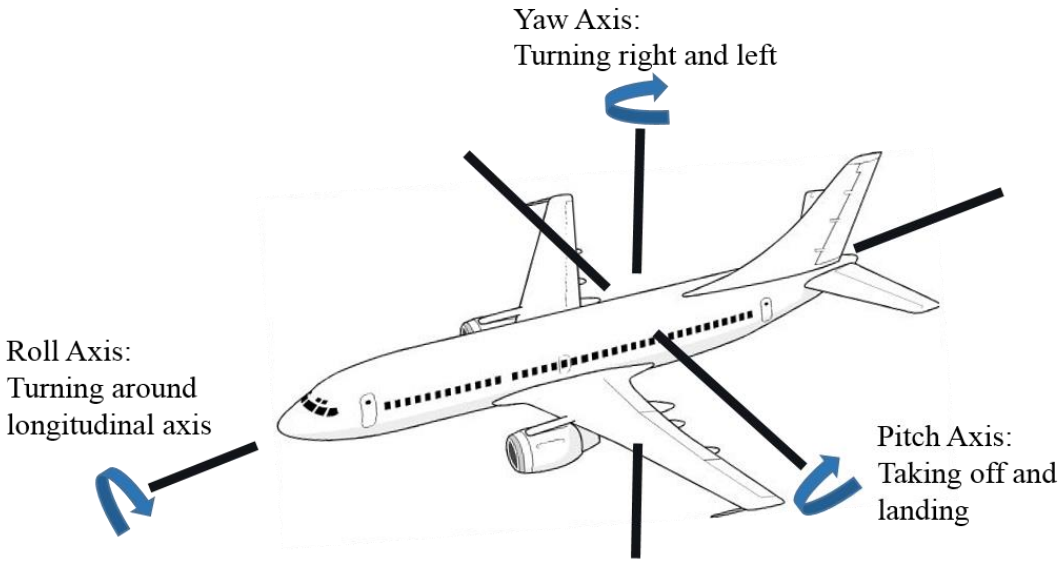

Figure 1.1 Three axes of an airplane[1].

To manipulate three axes of aircraft, different flight control surfaces should be displaced in the right position. Ailerons, rudders, and elevator, shown in Figure 1.2, should be controlled to adjust roll, yaw, and pitch axes, respectively.

Conventional FCS applies hydraulic actuators and control valves by cables that pass the length of the airframe [2]. The disadvantage of this hydraulic cable-controlled system is the weight of long cables which result in a heavy aircraft. However, FBW airplanes apply electronic displacement sensors in which the analog signals from the sensor are sent to the FCC interface. Hence, analog signals are processed in FCC interface which consumes lots of pins on connectors and board surface [3]. The solution to this challenge is a smart sensor in which the corresponding electronics for demodulation and digitizing processes of analog signals should be removed from FCC and

[1] http://drawingimage.com/files/3/Airplane-Amazing-Drawing.jpg

packed with the sensor itself in a compact housing [3]–[5]. Conventional FCS, FBW FCS, and fly-by-light FCS are explained in the following sections.

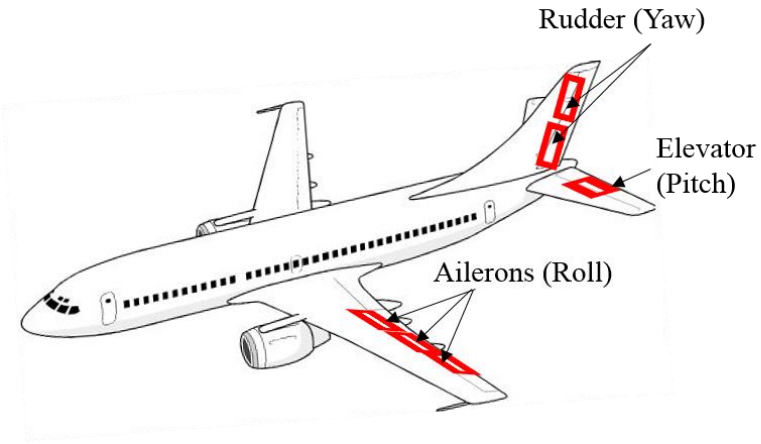

Figure 1.2 Primary flight control surfaces[2].

1.2.1 Conventional FCS

Early airplanes - such as Boing 727 in the early 60's and Boeing 737 in 1967 [6] - used mechanical FCS [7] shown in Figure 1.3. In a conventional FCS, the pilot command in the cockpit inceptors (such as rudder pedals, spoiler handle, flap handle, etc.) is transferred through a mechanical transmission system of cables and pulleys to the actuators which influence flight control surfaces in the wing or tail of the aircraft. Heavy cables and pulleys pass along the aircraft from cockpit in the nose of the airplane to the actuator in the tail or wing resulting in a heavy load and non-integrated FCS.

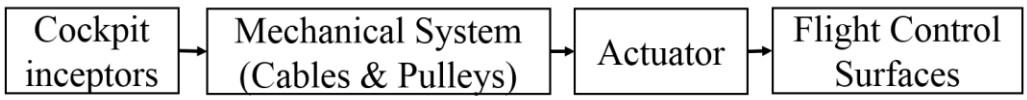

Figure 1.3 Conventional FCS in which cables and pulleys are used to transfer captain command in the airplane nose to actuators in flight control surfaces.

[2] http://drawingimage.com/files/3/Airplane-Amazing-Drawing.jpg

An example of conventional FCS for elevator control using cables and pulleys is shown in Figure 1.4.

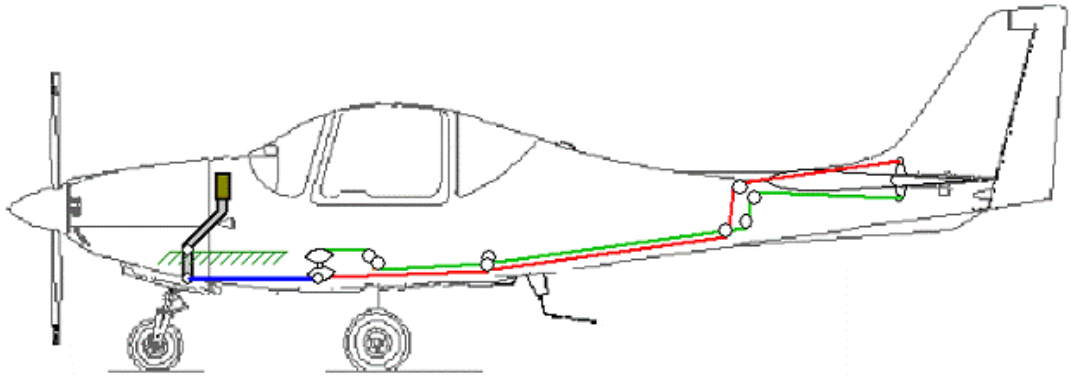

Figure 1.4 Conventional FCS of cables and pulleys[3].

1.2.2 FBW FCS

The FBW-FCS was proposed as an evolutionary step for FCS. A well-known example of an aircraft with FBW-FCS is the Boeing 777 delivered to United Airlines in 1995 [6]. Another example is the Airbus A320 which made its first flight in 1987 [1]. Other examples are the Airbus A330, A340, A380, and the Boeing 787 [8]. In FBW-FCS, the mechanical control system is replaced by the electronic control system to reduce the aircraft weight and integrate the systems. Hence, displacement sensors were required to convert mechanical signals (Pilot commands) to the electrical signals which have to be sent to the FCC. The processed signals from FCC are sent to the actuators in flight control surfaces and automatic flight control system (AFCS) [9].

It is worth noting that in comparison to conventional FCS, FBW system uses wires to send/receive data between cockpit, FCC, and actuators in flight control surfaces resulting in impressive weight reduction and integrated system [2]. Another major benefit of FBW-FCS is the ability to tailor the system's characteristics at each point in the airplane [1].

An example of FBW-FCS is shown in Figure 1.5 to clarify how a command in the cockpit is transferred to the elevator in the tail of airplane to adjust pitch angle while taking off or landing.

---

[3] https://pritamashutosh.wordpress.com/2012/11/17/flight-control-system/

The captain command (mechanical signal by displacing elevator handle) is converted to the electrical signal through a transducer which sent to FCC-interface for demodulation and digitization. The digitized signal is sent to FCC for processing. The processed signal is sent to actuator electronics and then to the elevator actuator in the flight control surface.

Position sensors are used in this system for one of the following applications:

1. Pilot input controls: the position of cockpit inceptors such as such as sidesticks, conventional columns-wheels, rudder pedals, spoiler handle, and flap handle, etc.
2. Actuator displacements near to flight control surfaces
3. Flight control surfaces movement

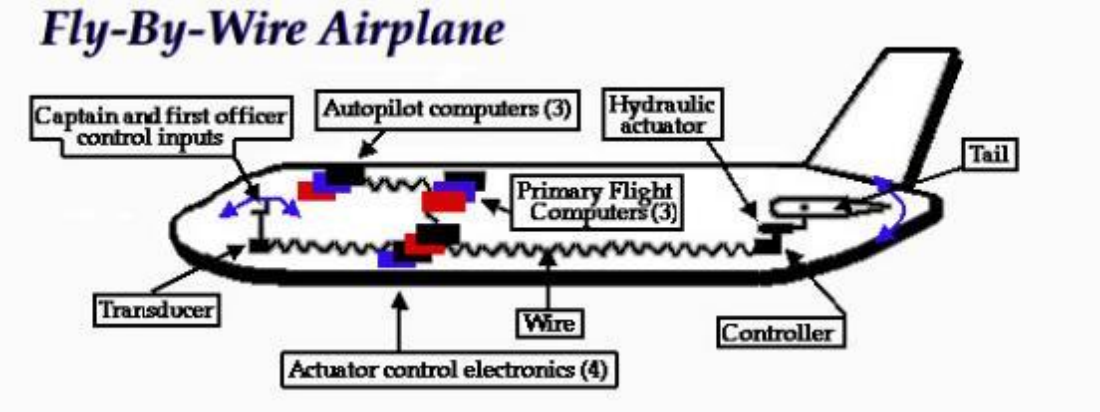

Figure 1.5 an example of FBW-FCS to adjust elevator position[4].

1.3 Motivation

Block diagram of FBW-FCS is shown in Figure 1.6 in which captain command is converted to an electrical signal through a displacement sensor, rotary/linear variable differential transformer (RVDT/LVDT). The analog signal is sent to FCC interface for demodulation and digitization and thus, the produced digital signal is sent to FCC. The processed command from FCC is sent to actuator electronics and consequently to the actuators moving flight control surfaces. This block

[4] http://www.mura.org/mura.org/websites/me39c.me.berkeley.edu/Spring97/Projects/b777/flightdeck2.html

diagram clearly shows that the signals between cockpit, FCC, and flight control surfaces are communicated by wires.

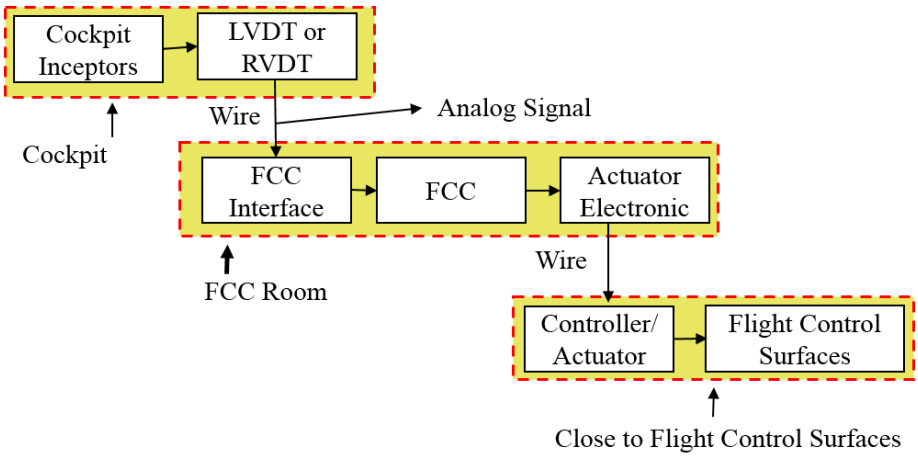

Figure 1.6 block diagram of FBW-FCS. FCC: flight control computer, LVDT: linear variable differential transformer.

Smart sensor concept: In the next step of flight control evolution, it is desired to receive condition of FCS over a digital link in FCC. Thus, the analog sensor and its related electronics should be packed in a single housing. As shown in Figure 1.7, the output of the smart sensor is sent directly to FCC via a bus and thus there is no need to FCC interface.

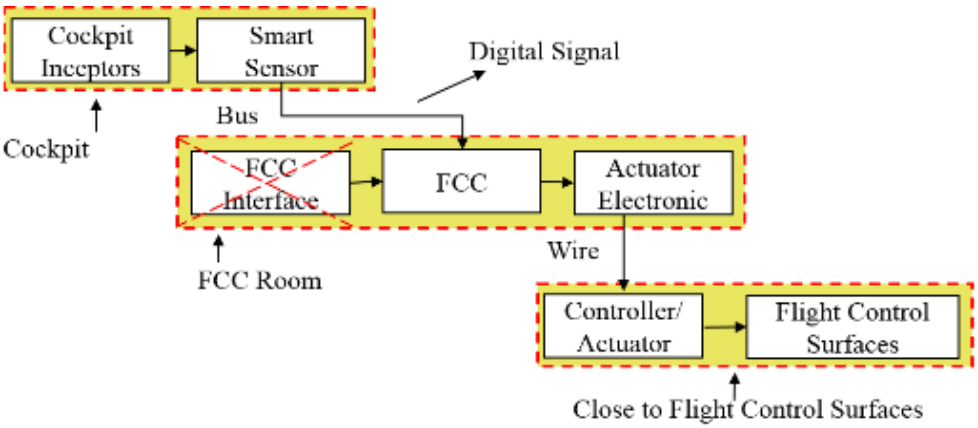

Figure 1.7 Smart sensor in FCS.

In an FBW system, there are 29 RVDT/LVDT in the cockpit, in one example, and each has usually 5 wires resulting in the total number of 145 wires as reported in [3]. However, the outputs of smart sensors are sent to FCC via only 4 buses [3] in a control system with smart sensors. Smart sensor system not only results in reducing the weight but also integrating the FCS.

Based on the request of industry parties and with the enormous advances made in the field of photonics, we are going to use a simple analog coding encoder system to implement angular position sensing with low weight, low cost, high reliability and resolution in the avionic system.

1.4 Contributions in this Thesis

New analog optical rotation sensors have been designed, fabricated, and tested for avionic applications. Following contributions have been made:

- Two different NEW rotation encoders have been designed to propose various operating ranges and sensitivities as these two parameters are in a trade-off with each other. In the first one, the sensitivity is higher while in the second one the operating range is broader.
  - The first one which is based on the ratio of reflected and transmitted powers has a high sensitivity.
  - The second one has a broader operating range but lower sensitivity, the sensor response is obtained from the ratio of subtraction to summation of reflected and transmitted powers.
- The sensors are SIMPLE: In order to propose a simple sensor, the number of components is minimized and they are selected from the available components in the market. In addition, the design of rotary encoder and consequently its fabrication are not complicated. These simplifying approaches are explained as follows:
  - ONLY one laser diode and two photodiodes are used for the source and detection, respectively.
  - The optical setup is designed to use components off the shelf (COTS) and there is no need to design special lenses which result in increased cost.
  - The design of the rotary encoder is simple in comparison to the optical digital rotary encoders on the market (details in Section 2.6). As a consequence, fabrication procedure is not complicated and the accuracy of microfabrication technology is enough to meet the final accuracy requirements of avionic applications.

- The sensor is RELIABLE: To deliver reliable sensors for avionic applications, they should be self-referencing and self-calibrating. Hence, the pattern of rotary encoders are designed to meet these requirements as explained as follows:

  - Self-referencing: the sensor response is obtained from the ratio of two powers (or the ratio of subtraction to the summation of two powers). Hence, the effect of source fluctuation and aging is canceled in the ratiometric sensor response. In addition, having two photodiodes with the same silicon material, two powers at the detection side are aged approximately equal and cancel each other's effect in the ratio-metric sensor response.

  - Self-calibrating: Multi-patterned-rings design has been used to overcome the problem of the non-uniform source. All optical sources are non-uniform by their nature. Moreover, high order modes could appear by aging. Using multi-patterned-ring design, one can assume the source is uniform in each subring.

- The sensors are SMART: In order to propose a smart sensor, all parts of the sensor including optical and electrical components and the rotary encoder mask on the shaft have been packed into a single housing and the digitized signals are sent to the computer via a bus. Applying smart sensor in an aircraft results in wire removal between sensor and FCC and replacing it with Buses and removal of related electronics in the FCC interface for digitization and demodulation of the analog signal. These two improvements result in:

  - Low maintenance: cable management between sensor and FCC would be easier and with the lower cost because of replacing more than 100 wires with 4 buses.

  - Low EMI: buses are less sensitive to EMI in comparison to wires

  - Low weight: With a lighter aircraft, the rate of fuel consumption is decreased which is followed by an increase in the range, the distance an aircraft can fly between takeoff and landing. Another effect of lower weight could mean more cargo or passenger handling.

- Small footprint: more space will be available by replacing of wires with buses and removal of electronics related to sensors in the FCC interface.

– The sensors consume LOW POWER: the power consumption on the source side and detection side are verified as follows:

- The power consumption of the source to drive the laser diode is 40mA×9V=360mW.
- The power consumption in the detection side in photodiode detection circuits is 16mW. As the total optical power is 1mW, the maximum photocurrent produced by a silicon photodiode is 0.5mA. The voltage to drive the op-amps is -16V to +16V. Hence, the total power consumption on the analog detection side is 16mW. In the digital part, the voltage and current on the board are 3.3V and 0.5mA resulting in a power consumption of 1.7mW.
- The total power requirement is less than 0.5 watt including the power on the detection side, analog and digital.

1.5 Research objectives

It is expected to design optical sensors which measure the rotation angle and works linearly. It should be fabricated from a piece of glass which is light and cheap. Moreover, for producing the beam, an optical setup including LD should be used which is an incoherent and inexpensive source. In addition, an optoelectronic circuit should be designed and fabricated to convert the light into voltage. So at the end, we hope to design and make an optical sensor which has a lot of benefits over current electronic sensors.

1. **Literature review in optics, optical sensors, and optical rotation sensors**
   In this section, a literature survey of optical elements such as a laser, LD, and PD is required. In addition, taking courses of fundamentals of photonics and optical engineering is needed. Moreover, it is indispensable to be familiar with principles of sensing and classification of optical sensors. (It is done, could be improved)
2. **Making a proper beam using lenses and LED:** In this section, it is necessary to be familiar with choosing and ordering proper elements such as lenses, mounts, and LDs.

Getting practical knowledge about characterizing, mounting, and making a proper beam should be obtained. (It is done, could be improved)

3. **Design, simulation, and fabrication of mask for rotation sensor:** In this section, the design of the encoder masks based on the principles of sensing should be done. Using software such and Matlab and Solidworks for simulation and drawing the encoder mask is needed. Finally, it is required to fabricate them. (one sample is designed and fabricated)
4. **Design, simulation and making detecting electronic circuits:** In this part, design and simulation of the electronic circuit are required to convert the optical signal to the electronic signal such as voltage and current. In the next step, the electronic circuit should be implemented.
5. **Testing:** In this section, after implementing the optical and electronic parts, the whole setup of the optical sensor should be tested. (first fabricated sample is tested which shows the design works but it should be re-fabricated to resolve some problems)
6. **Making a housing:** In this section, housing for the optical elements such as lenses and LD should be designed and fabricated. (Solidworks should be applied and student is familiar with it now)
7. **Deliverables:** In this part, the results of design and fabrications are published as conference and journal papers. It was also necessary to deliver reports to the industrial partners by the end of each phase. Moreover, at the end of the Ph.D. journey, the dissertation should be written.

1.6 Thesis outline

The remainder of this thesis is structured as follows: In Chapter 2, a literature review of different rotation sensors and their characteristics will be presented with a specific emphasis on current optical rotary sensors (ORSs) in the market and rotary sensors currently used in the avionic application. In Chapter 3, rotary encoder design principles are presented as well as its drawing and fabrication procedure. This Chapter also includes optical and mechanical setups and test approaches. In Chapter 4 and 5, analog optical rotary encoders with the operating range of 0º to 180º and 0º to 356.5º will be presented, respectively. In Chapter 6, the prototyping procedure of smart sensor will be presented. Finally, in Chapter 7, one can find the conclusion and future works.

CHAPTER 2 LITERATURE REVIEW: ROTATION SENSORS

Rotary sensors are key components in several systems, such as motion capture devices [10]–[11], industrial control application to monitor rotation of mechanical parts [10], [12]–[14], and automotive sensors for tracking steering-angle [10], [15], [16]. Rotary displacement sensors are widely employed in FBW aircraft and avionics systems for flight control purposes [2], [3], [17], [18].

A variety of technologies and approaches can be applied to measure rotary displacement [13], [19]. Magnetic rotation sensors, potentiometers, resolvers/synchros, MEMS-based rotation sensors, and Gyro-based rotation sensors are briefly explained in the following sections followed by their advantages and disadvantages. In addition, two important categories of rotation sensors are verified, optical rotation sensors in the current market and rotary variable displacement transducers (RVDTs) currently used in FBW avionic applications. Finally, all sensors and compared with each other and their potential for avionic application are discussed.

2.1 Magnetic rotation sensors

2.1.1 Working principle

The rotation angle is encoded into the magnetic flux in magnetic rotation sensors such as magneto-resistive, Hall Effect, and magnetic encoders [13]. As a magnetic flux is a vector quantity, magnetic sensors may measure the total magnitude (ex: Hall Effect devices) or angle direction of a magnetic field (ex: magneto-resistive devices).

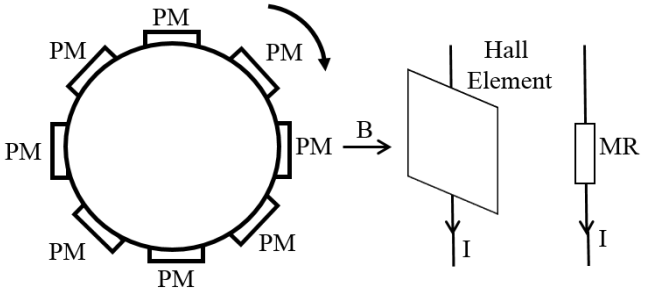

Figure 2.1. Magnetic sensor. PM: Permanent magnet, MR: Magneto-resistive, I: electric current.

In these sensors, rotation angle modulated into the magnetic flux is converted to the electrical signal by means of Hall elements [16] or magnetic resistance (MR) as shown in Figure 2.1. Hall Element

is a thin sheet of conductive material with connections perpendicular to the direction of current flow and MR device has a resistance changing with the applied magnetic field.

The principle of working of magnetic rotation sensors is displayed in the format of the block diagram in Figure 2.2.

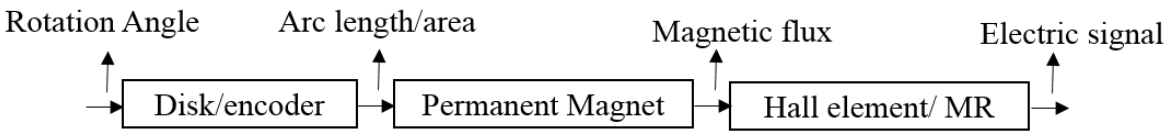

Figure 2.2. The principle of working (Magnetic rotation sensors).

2.1.2 Pros and Cons

Magnetic sensors could be used in hot and dirty environments and they are known for their infinitesimal resolution, and robust and solid construction [20]–[22]. In addition, they are very rugged, suitable for small-lot production [15], high-speed operation (100kHz) [23]

However, external electromagnetic interference (EMI) can seriously affect the sensor response due to intrinsic operation of magnetic sensors having a high sensitivity to magnetic flux [13]. In addition, the output of a magnetic sensor requires some signal processing (ex: linearization) to translate the sensor output into the desired parameter value.

2.2 Resistive rotation sensors

2.2.1 Working principle

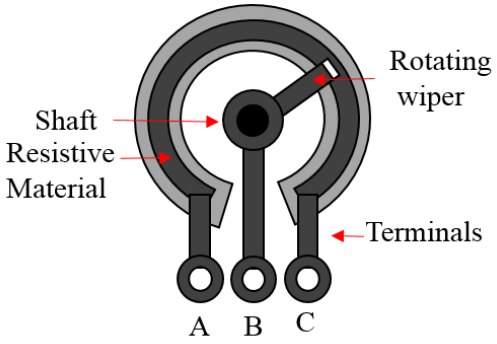

Figure 2.3 Resistive rotary sensor (Resistive rotation sensors).

Potentiometer or pots are the common terms used for resistive displacement sensors [13]. By rotating the shaft of a potentiometer, the length and consequently the resistance of the internal resistor is increased resulting in the modulation of rotation angle into the resistance (Figure 2.3).

Working principle of resistive rotation sensors is displayed in the format of the block diagram in Figure 2.4.

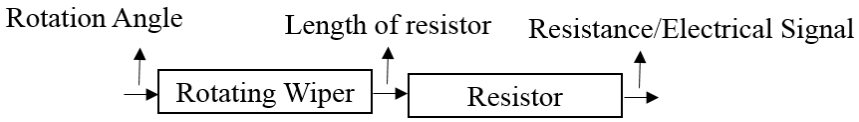

Figure 2.4. The principle of working (Resistive rotation sensors).

2.2.2 Pros and Cons

Potentiometers are low-cost, simple, and EMI resistant.

However, they suffer from the eventual wear-out due to the sliding contact wiper with the resistive material [19].

2.3 Resolver and synchro

2.3.1 Working principle

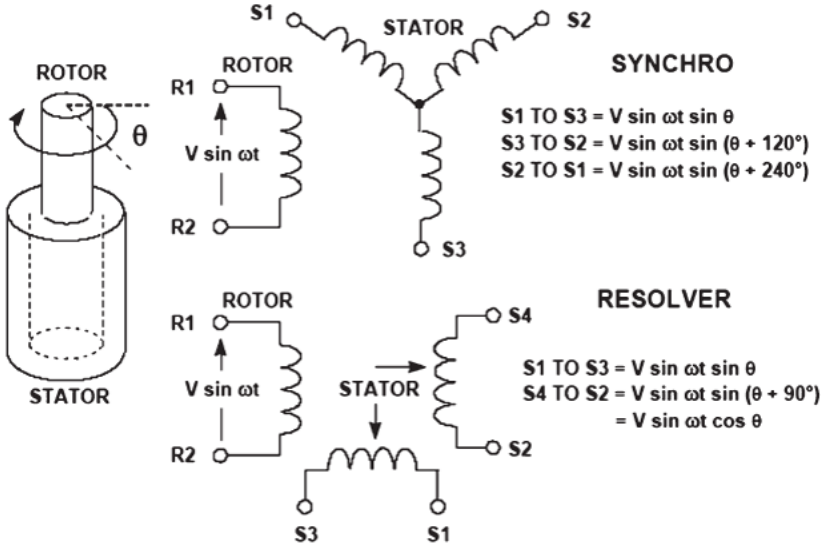

Figure 2.5: Resolver and synchro [19].

Resolver and synchro are shown in Figure 2.5. In synchro, a primary coil (in the rotor) is excited by an AC signal. Electric signals are inducted into the secondary coils which have the angle 120º with each other with the rotation of the rotor. In resolvers, two secondary coils have the angle of 90º with each other.

Resolvers and synchros have the same principles as RVDTs with the only difference that the transfer coils are fixed in RVDT. Unlike RVDTs, they are multi-turn with the full operating range [19].

Working principle of resolvers/synchros is displayed in the format of the block diagram in Figure 2.6.

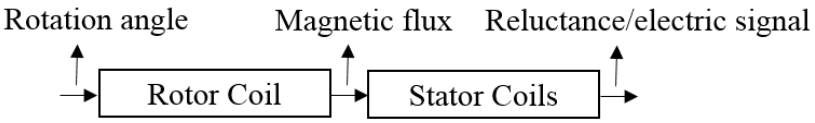

Figure 2.6. The principle of working (Resolvers/synchros).

2.3.2 Pros and Cons

Resolvers/synchros are very robust and have the capability of working in dirty environments.

However, the need for an AC signal source is the weak point of these sensors [24].

2.4 Rotation sensor based on MEMS

2.4.1 Working principle

Various approaches could be taken to measure rotation angle by MEMS such as capacitive, piezoelectric, piezo-resistive, magnetic, and optical categories [25]. However, the capacitive MEMS are the most spread ones. MEMS devices do not measure the angle directly. In reality, MEMS accelerometers and gyroscope MEMS are used for measurement of rotary displacement

The accelerometer MEMS used in iPhone measure the projection of the gravity vector on the sensitive axis as shown in Figure 2.7. The angle of rotation, α, is calculated as Eq. 2.1

$$\alpha = \arcsin(A / g) \qquad \text{Eq. 2.1}$$

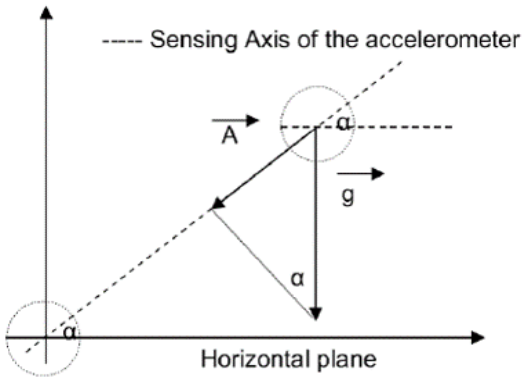

Figure 2.7 MEMS accelerometer for rotation angle measurement. Vector A shows the projection of the gravity vector on the sensitive axis.

where *g* is acceleration due to gravity and vector A is the projection of gravity vector on the sensing axis. Hence, these types of MEMS are practical in the devices with negligible acceleration in comparison to the gravity. For example, it could be used in iPhone but cannot be used in the airplanes which have acceleration while landing and taking off. In the case of using an accelerometer for angle measurement, the gravitational components should be extracted from the total acceleration components. Hence, an information measurement unit (IMU) should be used containing certain sensors such as inertial sensors [26].

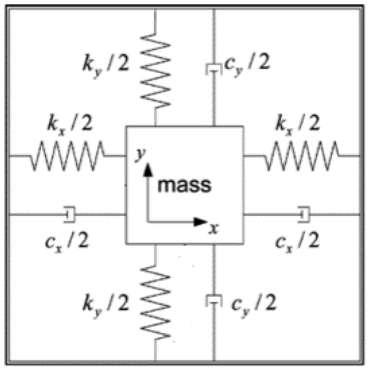

Figure 2.8 MEMS Gyroscope: mass suspended by use of four springs, $k_{x/y}$ *and* $c_{x/y}$ are spring constants and damping factors, respectively [27].

Another MEMS development could be applied for angle measurement is MEMS Gyroscope [27], [28]. In this approach, as shown in Figure 2.8, the angle of free vibration of a mass suspending by

elastic members is measured. When sensor experiences an external angular velocity, the angular velocity is modulated into vibrating positions (*x* and *y*) of suspending mass. Hence, by demodulating of positions, the angular velocity is obtained. Angular displacement is attained by integration of angular velocity over the time in which the error in each time will be accumulated resulting in a high error.

Working principle of MEMS is displayed in the format of the block diagram in Figure 2.9.

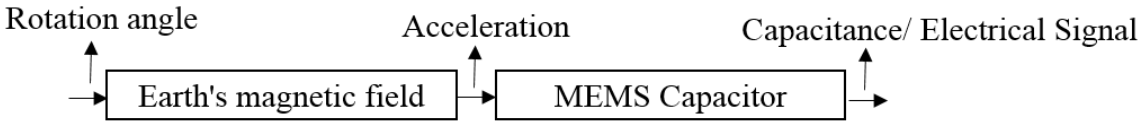

Figure 2.9. The principle of working (MEMS).

2.4.2 Pros and Cons

MEMS have a small size in the range of μm with the final package in the range of mm. Nonetheless, this positive makes these kinds of sensors incompatible for avionic applications.
However, it is not standardized yet. In addition, fabrication procedure is time-consuming [29]. Moreover, small imperfection has a huge impact on the performance of these sensors [27].

2.5 Rotation sensor based on Gyro

2.5.1 Working principle

Gyroscopes work based on inertia law stating an object at rest stays at rest and an object in motion stays in motion. Hence, when the spinning part of gyroscope spins at high speed, it tends to keep the direction of its axis. There are three types of gyroscopes: spinning mass, optical, and vibratory [30]. Spinning mass gyroscopes have a mass spinning continually. Optical gyroscopes [31] works based on Sagnac effect stating phase shift between two waves counter-propagating in a rotating ring interferometer is proportional to the loop angular velocity. Vibrating gyros are based on Coriolis effect that induces a coupling between two resonant modes of a mechanical resonator [30].

Gyros measure angular velocity. The angular velocity could be integrated over the time to find the rotation displacement. Consequently, small errors in each time will be accumulated and resulted in a big error in the angle measurement [27], [32].

Working principle of Gyros is displayed in the format of the block diagram in Figure 2.10.

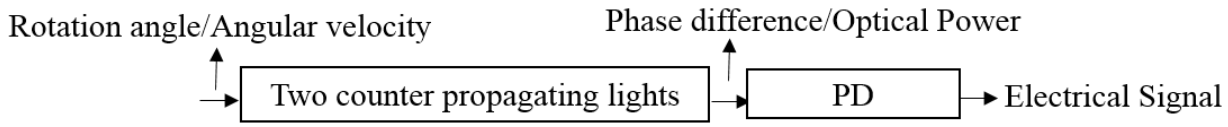

Figure 2.10. The principle of working (Gyro).

2.5.2 Pros and Cons

Gyros are excellent devices for angular velocity measurement.
However, error accumulation for rotary displacement measurement and being bulky and expensive are disadvantages of Gyros [26]

2.6 Optical rotation sensors

Optical sensors include a variety of devices, all of which use light as the means to transform displacement into electrical signals [13]. They have attracted a lot of attention in biomedical sensing [33], [34], structural monitoring [35], gas sensing [36], [37], humidity sensing [38], mining [39], renewable energies to assess quality of biodiesel [40], bio/chemical sensing [33], [41] and avionic [42]–[44]. Optical sensors not only are accurate, light and small but also have high speeds and high resolution [16], [45]. However, optical sensors are susceptible to dirty environment and lose performance at higher temperatures (greater than 70°C) because of the intrinsic properties of the photodiodes and laser diodes commonly used as receivers. Moreover, the fine target structures of high-resolution optical sensors can be easily affected by mechanical shock and vibration.

Different types of optical rotation encoder sensors in terms of the principle of working and the scheme are explained in the following sections.

2.6.1 Different types of optical rotation sensors (Working principle)

Optical rotary encoder sensors found in the literature to date are mainly digital [10], [12], [46]–[49] which work just based on the reflected or transmitted power. Working principle of optical rotation sensors is displayed in the format of the block diagram in Figure 2.11.

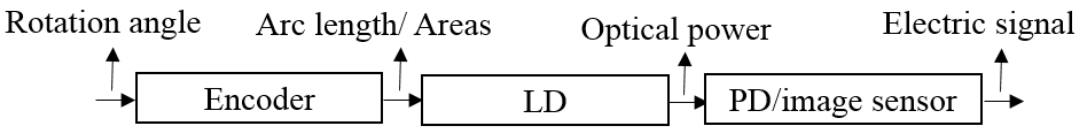

Figure 2.11. The principle of working (Optical rotation sensors).

2.6.2 Different types of optical rotation sensors (Schemes)

Two schemes can be applied to the rotary encoder [49], incremental and absolute.

In the incremental encoder, the displacement is detected relative to a reference point [13]. Consequently, some form of the reference signal in needed in order to define a reference position. The current position thus is decremented/incremented as appropriate [13]. Figure 2.12 shows incremental rotary encoder [50].

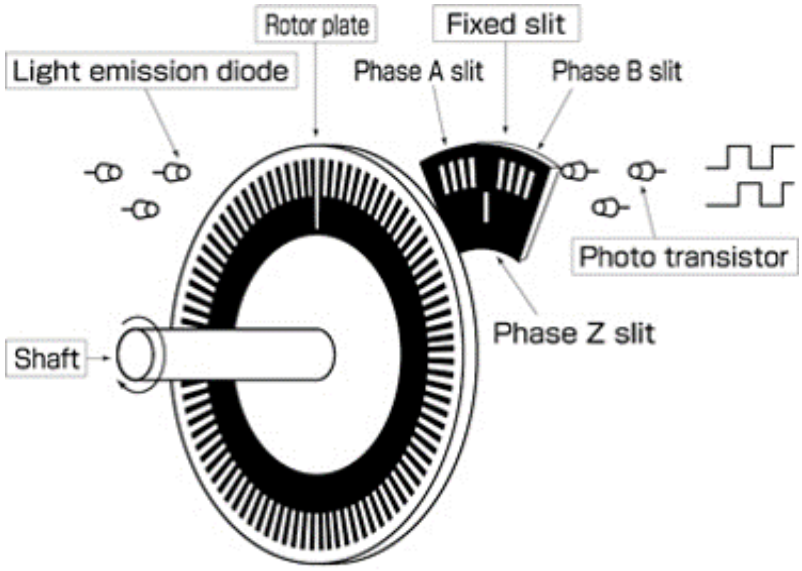

Figure 2.12: Incremental rotary encoder [50].

Figure 2.13 shows absolute rotary encoder [50] in which the position of the disk is detected absolutely from a set of binary signals [13]. It is a very complicated method and consequently, it is difficult to make a high accuracy disk [49].

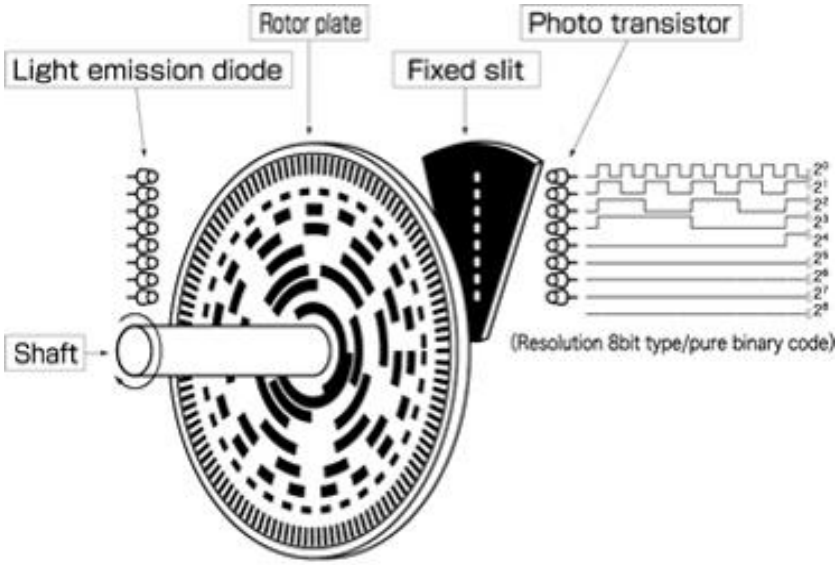

Figure 2.13 Absolute rotary encoder [50].

2.6.3 Pros and Cons

There are many advantages for optical rotary encoder sensors. They are small and light [16] with high speed and high resolution (even 0.001º).

However, the encoder design is complex [45]. They contain numerous parts such as several light sources [51]. In the detection side, an array of photodiodes or an image sensor is used; therefore, to decode the measurand from the measured signals, complex signal processing should be done in the detected scheme [12]. Certain systems include image sensors [10], [52], [53] in which the properties of the image sensor and image processing system are needed to decode the response of sensor from the coded information. In addition, they work solely on transmitted light [54], reflected light [51], [52], or diffracted light [14] making the sensor susceptible to source power fluctuation. Moreover, preliminary calibration and self-calibration circuits are used to solve the problem of nonlinearity coming from the non-uniform light source and power reduction of the source which makes the sensor complex. All of these characteristics make these kinds of sensors very expensive and inappropriate for small-lot production [15].

2.7 RVDT

2.7.1 Working principle

Electromagnetic induction is the basic principle of RVDTs. As shown in Figure 2.14, a primary coil is excited with a carrier signal and movement of the ferromagnetic core within the flux path results in a change of second coils reluctance. Consequently, the rotation angle is modulated into the differential amplitude of the secondary coils [13]. RVDTs currently used in FBW-FCS [3].

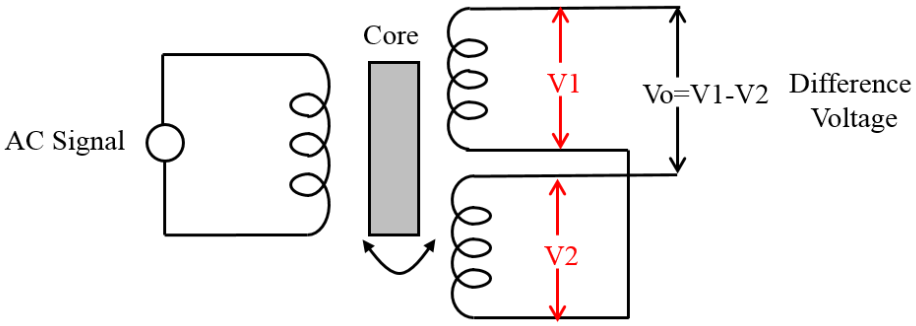

Figure 2.14 RVDT, AC: Alternating current.

Working principle of RVDTs is displayed in the format of the block diagram in Figure 2.15.

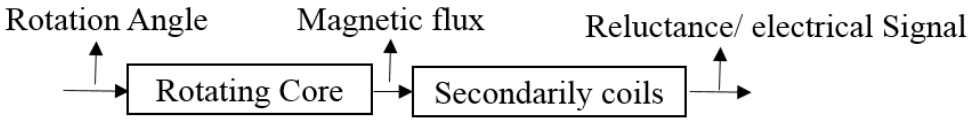

Figure 2.15. The principle of working (RVDTs).

2.7.2 Pros and Cons

RVDTs work based on ratiometric sensor response resulting in a high reliability. In addition, they are compact [13] and the infinitesimal resolution and robust and solid construction are possible with these kinds of sensors [20]–[22].

However, a typical linear range of measurement of RVDT is about -40º to +40º with a nonlinearity error of about 1% [13], [20]; to increase the range, the sensor response is no longer linear [55]. Moreover, external EMI can seriously affect the sensor response as the intrinsic operation of inductive sensors has a high sensitivity to magnetic flux [13]. In addition, they are packaged as traditional sensors (analog sensors not smart sensors) and currently used in FBW-FCS. These

sensors used in cockpit inceptors produce analog signal sent to FCC interface. Management of nearly 30 RVDTs (each with 5 wires) in the cockpit is one challenge. Another challenge is consuming lots of connector and board surface of FCC interface. Hence, it is aimed to replace the analog sensor with a smart sensor to produce a digital signal over buses [3].

2.8 Comparison of various rotation sensors

Being resistance to EMI/ EMI source, resolution/accuracy, single-turn/multi-turn, contact/non-contact are summarized in Table 2.1.

In addition, temperature range, operating range, analog/digital and operational speed of different rotation sensors are summarized in Table 2.2.

Price, size/weight, and applications and manufacturers of various rotation sensors are summarized in Table 2.3 and Table 2.4, respectively.

Table 2.1: Rotary position sensors: resistance to/source of EMI, Accuracy, Single-turn/Multi-turn, and contact/non-contact.

		EMI resistance/ Source of EMI	Resolution/ Accuracy	Single-turn (ST) Multi-turn (MT)	Contact(C) non-contact (NC)	Descriptions
Magnetic		Sensitive	12 bits [56]	-	NC	MOA: Minute of angle
Resistive		Highly resistive	1% over the full range [57]	ST/ MT	C	
Resolver/Synchro		Resistive [24]	5 to 0.5 MOA [19]	MT	NC	
MEMS	ACC	Source of EMI [58]	-	-	NC/C	
	Gyro					
Gyro			decreasing with time		NC	
Optical encoder		Not sensitive	17 bits [15]	ST/ MT	NC	
RVDT		Sensitive	1% over the full range	ST	NC	

Table 2.2: Rotary position sensors: temperature range, operating range, and Analog/digital.

		Temperature range	Operating Range	Analog (A) Digital (D)	Operation Speed High speed (>100kHz)	Descriptions
Magnetic		-40 ºC to +85 ºC [56]	360º [56]	A/D	High speed [23]	MOA: Minute of angle
Resistive		-55ºC to 300ºC [56]	Less than 360º in ST	A	Low speed	
Resolver/Synchro		-55ºC to 70ºC [57]	360º	A	Low speed	
MEMS	ACC		0º to 45º [27]	A/D	-	
	Gyro	-40ºC to 85ºC [59]				
Gyro			360º	A		
Optical encoder		-40 ºC to 70 ºC	-	D	High speed [15]	
RVDT		-55 ºC to 70 ºC [57]	-40º to +40º	A	Low speed	

Table 2.3: Rotation displacement sensor: Price, and size/weight.

	Price	Size/Weight	Descriptions
Magnetic	Low [60]	-	ST: Single turn TI: Texas Instrument
Resistive	Low [60]	-	
Resolver /Synchro	High	58mm-80mm [61]	
MEMS	Low: MEMS used in iPhone 4 cost $2.60, supplied by STMicroelectronics [62]	In µm range [29] Packages in mm [59]	
Gyro	High [26], [27]	-	
Optical sensor	Varies[60]	58mm to 116 mm for ST [56]	
RVDT	High[60] 1000$ (Internship at Bombardier)	255g	

Table 2.4: Rotation displacement sensor: applications and manufacturers.

	Applications	Manufacturers	Descriptions
Magnetic	Automation equipment and robotics [16], [22]	BEI Motion Sensors Inc.	ST: Single turn TI: Texas Instrument
Resistive	Avionic [57] Wearable Sensors [11]	BEI Honeywell	
Resolver /Synchro	High-temperature applications such as aircraft engines, petrochemical refining [13]	Honeywell Baumer	
	Machine-tool and robotics [19]		
MEMS	Apple products,	Bosch, TI, STMicroelectronics, InvenSense	
Gyro	Altitude determination (Pitch/roll/yaw angle measurement) in aircraft navigation system	-	
Optical sensor	Automotive manufacturing [10], robotics, motion capture system	BEI, Gurley, Heidenhain, Canon, Lucas Ledex TR Electronix Hewlett Packard	
RVDT	Avionic [3]	Honeywell Motion Sensors Inc. Mouser Electronics	

CHAPTER 3 DESIGN AND METHODOLOGY

3.1 Introduction

This chapter outlines the rotary encoder design and the research methodology within following sections: rotary encoder design, pattern drawing, fabrication procedure, and testing methods.

3.2 Rotary encoder design

3.2.1 Hypothesis

The main concept of the rotation sensor is shown in Figure 3.1. On the source side, a collimated beam with an elliptical cross-section is needed to illuminate a rectangular slot to make a good use of the optical power. Light is launched at a 45º angle of incidence (AOI) onto the rotary encoder after passing through the slot in which partially reflected and the rest is transmitted. On the detection sides, reflection and transmission, two convex lenses (PCX) collect the light onto the photo-detectors.

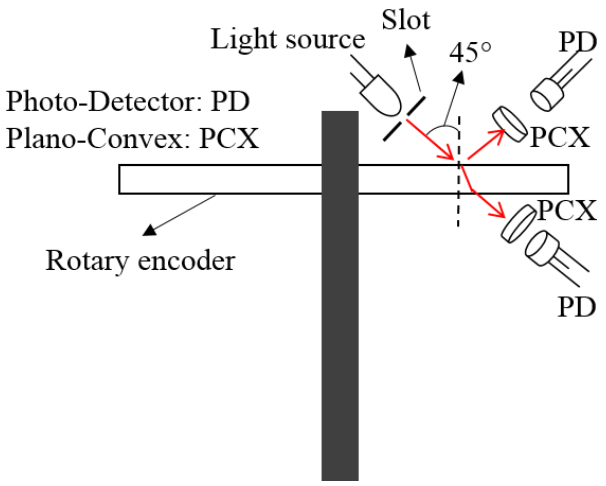

Figure 3.1 Rotation sensor concept.

Figure 3.2 shows a series of transformations needed to convert rotation angle to the electrical signals in our sensor. Firstly, the rotation angle is encoded into two areas of reflection and transmission by means of a rotary encoder. Reflection and transmission areas are encoded into reflection and transmission light powers, respectively, by applying a light source which is supposed to be uniform. Finally, light powers are converted to electrical signals through detectors.

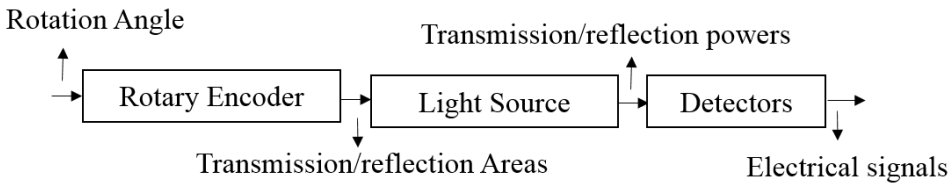

Figure 3.2 A series of transformations required to encode the rotation angle to electrical signals in our sensor.

A rotary encoder is required to encode the rotation angle into areas of reflection and transmission. Hence, an unknown curve in the polar coordination, $r(\theta)$, is supposed as shown in Figure 3.3. This curve divides the ring with the width of $d=5mm$ and inner radius of $R=8.5mm$ into two sections.

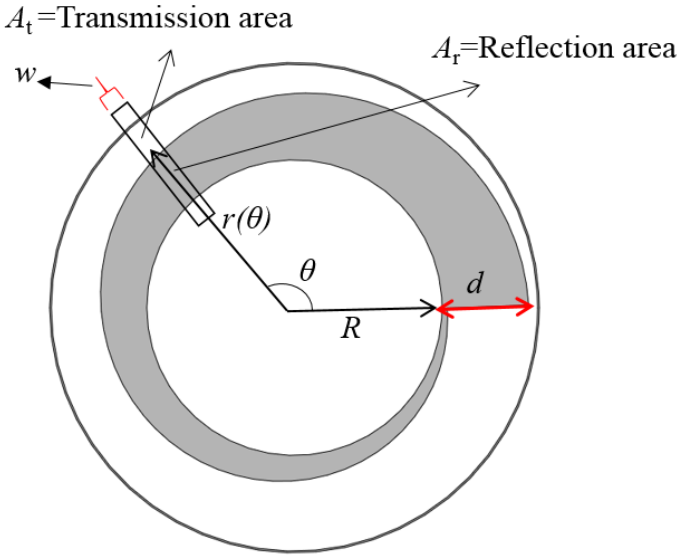

Figure 3.3 Rotary encoder with unknown curve $r(\theta)$. Gray and white show reflection and transmission areas, respectively.

Rectangle with the width w in Figure 3.3 shows the light with a rectangular cross-section on the rotary encoder. Reflection and transmission areas, A_r and A_t, respectively, as functions of the rotation angle, are calculated as:

$$A_r = w(r(\theta) - R) \qquad \text{Eq. 3.1}$$

$$A_t = w(R + d - r(\theta)) \qquad \text{Eq. 3.2}$$

Assuming a uniform distribution of the source light, $I(x,y) = I_0$, the reflected and transmitted powers are proportional to the reflected and transmitted areas, respectively, as shown in Figure 3.4.

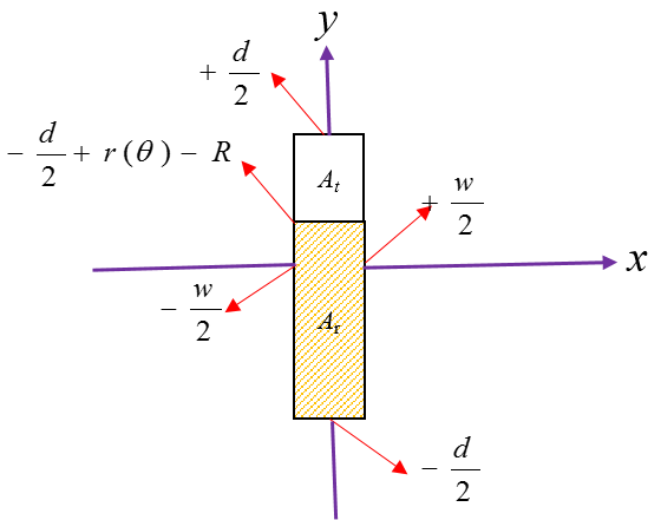

Figure 3.4 Light distribution in the reflection and transmission areas in the rotation angle θ

Reflected and transmitted light powers are calculated as per Eq. 3.3 and Eq. 3.4, respectively.

$$P_r = \iint_{A_r} I(x,y).dx.dy = \int_{-w/2}^{+w/2} \int_{-d/2}^{-d/2+r(\theta)-R} I_0.dx.dy = w.I_0.(r(\theta) - R) \qquad \text{Eq. 3.3}$$

$$P_t = \iint_{A_t} I(x,y).dx.dy = \int_{-w/2}^{+w/2} \int_{-d/2+r(\theta)-R}^{+d/2} I_0.dx.dy = w.I_0.(d + R - r(\theta)) \qquad \text{Eq. 3.4}$$

where $I(x,y)$ shows light power intensity.

Different possibilities of $r(\theta)$ are shown in Figure 3.5. The gray shows the reflection area and the white shows transmission area. To determine the unknown curve $r(\theta)$, the relation between sensor response and reflected/transmitted powers should be defined. Requirements of sensor response explained in Section 3.2.2 clarify the relation of sensor response and reflected/transmitted powers and consequently specify $r(\theta)$.

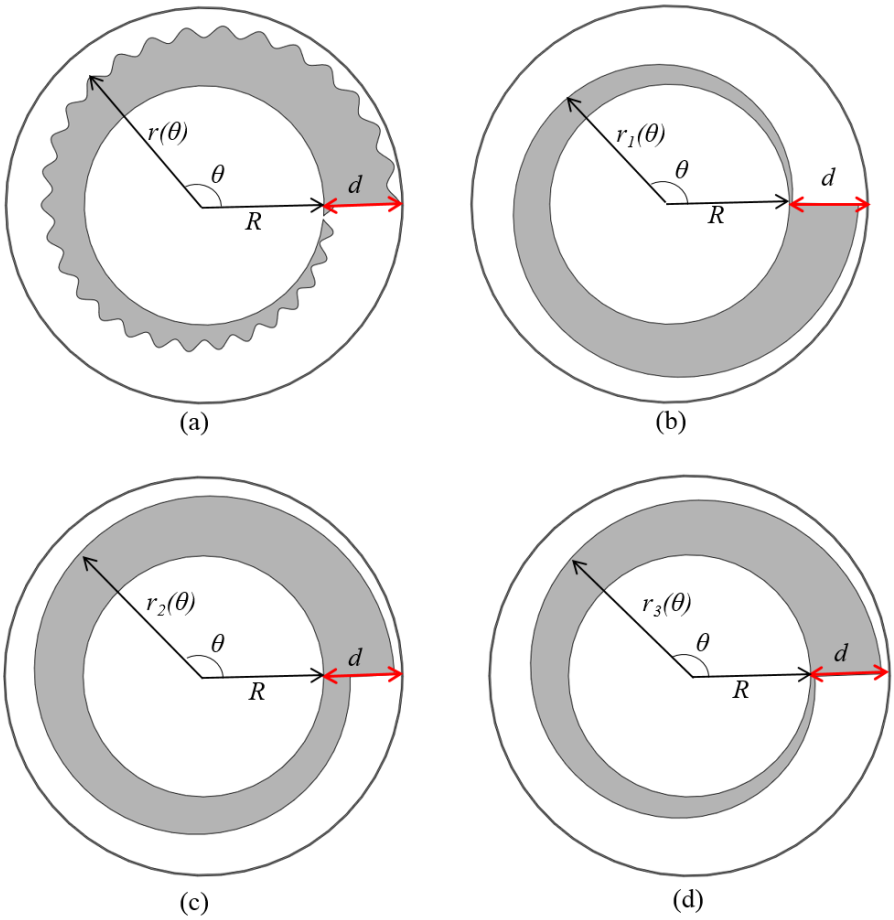

Figure 3.5 Rotary encoder with different possibilities of $r(\theta)$. Gray and white show reflection and transmission areas, respectively.

3.2.2 Rotary sensor requirements for avionic applications

Reliability: Reliability is the most important factor for an avionic application. One problem affecting the sensor reliability is degradation or fluctuation of optical source by time. To solve this problem, the sensor response, s, should be obtained from two encoded signals (here reflected and transmitted powers) as follows:

- The ratio of two signals as Eq. 3.5
- The ratio of subtraction to the summation of two signals as Eq. 3.6

$$s = \frac{P_t}{P_r} \qquad \text{Eq. 3.5}$$

$$s = \frac{P_t - P_r}{P_t + P_r} \qquad \text{Eq. 3.6}$$

Both signals are affected by the source fluctuation equally and consequently, cancel each other in the ratiometric sensor response.

Another item increasing the sensor reliability is having an encoder design to make the sensor rugged against beam profile change.

In our design, the sensor response is ratiometric and the encoder is designed in such a way that the sensor response is rugged in the case of a change in the light source profile.

Linearity: Another requirement helping us to determine $r(\theta)$ is linearity between sensor response and measurand[1], the rotation angle in the case of our sensor. Based on [63], 'A sensor is a transducer that responds to the measurand. To remain unambiguous, the response of the sensor should be:

1- Ideally a linear function of measurand
2- Strictly a single value parameter without hysteresis.

Therefore, sensor response [63] should be as Eq. 3.7:

$$s = K.x \qquad \text{Eq. 3.7}$$

Where parameters s, x, and K are the output of the sensor, measurand, and the sensor sensitivity. In the case of the rotary displacement, sensor measurand is rotation angle. Hence, Eq. 3.5 and Eq. 3.6 will be as

$$s = \frac{P_t}{P_r} = k.\theta \qquad \text{Eq. 3.8}$$

[1] Measurand: what is measured, in the case of our sensor, the measurand is the rotation angle.

$$s = \frac{P_t - P_r}{P_t + P_r} = K.\theta \qquad \text{Eq. 3.9}$$

Substituting Eq. 3.3 and Eq. 3.4 in Eq. 3.8 and Eq. 3.9, one can determine the curve $r(\theta)$.

Sensitivity: The sensitivity of rotation sensor is calculated as the differentiation of sensor response with respect to the rotation angle as Eq. 3.10:

$$Sensitivity = \frac{ds}{d\theta} = k(orK) \qquad \text{Eq. 3.10}$$

where s is sensor response, and θ is the rotation angle. Sensor sensitivity, $k(K)$, is selected based on the curve $r(\theta)$ and the sensor operating range.

Accuracy: Resolution and accuracy represent that how much exact the sensor is; however, they have a different definition. Resolution is the smallest detectable part in digital sensors. In reality, resolution of analog sensors is considered to be infinite. Accuracy is related to the acceptable error which should be 1% over the full range.

Speed frequency: Speed frequency of digital rotation sensor is calculated as:

$$speed = resolution.\frac{RPM}{60} \qquad \text{Eq. 3.11}$$

RPM stands for the revolution per minute. The sensor is called high frequency for the frequencies more than 100 kHz. All sensors for pilot input control are low-frequency sensors with the frequency of around 1 kHz.

Compatibility: The sensor should be compatible for avionic applications and specifically for pilot input control purposes. For example, being small is always considered as an advantage; however, a micrometer-sized sensor (such as MEMS) cannot be used for a centimeter sized application. Or, being high speed is usually a positive aspect while it allows the broadband noise for the low-frequency applications.

Electromagnetically, the sensor should be compatible. Being electromagnetically compatible, two aspects should be considered: the electronic circuit should not be EMI source and the whole sensor should be immune to EMI.

EMI Source: The integrated circuit of the sensor could be EMI source if a part of the electronic board acted as an antenna. A part of board acts as an antenna if its length is more than $\lambda/6$. As our sensor is a low-frequency device (1 kHz), the wavelength is around 300 km far from the range of device size (in cm) showing that it cannot be EMI source.

EMI Immunity: EMI sources against which our sensor should be immune are radio communication systems in the aircraft working in the frequency range of HF and VHF. Making the sensor immune to EMI, it is vital to use low pass filter (LPF) and decoupling capacitors in the electronic circuits.

Operating temperature: Optical sensors lose performance at temperatures greater than 70°C because of the intrinsic properties of the photodiodes and laser diodes commonly used as receivers. However, based on the specification [3], required temperature range should be from -40 ºC to +55ºC which is practical with optical sensors.

3.3 Drawing

To fabricate the rotary encoder, the Gerber file of the encoder design should be prepared. DXF file was generated using Solidworks software. Next, LinkCAD software was used to convert DXF file to Gerber file. In the procedure of drawing and exporting Gerber file, some indispensable notes should be considered as explained in the subsequent sections.

3.3.1 Resolution of drawing

Firstly, drawing the pattern with the maximum resolution is of great importance. The precision should be adjusted in Tools/Option/Document properties/Units in Solidworks. Also, the precision should be maintained through exporting DXF file in Solidworks software and converting DXF file to Gerber file in LinkCAD software by selecting the right formats. Figure 3.6 shows one of the fabricated masks having the problem of low resolution in which the patterns are like polyline curves. This problem came during converting DXF file to Gerber file in which the selected format was a polyline, while it should be arc format.

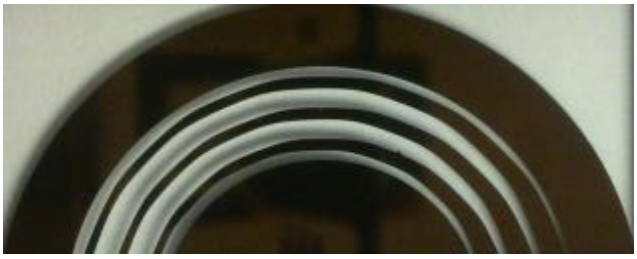

Figure 3.6 Fabricated mask with polylines instead of curves.

3.3.2 Filling reflective areas

The reflective area of the designed pattern should be filled in the drawing to represent the sections where the reflective material should be deposited. To fill the desired parts, one important trick should be considered which is explained as follows. Suppose two concentric circles as shown in Figure 3.7 (a). The area between two circles could be filled in the drawing software such as Solidworks or AutoSketch. However, when the file is converted to Gerber file, one will realize that the whole outer circle is filled. The problem coming from the fact the area between two circles is a multiply connected region. Hence, the solution is the conversion of multiply connected domain to two simply connected domains as shown in Figure 3.7 (b) and (c).

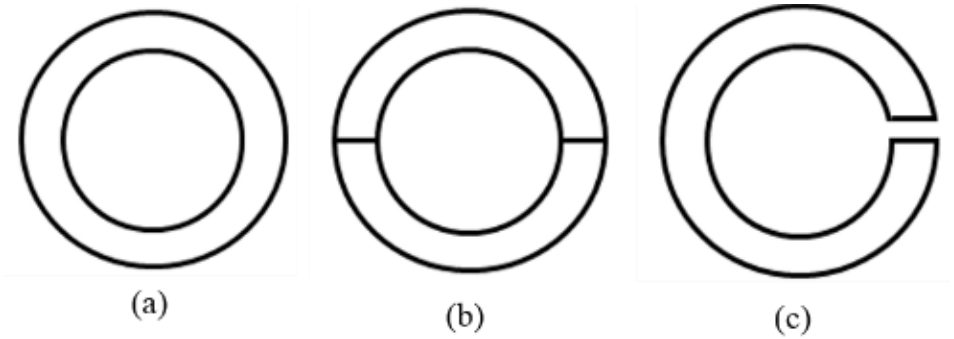

Figure 3.7 Filling tricks: (a) multiply connected domain which is impossible to fill, (b) and (c) conversion of multiply connected domain to two simply connected domains to be able to fill the area between two circles.

3.3.3 Drawing with equations in polar coordinates

There are different ways to draw a pattern with special equations such as equation in the polar coordination. In one method, Matlab software could be used to generate a matrix of points which could be imported into the drawing software such as Auto-Sketch or Solid-Works as a point cloud.

Another method is using parametric equations existing in most drawing software. For example, suppose a curve in polar coordinates such as Eq. 3.12:

$$r(\theta) = 2.\cos(\theta) - 1 \qquad \text{Eq. 3.12}$$

where θ is the angle. Hence, the parametric equations to draw the curve in polar coordinates are defined as Eq. 3.13 and Eq. 3.14:

$$x(\theta) = r(\theta).\cos(\theta) = (2.\cos(\theta) - 1).\cos(\theta) \qquad \text{Eq. 3.13}$$

$$y(\theta) = r(\theta).\sin(\theta) = (2.\cos(\theta) - 1).\sin(\theta) \qquad \text{Eq. 3.14}$$

3.3.4 Diffraction prevention

Diffraction reduction is important to be sure that the light beams in the detection sides could be captured by small lenses. Hence, to reduce the effects of diffraction, the smallest width in the patterns should have a dimension many times (ex: 10 times) larger than the operating wavelength, 650nm. Depending on the design, this limitation affects factor *K* factor (sensor sensitivity) in Eq. 3.7 and consequently sensor sensitivity a little.

3.4 Fabrication

The fabrication procedure of the optical rotary encoder and the selection of substrate depend on the type of the optical rotary encoder - reflecting, refracting, or transmitting. As our sensor uses reflection and transmission powers simultaneously, we cannot fabricate our rotary encoder in the same way as proposed in the literature [10], [12], [14], [65]. Our ratio-metric rotary encoders work simultaneously based on the reflected and transmitted powers; hence, the encoder should be fabricated in such a way that requirements of transmission and reflection area be met concurrently.

Fabrication requirements in the transmission area: power in the transmission area should be transmitted or absorbed. Power in the transmission area should not be reflected to avoid error in the reflected power. To meet the requirements in the transmission area, a highly transparent glass substrate should be coated by anti-reflection (AR) coating layers.

Fabrication requirements in the reflection area: power in the reflection area should be reflected or absorbed. Power in the reflection area should not be transmitted to avoid the error in the

transmitted power. Another remarkable point is the thickness of the reflection area which should be as small as possible in order not to block the power on the transmission side as AOI[1] is 45º. Moreover, AR coatings on the glass should remain untouched in the procedure of metal deposition. To meet the requirements in the reflection area, the reflective material, aluminum, is deposited with a sub-micron thickness.

3.4.1 Anti-reflection (AR) coating

AR coating is needed to increase the transmittance of even highly transparent glasses such as B-270 and soda-lime. With their appropriate AR coating, these glasses achieve nearly the same transmittance. Soda-lime glass with a thickness of 1mm was selected having high transmittance at red wavelengths before AR coating. The OpenFilter software was used to design the AR coating. In this software, a starting design with the number of layers and type and thickness of material in each layer is specified by the user. Then, the software uses the Levenberg–Marquardt algorithm to optimize the thickness of the layers [66]. In addition, targets describing the AR specification have to be provided. Based on the application, it may be necessary to define a target at a single wavelength or over a range of wavelengths [66]. The design targets for our application are summarized in Table 3.1:

Table 3.1 Design target for AR coating.

Item	value
Wavelength	630-650 nm
Transmittance	1 ± 0.0001
Insertion angle	45º
Polarization	Un-polarized

[1] Angle of Input

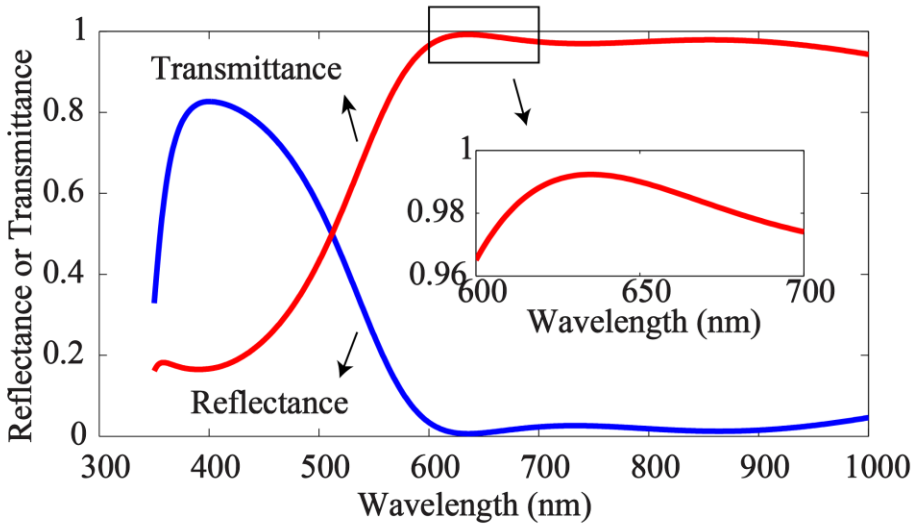

Figure 3.8 Reflectance and transmittance of glass after AR coating vs. wavelength, using OpenFilter Software

AR coating on each side of the soda-lime glass includes 4 layers of TiO2 and SiO2. The total thickness of AR layers is 312.6nm after optimization of thickness of layers to achieve the targets in Table 3.1. Figure 3.8 shows the reflectance and transmittance of AR coated glass vs. wavelength. Transmittance for red wavelength is around 99% which was proved by measurement (98.97).

The first step of fabrication, anti-reflection coating on both sides of the glass substrate, is shown in Figure 3.9.

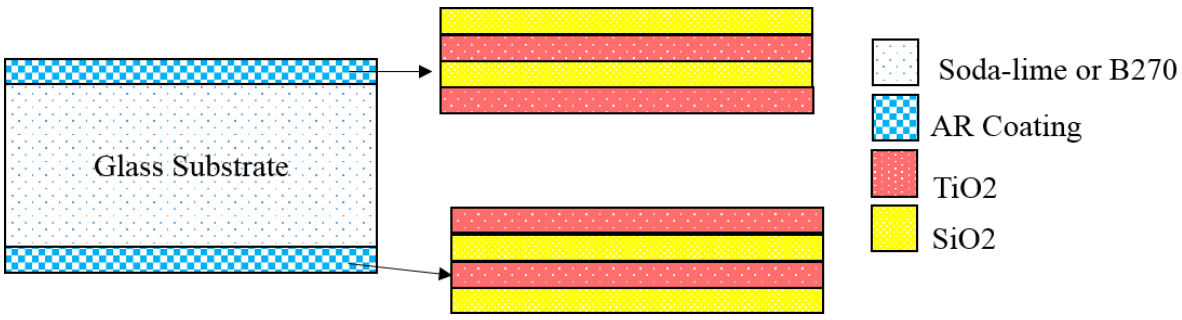

Figure 3.9 Anti-reflection coating on both sides of the glass substrates.

3.4.2 Deposition of reflective material

In the next step of fabrication, the reflective material, Aluminum, should be deposited on AR-coated glass. Step by step of aluminum deposition is explained in the following sections.

Cleaning: Before deposition of aluminum, the AR-coated glass should be cleaned and checked under the microscope to be sure that there is no dust over it.

Aluminum coating: Among the reflective materials, aluminum, and silver not only have high-reflectivity but also are not expensive. We select aluminum as it adheres to the glass.

The thickness of aluminum should be as small as possible to avoid light blockage on the transmission side. However, if it is less than a certain amount, the transmitted power would not be zero resulting in an error to the sensor response because of error in the transmitted power. For example, for 10 nm thickness, the transmitted power won't be negligible. Figure 3.10 shows reflection, absorption, and transmission of aluminum with 10 nm thickness deposited on the glass substrates, for an input angle of 45º and unpolarised light. At 633nm, transmission is 9.57% which cannot be ignored.

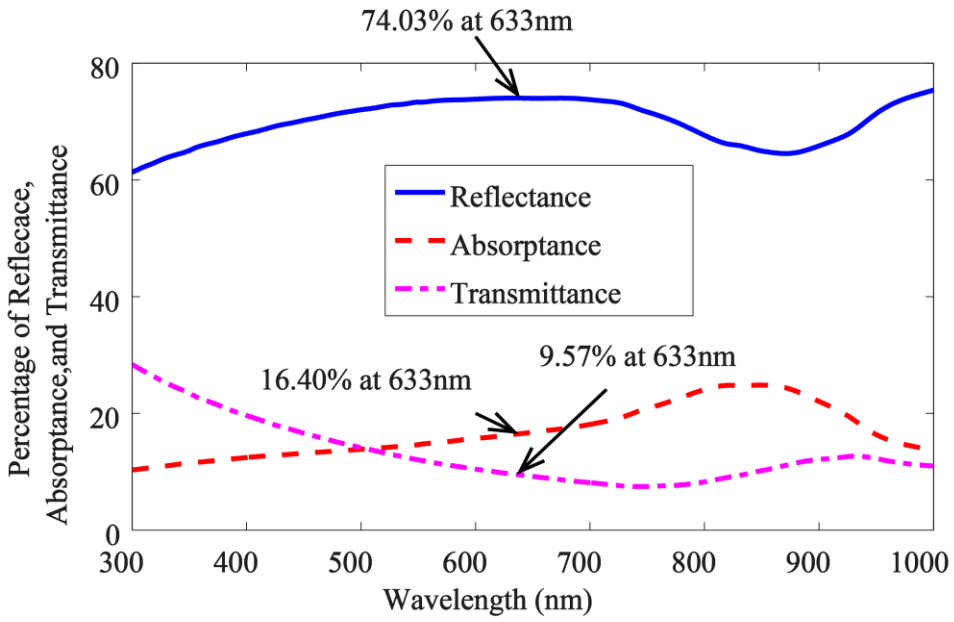

Figure 3.10 Reflection, absorption, and transmission of 10 nm aluminum on the glass substrate for the input angle of 45º and unpolarised light.

Figure 3.11 shows the percentage of transmitted power vs. thickness of aluminum, for the wavelength of 633nm, input angle of 45º, and unpolarised light. It demonstrates that the transmittance is negligible when the thickness of aluminum is equal or more than 40nm.

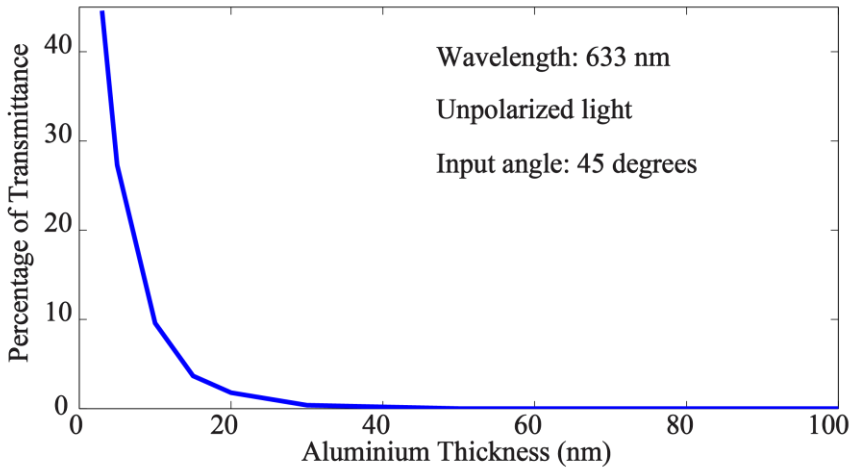

Figure 3.11 Percentage of transmitted power vs. thickness of aluminum, for 633nm, input angle of 45º and unpolarised light.

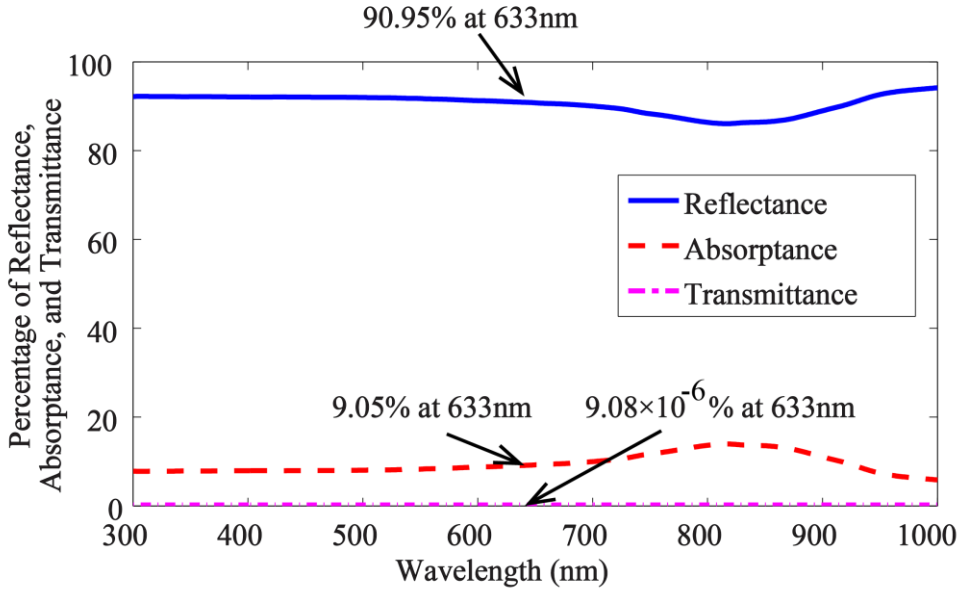

Figure 3.12 Reflection, absorption, and transmission of aluminum with the thickness of 100nm on the glass substrate for the input angle of 45º and unpolarised light.

With 100 nm aluminum, the transmitted power is negligible, around -70dB compared to the input power. Aluminum reflects 90.95% of the power in the reflection area. The rest of power is absorbed which is not considered as an error as it is 9.05% for all angles. All measurements in the reflection direction are just multiplied by a constant, 1/0.9095, to compensate for the absorbed power. (Figure 3.12)

The high-temperature sputtering deposition was used to deposit 100-nm aluminum on AR coated the glass. This deposition method is a physical vapor deposition and took 45 min. (Figure 3.13)

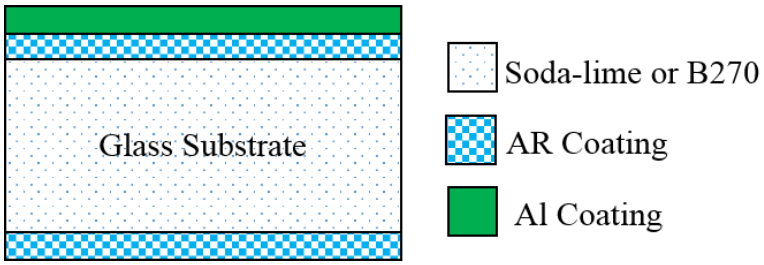

Figure 3.13 Aluminum deposition.

PR spin coating: Photo-resist, PR 1518, is deposited on the aluminum layer using spin coating machine as shown in Figure 3.14.

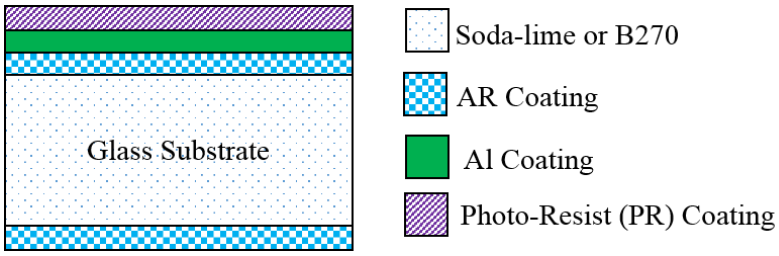

Figure 3.14 Photoresist (PR) deposition.

UV exposure: In the next step, the mask was exposed to UV light for 3 seconds as shown in Figure 3.15. The chromium glass mask is made using photo plotter machine based on the designed pattern.

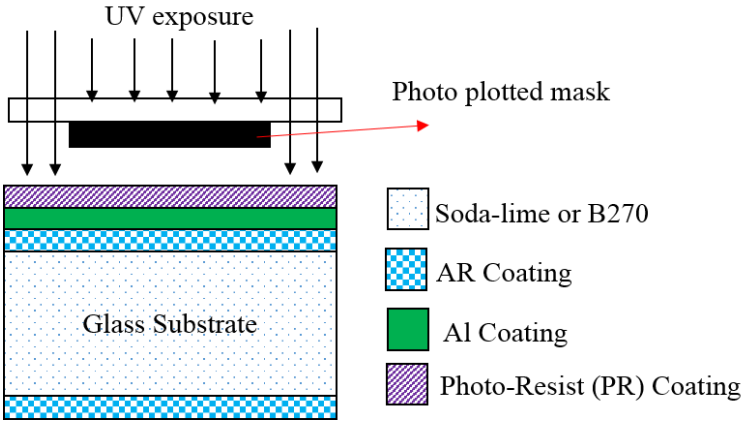

Figure 3.15 UV exposure.

Development of PR: The mask was inserted into the developer for 60 seconds to develop the photoresist as shown in Figure 3.16.

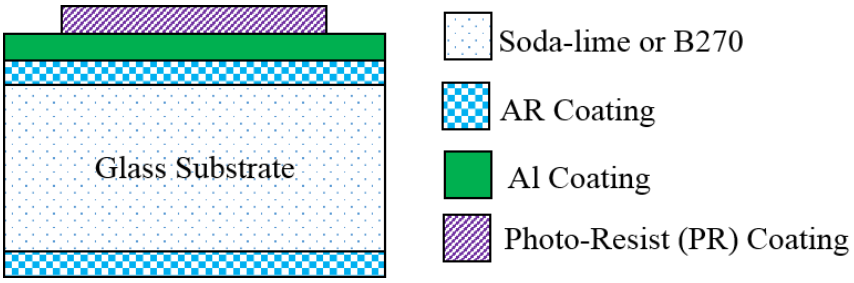

Figure 3.16 PR development.

Wet Etching: Etching of Aluminum is of great importance as it may touch the AR-coating layers. For instance, we once tried plasma etching and the experimental results showed that the AR coating layers were removed through etching. Hence, wet etching with NaOH was selected to etch aluminum. In this step, the mask was inserted to NaOH of 2 gram per liter for 5 minutes. (Figure 3.17).

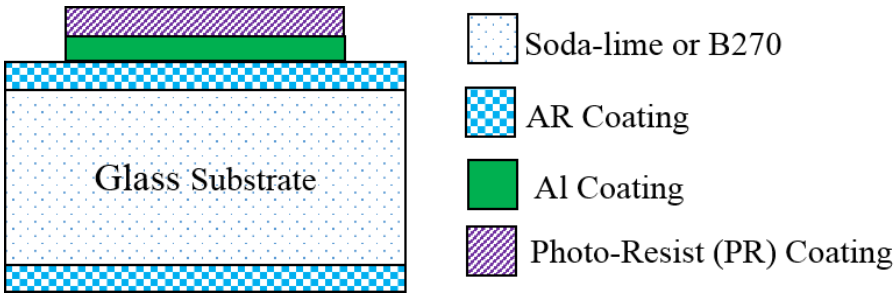

Figure 3.17 Aluminum etching.

PR removing: The mask was inserted into the acetone for 5min to wash away PR. (Figure 3.18)

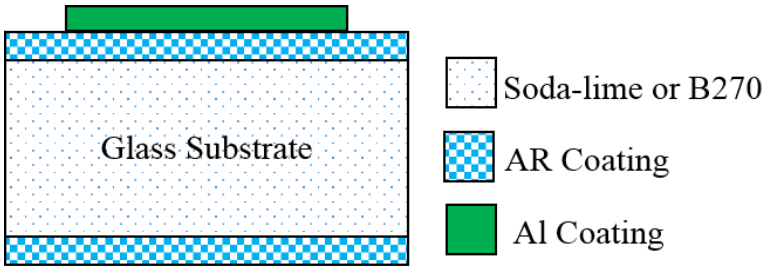

Figure 3.18 PR Removing.

In the next step, the mask was cut around using water jet machine.

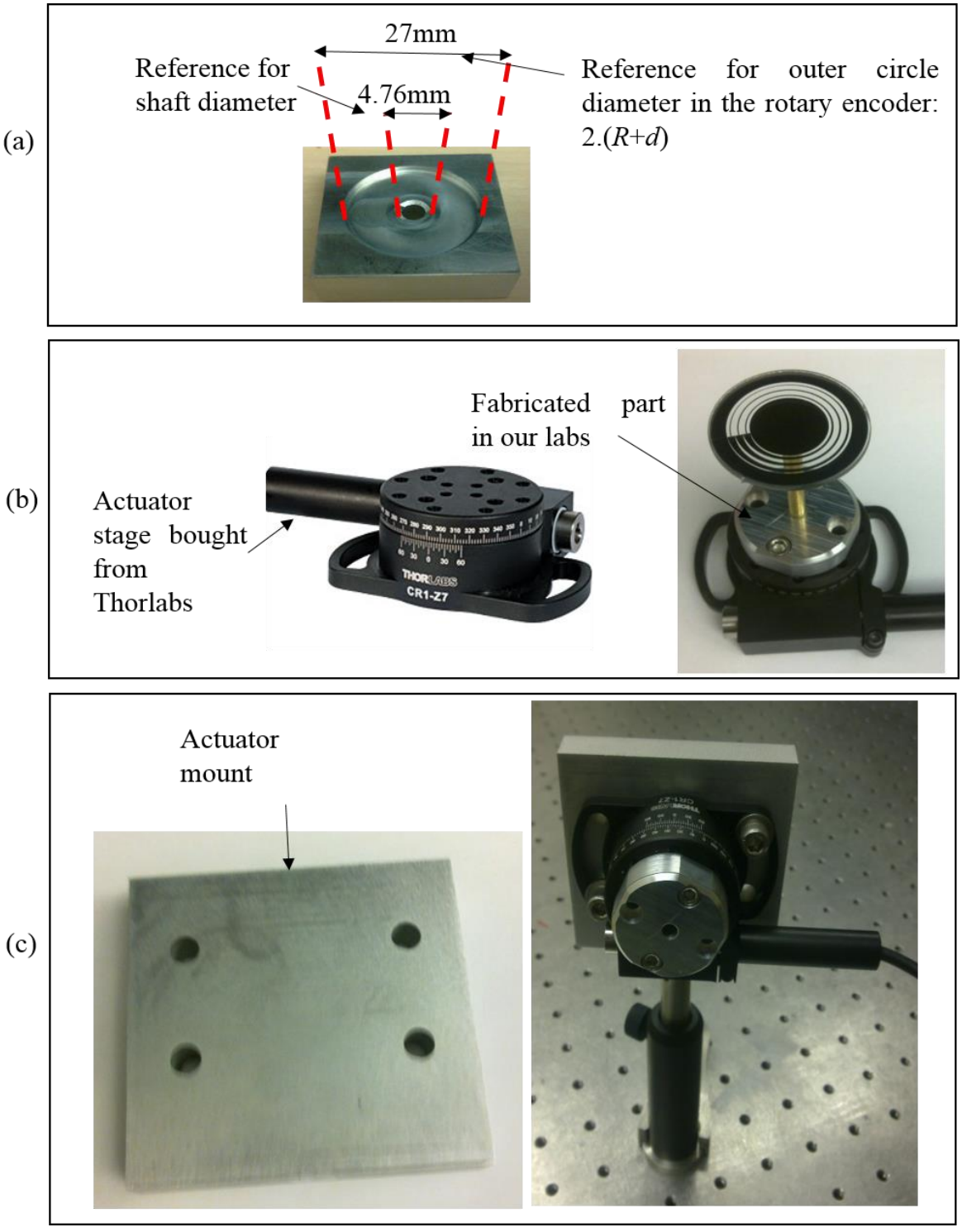

Figure 3.19 Primary mechanical setup, (a) Alignment part to find the center of rotary encoder while its installation on the shaft, (b) to install the rotary encoder on the motor stage bought from Thorlabs a mechanical piece was fabricated, and (c) installation of the actuator on the optical table.

3.5 Rotary encoder installation

Mechanical errors are one of the most important sources of error for all optical rotary encoder sensors. Therefore, installation of rotary encoder on the shaft and coupling the shaft to the motor should be done carefully which will be explained in the following sections.

3.5.1 Primary mechanical setup

It is vital to install the rotary encoder mask on the shaft very precisely in which finding the center of the mask is of great importance. An alignment device was fabricated with two concentric reference circles: one with the same diameter of the shaft (4.76 mm) and another circle with the same diameter of the outer circle in the rotary mask, 2. ($R + d$)=27mm shown in Figure 3.19 (a). The rotary encoder is placed on the alignment device in such a way that the outer circle of its pattern coincides with the reference circle of the alignment device and then shaft in the hole of alignment device is attached to the mask by means of epoxy glue.

Next, the shaft should be coupled to the motor stage bought from Thorlabs (left-hand side of Figure 3.19 (b)). Hence, one mechanical part was fabricated in our lab to connect the motor stage and the shaft as shown in the right-hand side of Figure 3.19 (b). Finally, a mechanical mount was fabricated to install the motor on the optical table as shown in Figure 3.19 (c).

The required improvements of mechanical setup in Figure 3.19 are as follows:

1. The height of the alignment part is low, hence, the shaft is wobbling during installation and consequently, the angle shaft and mask would not be 90º.
2. As the rotary encoder is installed horizontally on the optical table, a bearing is needed to prevent the shaft from bending because of gravity.
3. The area of shaft should be increased to prevent detachment of rotary encoder from shaft

In the final mechanical setup, how all above-mentioned improvements are applied is explained.

3.5.2 Final mechanical setup

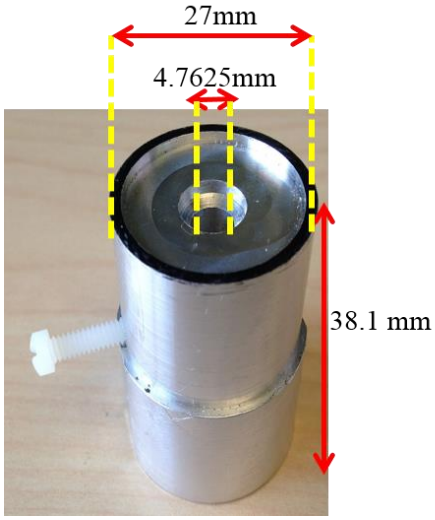

Figure 3.20 Alignment device with two reference circles to get the center of the rotary encoder.

Another alignment device was fabricated as shown in Figure 3.20. Device height is selected as 3.81mm/1.5in to prevent the shaft (5.08mm/2in) from wobbling. Another task to prevent the shaft from wobbling is to fix it by means of a plastic screw as shown in the left side of Figure 3.20. The rotary encoder is placed on the alignment device in such a way that the outer circle of its pattern coincides with the reference circle of the alignment device and then shaft in the hole of alignment device is attached to the mask by means of epoxy glue.

As the rotary encoder mask detached from the shaft while doing an experiment, the increase in the shaft area without increasing its weight was decided. Figure 3.21 shows how the shaft area is increased just in its end.

Figure 3.21 Increase the shaft area at its end.

In the next step, the shaft should be coupled to the motor using shaft coupling and bearing. Shaft coupler connects the shaft to the motor and bearing keep it straight as shown in Figure 3.22.

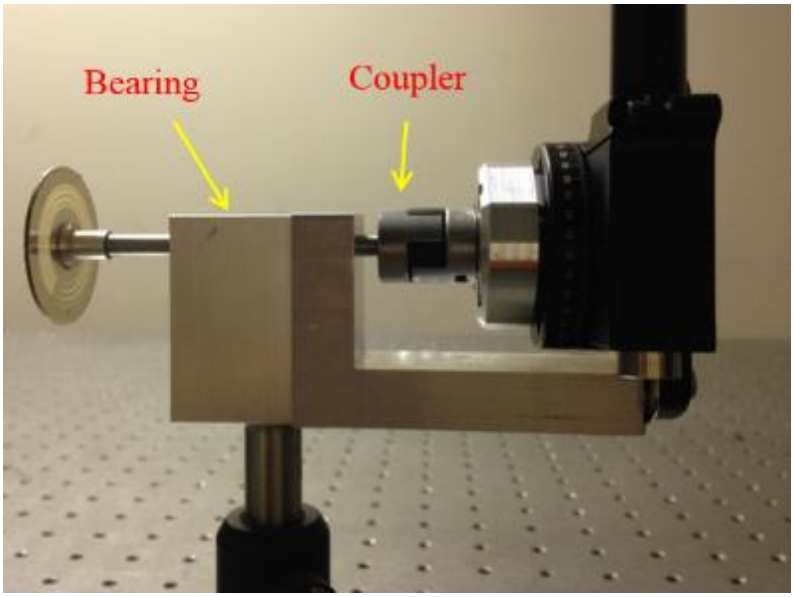

Figure 3.22 Coupling the shaft to the actuator and its installation on the optical table.

3.6 Test of the sensor

In this section, the experiment to test the mechanical setup explained. Next, two main approaches used to test the sensor are described.

3.6.1 Mechanical pre-test

To test the mechanical setup, the light beam of HeNe laser is launched into the edge of rotary encoder installed on the shaft as shown in Figure 3.22. The reflection from the rotary encoder (shown as point A in Figure 3.23) comes to a series of mirrors to make a long path of 4.5m which finally comes on the wall on point B.

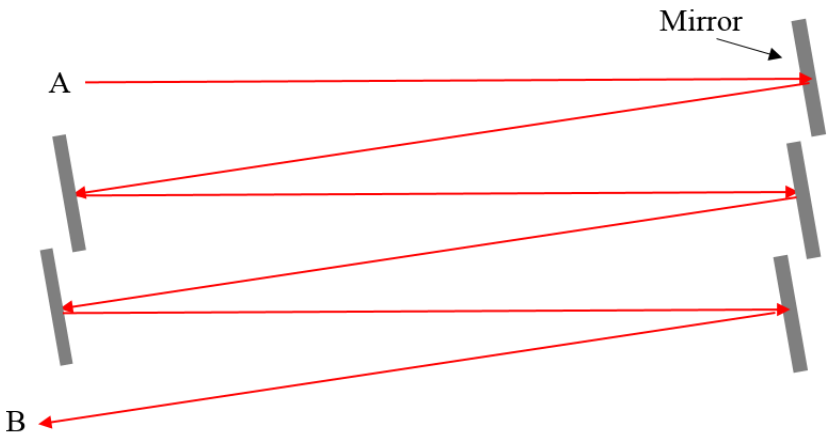

Figure 3.23 Make a long path of 4.5 m using a series of mirrors.

This experiment shows the precision of following items together resulting in the deviation of reflected ray:

- How precisely the rotary encoder installed on the shaft or what is the angle between mask and shaft.
- How precisely the shaft is installed on the motor or what is the angular displacement of the shaft
- The angle between two surfaces of the glass substrate as the reflective material is deposited on the front surface and the shaft is connected to the other side. The parallelism of glass substrates is 1 arcminute (~0.01º) in the worst case. However, AR coating and deposition of aluminum could affect the parallelism of final mask.

While rotating the motor within 48 steps in 360º, the reflected spot on the wall moves as shown in Figure 3.24.

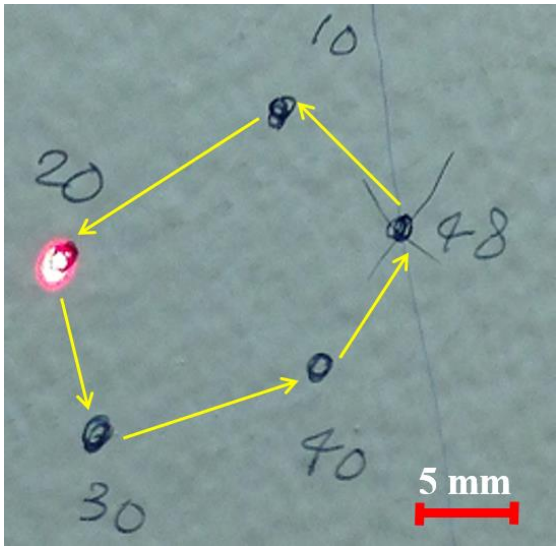

Figure 3.24 Displacement of the reflected ray on the wall while rotating the rotary mask.

When the rotary encoder mask is tilted αº, the reflected ray is tilted with 2αº as shown in Figure 3.25. The tilted angle is calculated as per Eq. 3.15.

$$\alpha = \frac{1}{2}\tan^{-1}\left(\frac{displacement}{ReflectionPath}\right) \qquad \text{Eq. 3.15}$$

where *displacement* is the deviation of reflected ray in point B of Figure 3.23 and *ReflectionPath* is 4.5m.

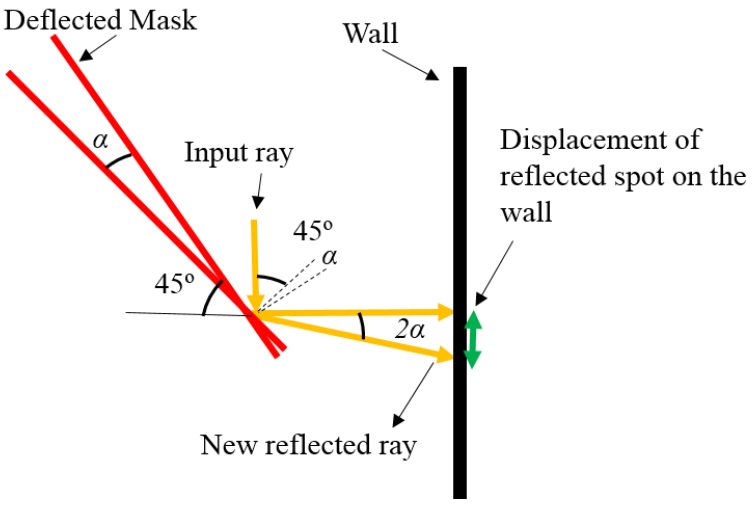

Figure 3.25 When a mirror rotates through an angle αº a beam of light reflected from it will rotate through an angle of 2αº.

In the first mechanical setup as shown in Figure 3.19, the farthest point on the wall had a large distance to the start point demonstrating the low accuracy of mechanical setup. For instance, the distance between the start point and the farthest point was 15 cm, the mechanical error was $\alpha=1^{o}$ calculated as Eq. 3.15 which is not acceptable.

Finally, all approaches explained in Section 3.5.2 were adopted to have the most accurate mechanical setup. The maximum displacement of reflected spot on the wall was 18mm. Hence, the tilted angle of the ray is $2\alpha=0.2^{o}$ showing the tilted angle of the rotary encoder is $\alpha=0.1^{o}$. This mechanical error affects different designs of rotary encoder differently.

3.6.2 First testing approach with HeNe Laser

Two setups are used to test the sensor. Primarily, a large setup including HeNe laser and Photo-detector were used to test the sensor. Next, a small setup by means of the laser diode (LD) and a photodiode (PD) was used to test the first prototype of the sensor.

To design an optical setup to test the sensor, we need to start by the design of slot because its dimension determines the beam dimension and consequently the optical items. The ring width as shown in Figure 3.3 is d=5mm. The beam length should be selected slightly larger to be sure that the ring width is covered by light. Hence, it is selected 5.5mm. Consequently, slot length should be 5.5mm/sin (45) ~ 3.9mm as shown in Figure 3.26 as there is 45^{o} between the slot and rotary encoder. The slot width is selected as 0.5mm to be large enough to prevent diffraction in the wavelength of 650nm.

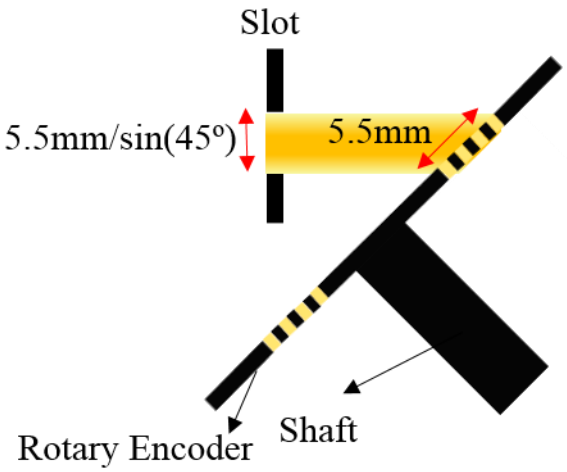

Figure 3.26 Slot length calculation.

The rectangular slot (0.5mm x 3.9mm) shown in Figure 3.27.

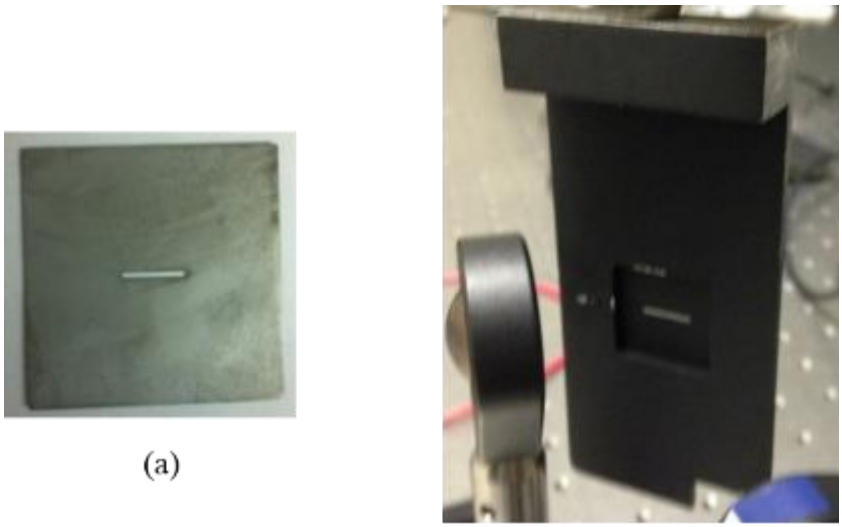

Figure 3.27 Fabricated rectangular slot (a) before and (b) after black painting and mounting.

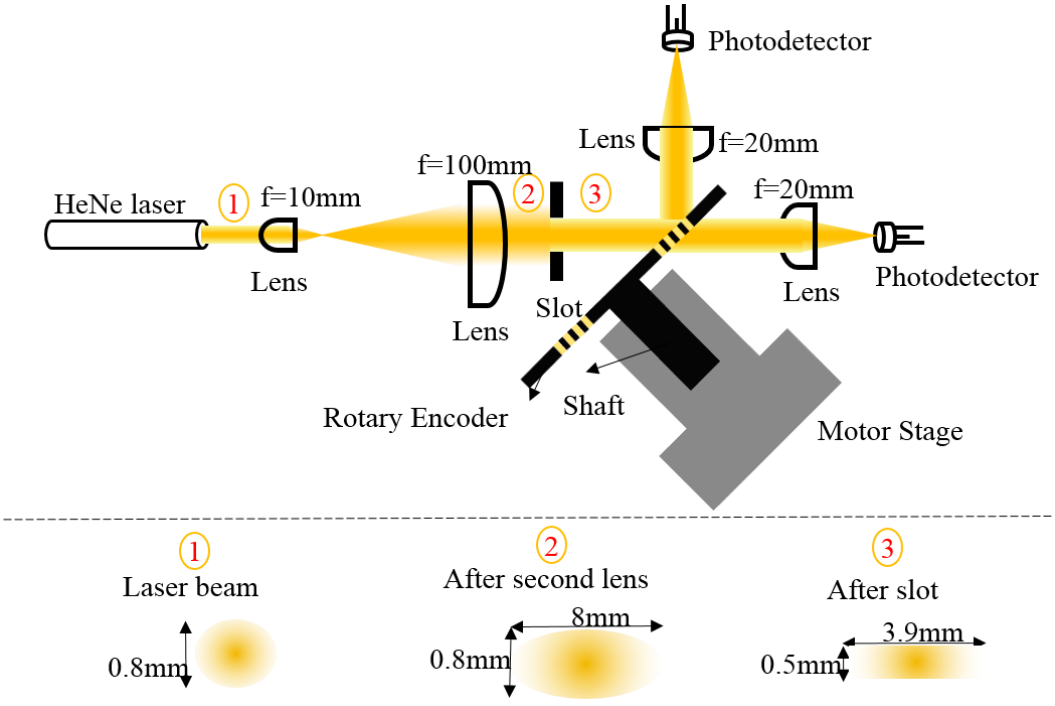

Figure 3.28 Setup with HeNe laser.

The first setup to test the rotary encoder is shown in Figure 3.28. In the source side, HeNe laser is used with the collimated beam of 0.8mm of diameter. The beam should be manipulated to make a collimated beam with an elliptical cross-section to cover the rectangular slot of 0.5mm x 3.9mm.

The simplest way to do that is keeping the vertical dimension untouched and increasing the horizontal dimension by means of cylindrical lenses. Two cylindrical lenses in which the ratio of their focal lengths is 10 are used to increase the dimension of the beam in one direction from 0.8mm to 8 mm. Hence, a collimated beam with an elliptical cross-section with the minor and major axis of 0.8mm and 8mm, respectively, is produced. The area of beam cross section is large enough to cover a rectangular slot with the dimensions of 0.5mm x 4mm as shown in Figure 3.29.

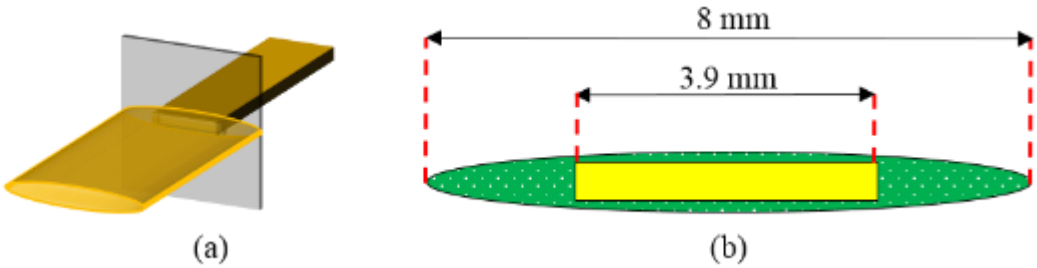

Figure 3.29 (a) 3D view and (b) 2D view of slot coverage with the beam cross section.

Light is incident on the rotary encoder at 45º AOI. A fraction of the light is transmitted and the rest is reflected. These two light powers are focused into PD by plano-convex lenses (PCX) with the focal length of 20mm. We use Plano-Convex lenses which introduce less aberration in comparison to the bi-convex lenses. To minimize aberration, a collimated light source should be incident on the curved surface of the lens as shown in Figure 3.28.

3.6.3 Second testing approach: with optoelectronic devices

The small setup with optoelectronic devices, a laser diode (LD) and photodiodes (PD), is shown in Figure 3.30. From the left, LD is driven by the current drive circuit and produce a diverging beam with an elliptical cross-section with full diverging angles of 25º and 5º, in the horizontal and vertical directions, respectively. Diverging beam with elliptical cross section gives us the opportunity to use just one lens to collimate the beam and yield a beam with an appropriate elliptical cross section. Having a beam with an elliptical cross-section with major and minor axes of *a* and *b*, the focal length of spherical lenses are calculated as:

$$f = \frac{a}{2\sin(25°/2)} \qquad \text{Eq. 3.16}$$

$$f = \frac{b}{2\sin(5°/2)} \qquad \text{Eq. 3.17}$$

Hence, a/b~5. If a is selected equal to 5mm, b will be 1mm resulting in an elliptical cross section which covers the slot properly as shown in Figure 3.31. In consequence, the focal length of the lens is calculated as 12mm according to Eq. 3.16 or Eq. 3.17.

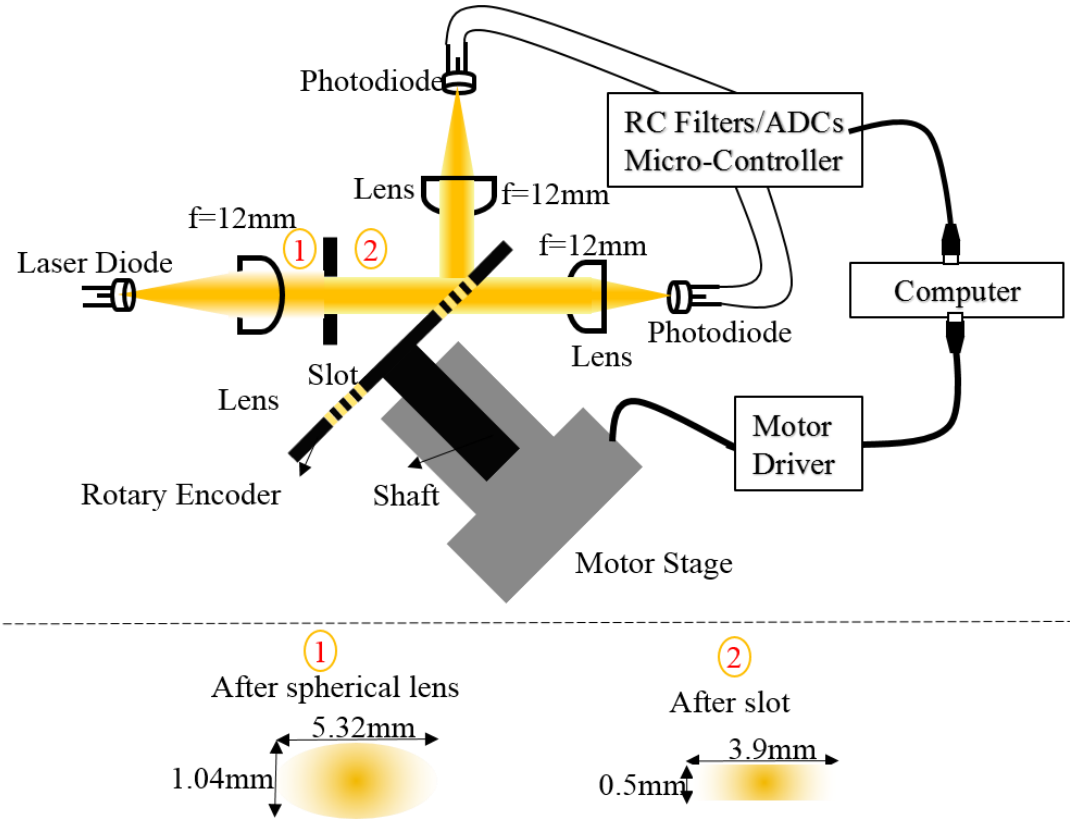

Figure 3.30 Setup with laser diode and photodiodes.

Referring to Figure 3.30, one spherical lens is used to yield collimated light with an elliptical cross section to illuminate rectangular slot. After slot (Figure 3.31), light with rectangular cross section comes to the rotary encoder where a portion of the light is transmitted and the rest is reflected. In transmission and reflection directions, light beams are captured by two lenses and focused into PDs which are connected to the RC filters. Produced voltages in the output of RC filters are digitized by ADCs and sent to the computer via USB cable. Another USB is used to connect the driver to the computer to be controlled via its related software.

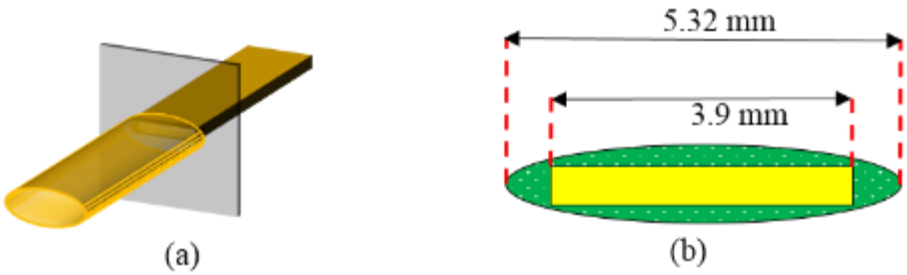

Figure 3.31 (a) 3D view and (b) 2D view of slot coverage in the setup with a laser diode (diverging angles of 25º and 5º).

3.7 Summary

In this chapter, the sensor hypothesis, requirements of the rotary sensor for avionic applications, important notes to draw the encoder pattern, fabrication procedure, mechanical consideration for installation of the mask on the motor, test setups, and mechanical pre-test were described. In the next chapter, the first rotary encoder design for operating a range of 0º to 180º will be presented in the next chapter. Chapter 4 also includes the different error analysis and experimental results.

CHAPTER 4 ANALOG OPTICAL ROTARY ENCODER (0º TO 180º)

4.1 Introduction

In this chapter, an optical, analog, self-referencing, ratio-metric, smart displacement sensor is proposed for avionic applications. The position of rotation is determined by the ratio of the transmitted and reflected light powers, which makes the sensor independent of power fluctuations. A single multi-gradient encoder design compensates for the use of a non-uniform source. An anti-reflection coated glass window with the outer diameter of 27mm is used with an encoder pattern mapped on it by aluminum deposition. The experimental results show that the ratio of the transmitted and reflected powers has an accuracy of 0.53% over the full range, matching the specifications for avionic applications. It is also experimentally showed that the sensor operates ratio-metrically and not affected by the change in the source power which makes it highly reliable for the avionic application. Further optimization of the design will make this type of sensor an excellent choice for future lightweight and greener aircraft technology.

The chapter is organized as follows. In section 4.2 and 4.3, respectively, the design methodology and rotary encoder fabrication are described. The error analysis and the experimental results are discussed in sections 4.4 and 4.5, respectively.

4.2 Device design

The main concept of the self-referencing rotation sensor is shown in Figure 4.1 (a) including the rotary encoder on a shaft, the optical source and transmission and reflection directions. On the source side, a collimated beam with an elliptical cross-section is needed to illuminate a rectangular slot to make good use of the optical power. On the detection side, for the reflection and transmission, two convex lenses collect the light onto the photo-detectors. Light is launched at a 45º angle of incidence (AOI) onto the rotary encoder after passing through the slot. The "nominally" uniform distribution of light across the slot is reflected and the rest is transmitted as shown in Figure 4.1 (b). Assuming a uniform distribution of the source light, the reflected and transmitted areas are proportional to the reflected and transmitted powers, respectively. The encoder is designed such that the ratio of reflected and transmitted areas is linearly related to the rotation angle. As the rotation angle is dependent on the ratio of the reflected and transmitted lights,

the effect of source power variation is canceled making the sensor independent of the source power fluctuation.

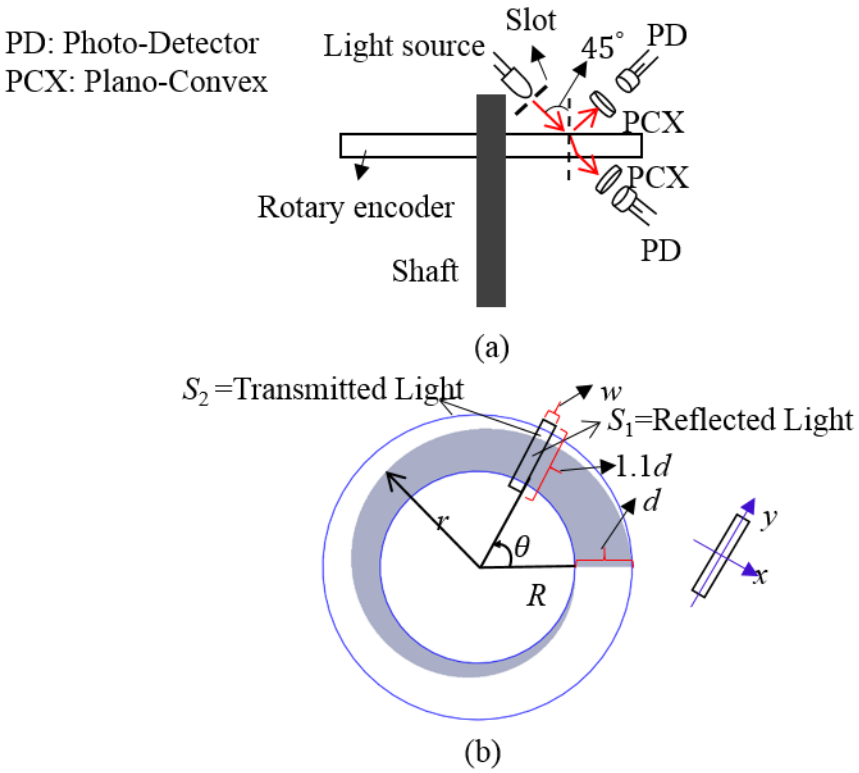

Figure 4.1 (a) Concept of the self-referencing rotation sensor showing the rotary encoder installed on a shaft. Light is incident on the rotary encoder at input angle of 45 degrees in which the "nominally" uniform distribution of light is reflected and the rest, transmitted, (b) The simplest form of a spiral rotary encoder: ring with the inner radius of *R* and width of *d* should be divided into two areas of reflection and transmission according to the position, $r(\theta)$, which is a function of θ. Grey shows the reflection area. Axis *x* and *y* show coordinates used to calculate the transmitted and reflected powers at each angle in Eq. 4.6 and Eq. 4.7. Rectangle with width *w* and length 1.1*d* shows the light with a rectangular cross section on the rotary encoder.

The simplest form of a spiral rotary encoder is displayed in Figure 4.1 (b). Selecting a spiral form, the width of the ring is divided into two segments to encode the angle of rotation into the width of these two segments. A ring with an inner radius of *R* and width of *d* should be divided into two areas of reflection and transmission according to the radial position, $r(\theta)$, which is a function of the angle of rotation, θ. The areas of *S1* and *S2* are proportional to the reflected and transmitted powers, respectively, assuming that the intensity of the beam launched into the slot is uniform.

The required beam on the rotary encoder has a width of *w* and length of a bit more than *d*, *i.e.* 1.1*d*, to be certain the width of the ring, *d*, is completely illuminated by the light from the source. Hence, the width of the slot should be the same as the width of the required beam on the rotary mask, *L*. The length of the slot, which has a 45 degrees AOI to the rotary encoder should be $1.1d \times \cos(45^{o})$.

A linear relation between the ratio of transmitted and reflected power vs. rotation angle is required as the response of the sensor should be ideally a linear function of the measurand and strictly a single-valued parameter without hysteresis [63]. Assuming a uniform light source, the ratio of two areas, which should be linear with rotation angle is given as:

$$\text{Ratio} = \frac{S_2}{S_1} = \frac{w(R+d-r)}{w(r-R)} \qquad \text{Eq. 4.1}$$

Therefore, the curve needed to divide the ring with the inner radius of *R* and width of *d* into two areas of reflection and transmission in polar coordinates, $r(\theta)$, is as Eq. 4.2:

$$r(\theta) = R + \frac{d}{1+k\theta} \qquad \text{Eq. 4.2}$$

where *k* is a constant.

Hence, the reflection, the transmission areas and along with their ratio are as Eq. 4.3, Eq. 4.4, and, Eq. 4.5 respectively.

$$S_1 = \frac{w.d}{1+k\theta} \qquad \text{Eq. 4.3}$$

$$S_2 = \frac{w.d.k\theta}{1+k\theta} \qquad \text{Eq. 4.4}$$

$$Ratio = \frac{S_2}{S_1} = k.\theta \qquad \text{Eq. 4.5}$$

Values of the constants are *R*=8.5mm, *w*=0.5mm, and *d*=5mm.

If the light power distribution is uniform, the reflected and transmitted powers can be calculated as per Eq. 4.6 and Eq. 4.7 respectively. The ratio of reflected and transmitted powers will be as per Eq. 4.8.

$$P_t = I_0 \int_{-\frac{w}{2}}^{\frac{w}{2}} dx \int_{R+\frac{d}{1+\theta}}^{R+d} dy = I_0 \frac{w.d.\theta}{1+\theta} \qquad \text{Eq. 4.6}$$

$$P_r = I_0 \int_{-\frac{w}{2}}^{\frac{w}{2}} dx \int_{R}^{R+\frac{d}{1+\theta}} dy = I_0 \frac{w.d}{1+\theta} \qquad \text{Eq. 4.7}$$

$$Ratio = \frac{P_t}{P_r} = \theta \qquad \text{Eq. 4.8}$$

where I_0 is a constant representing a uniform power density and k is selected to be one as the spiral starting at $r(0°)=R+d$ comes to $r(360°)\sim R$.

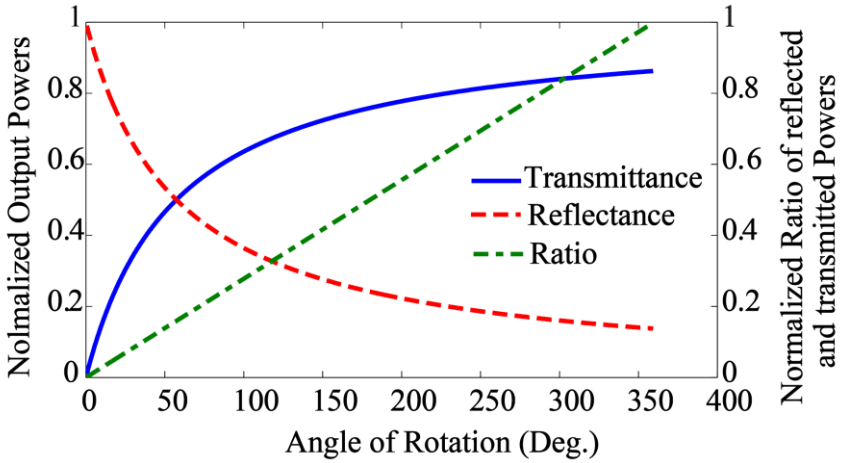

Figure 4.2 Normalized reflected and transmitted powers and their ratio, in theory, supposing uniform source light.

For our sensor, the typical functions of reflected and transmitted powers and their ratio vs. rotation angle are shown in Figure 4.2. The ratio of transmitted and reflected powers changes linearly with the rotation angle. However, the distribution of light from a real-life source on the rotary encoder is not uniform. Light power distribution is normally found to be Gaussian, diverging, and there

exists an angle between light propagation direction and rotary encoder; this source is called hereafter, as an expanded Gaussian source. Different possible light distributions are depicted in Figure 4.3 (a)-(c).

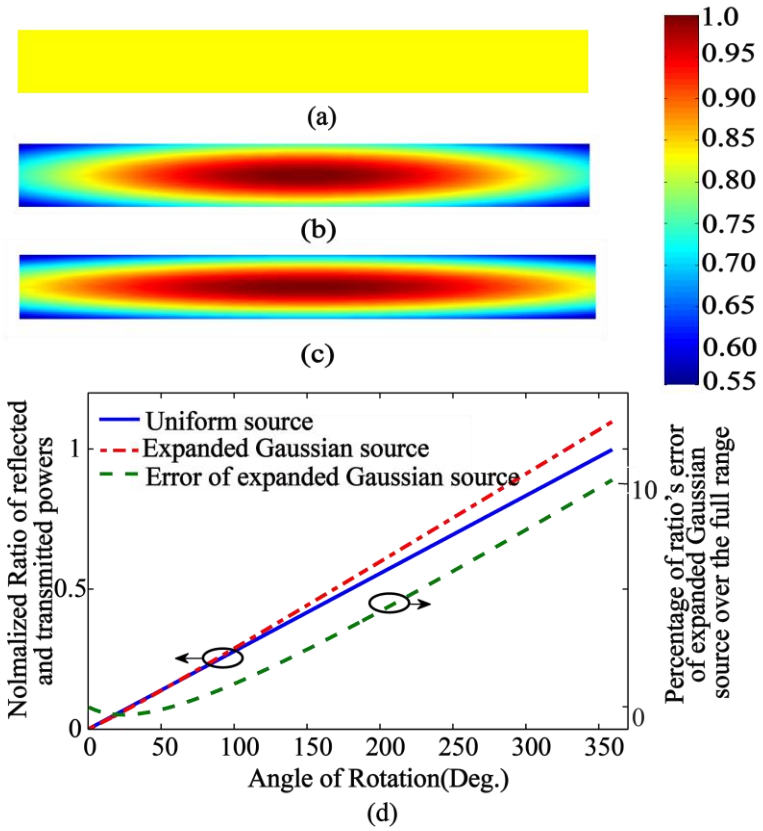

Figure 4.3 (a) Uniform, (b) Gaussian and (c) expanded Gaussian light distribution and (d) Ratio of reflected and transmitted powers for uniform and expanded Gaussian sources vs. rotation angle, and error of expanded Gaussian source (in green dashed curve).

The ratios of reflected and transmitted powers for a uniform and an expanded Gaussian light source are shown in Figure 4.3 (d). The green dashed curve shows the percentage of error of the expanded Gaussian source for the full range. RVDTs used in avionic systems have an error of 1% over the full range; therefore, clearly, the error for the expanded Gaussian source is higher than the permitted maximum error for avionic applications.

To avoid this non-linear error, a multi-ring encoder was implemented in order to approximate the source as a uniform source in sampling each ring. In this case, the ring with the width of *d* as depicted in Figure 4.1 (b) should include several patterned-rings. Based on the simulation, at least 6 patterned-rings are required to linearize the ratio of the transmitted and reflected powers as a

function of the rotation angle. To reduce the effects of fabrication errors, which cause the local width of the spiral to vary with the angle, it was decided to connect the neighboring reflection areas to each other. Therefore, the reflection areas of odd rings (light gray spirals) are flipped over to be connected to the reflection areas of even rings as per Figure 4.4.

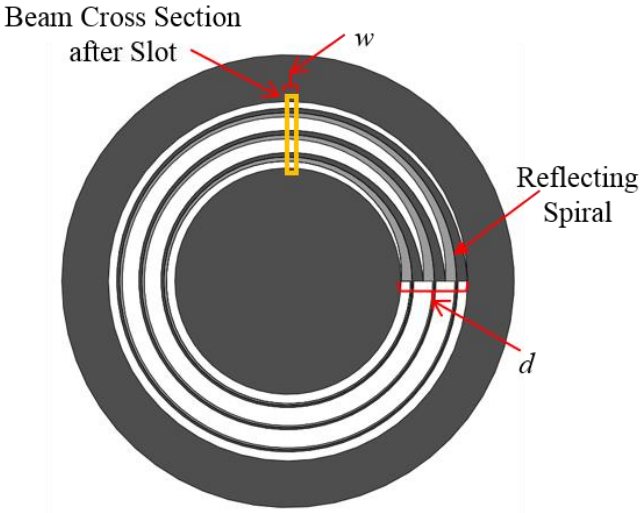

Figure 4.4 Rotary encoder called six-symmetric-patterned-rings as patterns of odd rings (light gray) spirals are symmetric to the patterns of even rings (dark gray spirals). Light and dark gray show the reflection area and white area shows the transmission area.

With six curves of $r(\theta)$, odd and even curves as per Eq. 4.9 and Eq. 4.10, respectively, the design is called six-symmetric-patterned rings, in which the patterns of odd rings (light gray spirals) are symmetric around the patterns of even rings (dark gray spirals) in Figure 4.4.

$$r_{2i-1}(\theta) = R + (2i-1)\frac{d}{6} - \frac{d/6}{1+k\theta}(i = 1,2,3). \qquad \text{Eq. 4.9}$$

$$r_{2i}(\theta) = R + (2i-1)\frac{d}{6} + \frac{d/6}{1+k\theta}(\mathrm{i} = 1,2,3). \qquad \text{Eq. 4.10}$$

where k is selected to be one (1/rad.) as the error of fabrication limits the operating range, for the greater values of k.

Figure 4.5 shows the ratio of the transmitted and reflected powers using Eq. 4.6 and Eq. 4.7 for different sources and two different patterns of the rotary encoders. Blue, green, and black curves exhibit the ratio with one patterned-ring, and uniform, Gaussian, and expanded Gaussian sources,

respectively. The red (dashed) curve illustrates the ratio of reflected and transmitted powers for an expanded Gaussian source and with the six-symmetric-patterned-rings. Noticeably, the behavior of the ratio curve for uniform source and one-patterned-ring is the same as the six-symmetric-patterned-rings and expanded Gaussian source. This figure confirms that the patterned-rings are certainly a robust design and compensates for the non-uniformity of the source illumination. Having a multi-patterned-ring design, the source is sampled in different spatial regions. In the other words, with a non-uniform source or a source that changes in time, with the multi-pattern-rings design, the source in each sampling ring remains uniform.

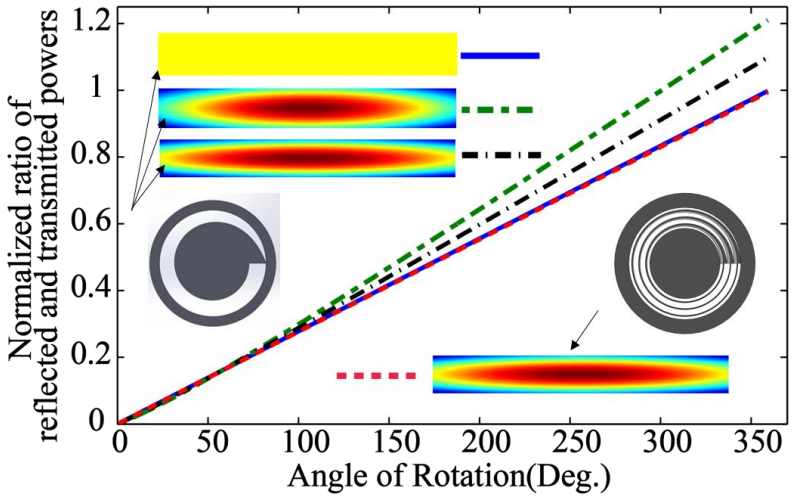

Figure 4.5 Ratio of reflected and transmitted powers for different light distributions and the two different patterns.

To verify the sensor for changes in the beam profile, we select two possible variations, a shift in the peak of expanded Gaussian source and the rise of the second lasing mode. Figure 4.6 (a)-(c) show an expanded Gaussian source, expanded Gaussian source with 25% displacement in the peak and expanded Gaussian source with the second mode with 5% increase in the power at the point of the second mode. Figure 4.6 (d) shows the ratio of the transmitted and reflected powers for these three sources which demonstrates that the ratio curves coincide and the sensor is independent of beam profile changes. With a multi-patterned-ring design, the source is sampled in multiple locations; therefore, the change in the beam profile results in moving the power from one sample to another. Hence, the normalized total reflected/transmitted powers of these samples do not alter with the variations in the source.

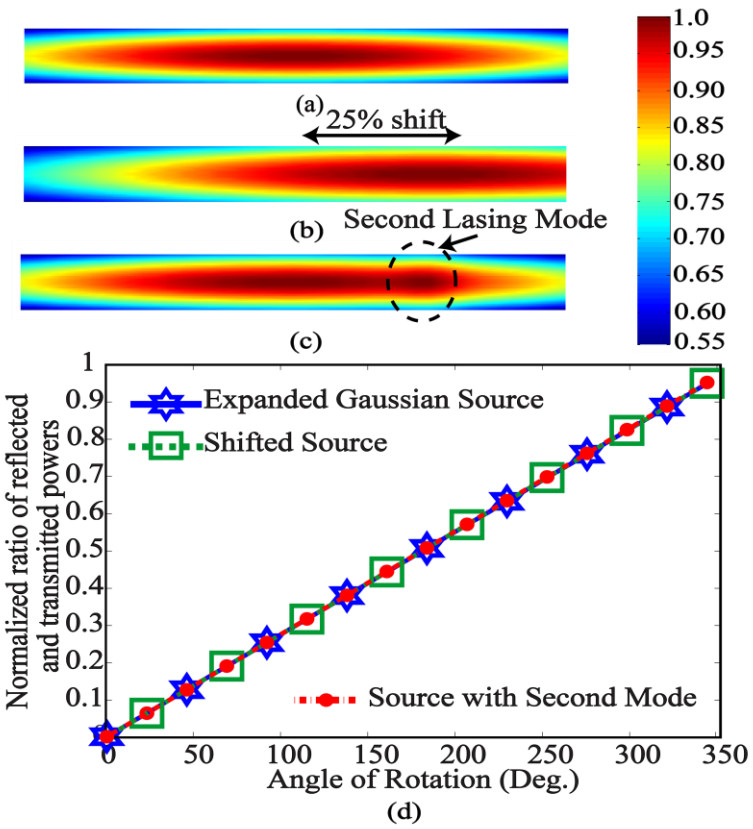

Figure 4.6 (a) Expanded Gaussian Source, (b) Shifted Expanded Gaussian Source, (c) Expanded Gaussian Source with the second mode, and (d) Ratio of transmitted and reflected powers with the multi-patterned-rings design of Figure 4.4 and for Expanded Gaussian Source, Shifted Expanded Gaussian Source, and Expanded Gaussian Source with the second mode.

A comparison of our sensor with digital optical sensors is summarized in Table 4.1. In our sensor, we applied a ratio-metric multi-patterned design to solve the problem of nonlinearity of sensor response introduced by the non-uniformity of the source and its power reduction through aging. However, to solve the same problem in digital optical sensors, preliminary calibration and self-calibration circuits are used, which make the sensor complex. In addition, an array of photo-diodes (PDs) or an image sensor are used, in the detection circuits for digital optical sensors; therefore, to decode the measurand from the measured signals, complex signal processing or image processing is required. However, only two PDs are required in the ratio-metric rotation sensor, where the rotation angle is decoded by simply dividing the transmitted power by the reflected power read by the two PDs.

Table 4.1 Comparison of our sensor and digital optical sensors

	Our sensor	Digital optical sensor [3]
Solution for compensating for the nonlinearity in the sensor response due to a non-uniform light source distribution	Ratio-metric design. Self-referencing	Preliminary calibration circuit
Solution to the nonlinearity in the sensor response resulting from power reduction of the light source through aging:	Multi-patterned optical mask	Self-calibration circuit
Number of PDs in the detection circuit	2 PDs	An array of PDs or an image sensor
Signal processing (Decoding of measurand from measured signals)	Division of transmitted power to reflected power	Image processing techniques

4.3 Fabrication of rotary encoder

The fabrication procedure is explained excessively in Section 3.4. Photograph of the fabricated rotary encoder based on the design of Figure 4.4 is shown in Figure 4.7.

Figure 4.7 Fabricated rotary encoder of the designed pattern of Figure 4.4

Please note that the mask shown in Figure 4.7 is the final mask and different masks and their related problems are classified in Table 4.2.

Table 4.2 Different rotary encoder made and their related problems. FS: Front surface and SS: Second surface.

no		Deposited material	Adhesive material	Reflection	AR coating	First/ Second surface mirror	Etching method	Problem Description
1		Cr	-	50%	-	SS (because of using Cr glass mask)	Light exposure and developer solution	Polylines instead of curves
2		Cr	-	50%	-	SS(because of using Cr glass mask)	Light exposure and developer solution	No AR Coating
2´	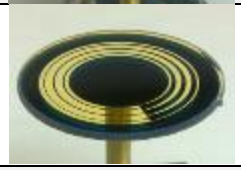	Cr	-	50%	One side	SS(because of using Cr glass mask)	Light exposure and developer solution	1. Low reflectivity 2. One side AR coating
3		Ag	Ti	65%	Both side	SS (for prevention of oxidation)	Plasma Etching	1. Low reflectivity 2. One side AR coating, after etching! 3. Checked under the microscope, polylines
4	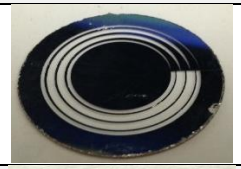	Al	-	-	-	FS	Wet etching with NaOH	It was just a sample to test the possibility of using NaOH for Al etching
4´	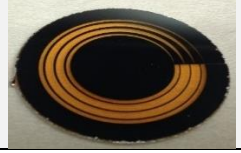	Al	-	90%	Both side	FS	Wet etching with NaOH	No problem.
All masks have the same substrate (Soda lime) and the same size (outer diameter of 27mm).								

4.4 Error analysis

Sources of errors could be categorized as design errors, fabrication errors, and experimental error which are analyzed in the following sections, respectively.

4.4.1 Design error

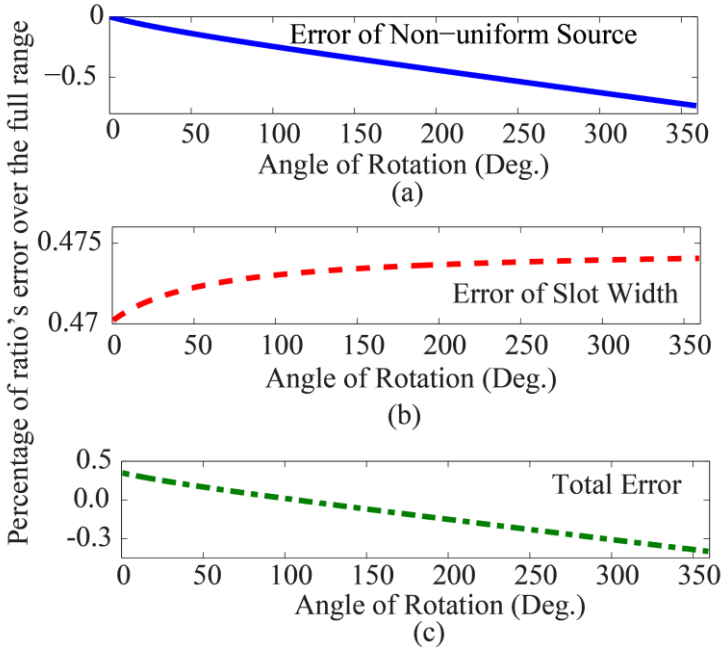

Figure 4.8 Percentage of ratio's error vs. rotation angle for (a) "non-uniform source" defined as the difference of ideal ratio and the ratio calculated in the condition of non-uniform source and six-symmetric-patterned-rings design, (b) "slot width" defined as the difference of ideal ratio and the ratio calculated in the condition that the ring's pattern varying in the slot's width, and (c) "non-uniform source and slot width" over the full range (0º-355º).

The two sources of design error are from the non-uniformity of source power distribution and the slot width. As explained in the DESIGN section, the real source has an expanded Gaussian distribution; therefore, multi-patterned-rings were applied to have nearly uniform power distribution in each ring. However, a non-uniform source with multi-patterned rings introduces a small error into the ratio of transmitted and reflected light powers. In addition, the slot width also adds error to the reflected and transmitted powers because in power calculations for each angle, as per Eq. 4.19 and Eq. 4.20, we assume the ring pattern is not varying within the slot width. Notice that the transmitted power at zero degrees should be zero but because of the slot width, there is

power in the transmitted signal. In reality, the width of the slot increases the power in the transmitted beam and reduces it in the reflected signal.

The *Error* is calculated as:

$$Error = (\theta_{EGS} - \theta_i).\frac{180}{\pi}.\frac{100}{Range} \qquad \text{Eq. 4.11}$$

where θ_{EGS} and θ_i are rotation angles assuming an expanded Gaussian beam and an ideal source. To convert radians to degrees and to calculate the full range percentage error, $180/\pi$ and $100/Range$, respectively, are multiplied into *Error*.

Figure 4.8 shows the percentage of these two errors over the full range and their cumulative effect vs. rotation angle confirming that the design error, 0.2% over the full range, is five times less than an error of RVDTs, which is 1% over the full range. The error is calculated as the root mean square of the variance of errors from the average error.

4.4.2 Fabrication error

As the curves in the design are a nonlinear function of rotation angle, the required precision varies with the angle. Therefore, the fabrication method depends on the required angle range for avionic applications.

The pitch scale range in the aviation industry is from -90º through +90º [2]; thus, the required angle range is 180°. Curves in the pattern of Figure 4.4 are a function of $d/6/(1+\theta)$, as per Eq. 4.9 and Eq. 4.10. Therefore, the curves in Figure 4.4 change as per Eq. 4.12 vs. the angle of rotation. As a result, the resolution of fabrication, $d\theta$, decreases with the angle.

$$dr = \frac{d/6}{(1+\theta)^2}.d\theta \Rightarrow d\theta = \frac{(1+\theta)^2}{d/6}.dr \qquad \text{Eq. 4.12}$$

The micro-fabrication accuracy of the fabricated rotary encoder is dr=0.5μm. Therefore, the resolution of fabrication at θ=0 and θ=π are $d\theta$ =0.034º and $d\theta$ =0.57º, respectively. Then, the root means square of fabrication resolution in the range of 0º to 180º is 0.2º. Hence, the percentage of fabrication error over the full range is 0.11% which is far below the 1% error specified for RVDTs.

For applications in which a higher range in needed, more accurate fabrication methods must be applied.

Note that the transmitted power from aluminum with a thickness of 100nm is -70dB below the input power; therefore, it does not introduce an error in the transmitted powers. Ninety-one and nine percent of power are reflected and absorbed by aluminum, respectively. Hence, the measured power in reflection direction should be multiplied by 1/0.91 to compensate for the absorbed power.

4.4.3 Experimental error

Experimental errors include installation and vibration errors. Both of these errors come from the fact that the beam with a rectangular cross section on a rotary encoder has a length a bit bigger than d to be certain that the ring's width, d, is completely illuminated by light; therefore, a fixed power is added to the reflected power which could be easily subtracted from the measured reflected power. Hence, if the rotary encoder does not stay at the same angle compared to the input beam, the power added to the reflected power varies. Consequently, any factors that change the position of the rotary encoder compared to the input beam will induce errors by adding extra power to reflected light, leading to errors in the ratio of transmitted and reflected powers.

Installation errors come from errors in the installation of rotary encoder on the shaft. Ideally, it is assumed that the angle between the rotary encoder and the shaft is 90^{o} for all rotation angles, hence, the angle between the input beam and rotary encoder remains at 45^{o} for all rotation angles. However, in the practice, there is a small error in the angle between the rotary encoder and shaft which may vary with rotation angle. Hence, when the rotary encoder turns, the angle between the light beam and the rotary encoder varies leading to a variation in the power in the reflected light. As the effect of this error is merged with the effect of the error of torsional vibration of the shaft, it will be explained in the next paragraphs.

Moreover, vibration errors are induced by the shaft's movement - upward and downward - and shaft's vibration around its axis which are called lateral and torsional vibrations, respectively. Indeed, if the shaft moves up and down, the center of the expanded Gaussian beam does not remain at the center of the ring; therefore, the reflected power changes dynamically. Hence, the reflected power has errors and accordingly, the ratio of transmitted and reflected powers has errors. For example, if the rotary encoder moves upward by 100µm, it results in a ratio error of 0.12% in the

rotation angle of 180º over the full range. Furthermore, if the shaft oscillates around its axis, the input angle of the beam into the rotary encoder will have errors as well.

Notice that this is a random error. The errors of torsional vibration of the shaft and installation were tested in one experiment in which the light was projected on the rotating mask and movement of reflected light on a screen at a distance of 4.5m was measured. It showed that the maximum error in the input angle of the beam and rotary encoder was 0.12º and this results in the maximum error of 0.81% over the full range. Furthermore, having a shaft with the length of 5.08cm (2in), the maximum deflection of the shaft will be 100µm. The transverse frequency of vibration is calculated as $f=(\sqrt{g/y})/(2\pi)$, where y is the deflection (m) of shaft and g is the acceleration due to gravity, 9.8 m/s^2. Hence, the transverse frequency of shaft will be 50Hz which is far from the vibration frequency of airplanes, 15Hz, and does not affect the measurement.

4.5 Experimental results and analysis

The setup to test the rotary encoder is shown in Figure 4.9.

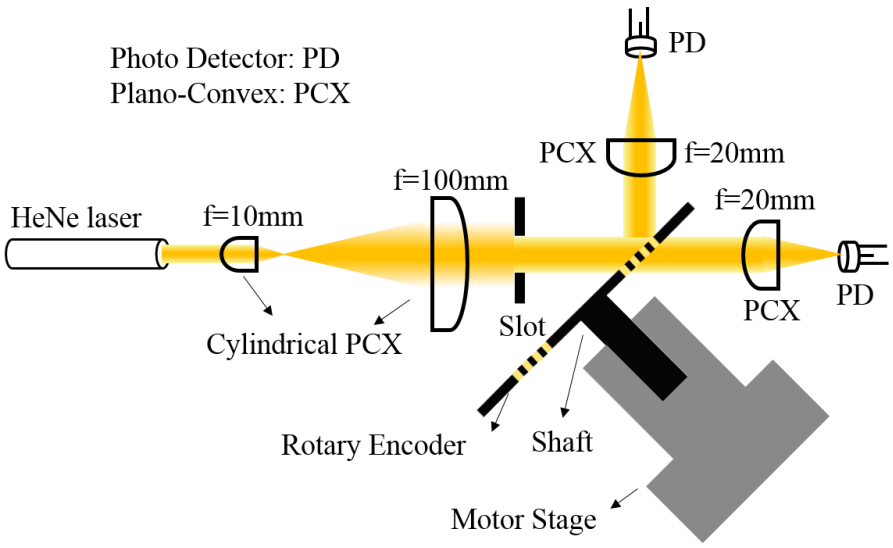

Figure 4.9 Whole setup to test the sensor.

In the source side, HeNe laser is used with the beam diameter of 0.8mm. Next, two cylindrical lenses in which their ratio of focal lengths is 10 are used to increase the dimension of the beam in one direction from 0.8mm to 8 mm. Hence, a collimated beam with an elliptical cross-section with a minor and the major axis of 0.8mm and 8mm is produced, respectively. The area of beam cross section is large enough to cover a rectangular slot with the dimensions of 0.5mm x 4mm. Light is

incident on the rotary encoder at 45 degrees AOI through the slot. A fraction of the light is transmitted and the rest is reflected, according to Eq. 4.6 and Eq. 4.7. These two light powers are focused into PD by plano-convex lenses (PCX) with the focal length of 20mm. We use Plano-Convex lenses which introduce less aberration in comparison to the bi-convex lenses. To minimize aberration, a collimated light source should be incident on the curved surface of the lens as shown in Figure 4.9.

In the prototyping of our sensor into a small housing, we use a laser diode with the diameter of 5.6mm, photodiodes with a diameter of 10mm, and plano-convex lenses with the focal length of 12mm. The related circuits of two PDs and micro-controller will be integrated into a single printed circuit board (PCB). Therefore, the final housing will be very small and will protect the sensor from environmental contamination.

Figure 4.10 (a) illustrates the theoretical and experimental normalized transmitted powers vs. rotation angle of the sensor and relative error between measurement and theory arising from Eq. 4.13. The results show that transmitted power in theory and experiment are in a good agreement with each other at large angles. Error at small angles comes from the width of slot considering that the transmitted power at zero degrees should be zero, however, because of the finite slot width there is power transmitted. As this is a constant error, it can be corrected after measurement and the final error of sensor response will be in the acceptable range. The error is calculated as the difference between powers in theory and measurement divided by power, in theory, is defined as per Eq. 4.13. P_T and P_M show powers in theory and measurements, respectively.

$$Error = \frac{P_M - P_T}{P_T} \qquad \text{Eq. 4.13}$$

Figure 4.10 (b) depicts the theoretical and experimental normalized reflected powers vs. rotation angle of the sensor and relative error between measurement and theory arising from Eq. 4.13. The results show that reflected power in theory and experiment are in good agreement with each other. As explained above, slot width increases power in the transmitted direction; indeed, this is the power subtracted from the reflected light. Since the reflected power at small angles is large, the power deducted from it brings smaller error in comparison to the error arising in the transmitted power. As a result, the error at the small angles is negligible because the ratio is calculated as

transmitted power divided by reflected power and dividing a low power with an error by a high power does not result in a big error in the ratio.

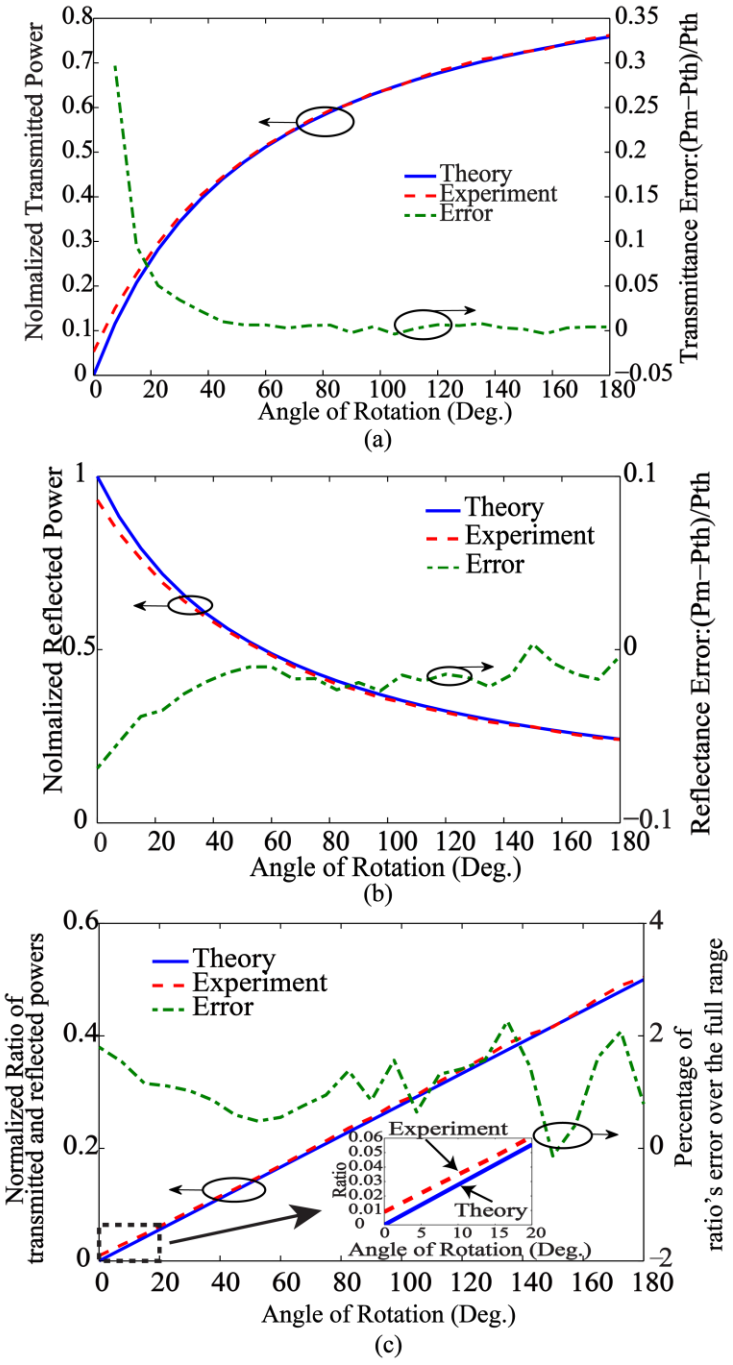

Figure 4.10 (a) Transmitted power vs. rotation angle in theory and measurement, and relative error between them. (b) Reflected power vs. rotation angle in theory and experiment, and the relative error between them. (c) The ratio of transmitted and reflected powers vs. rotation angle in theory and experiment, and percentage of error in the full range (0º-180º).

Figure 4.10 (c) shows the theoretical and measured ratio of transmitted and reflected powers and the percentage of absolute error vs. rotation angle over the full range. It shows the ratio of transmitted and reflected powers is in close agreement with the simulation. Percentage error of ratio over the full range is 1.24% showing the offset of 1.12 which is corrected in the next subsection called as Error Correction. The error of 1.24% is calculated as the root mean square of errors.

Error Correction:

Comparing the zoomed portion of ratio curves in the bottom of Figure 4.10 (c), the experimental ratio curve has an offset and inclination error compared to the ratio curve in theory. Therefore, error-correction is done to correct the inclination and offset of ratio curve to compensate for the error. The source of this error is the slot width which adds the power to the transmitted power and cuts power from the reflected power variably with the angle. As the slot width does not change with time, these corrective numbers can be used permanently to correct the inclination and offset error of ratio curve.

To do the error correction, we add two constants to the transmitted and reflected powers to correct the offset and multiply the ratio by another constant to correct the inclination of ratio curve.

Error correction is done as Eq. 4.16: two constants, called B and C, are added to the normalized reflected and transmitted powers to correct the offset, and another constant, called A, is multiplied by their ratio to correct the inclination of ratio curve.

$$Corrected\text{-}Ratio = A\frac{P_t + B}{P_r + C} \qquad \text{Eq. 4.14}$$

where P_t and P_r show normalized transmitted and reflected powers, respectively. To find three constant numbers, A, B, and C, the standard deviation of ratio error around zero is minimized; therefore, they are calculated as A = 1.066, B = -0.040, and C = 0.006. The ratio of transmitted and reflected powers after error correction and its error over the full range, are shown in Figure 4.11. Ratio errors over the full range are 0.53% which shows the smaller error in comparison to the error of current RVDT used in avionic applications. Hence, the angular accuracy of the sensor is 0.53% over the full range which is the error of sensor response from the ratio of transmitted to reflected powers.

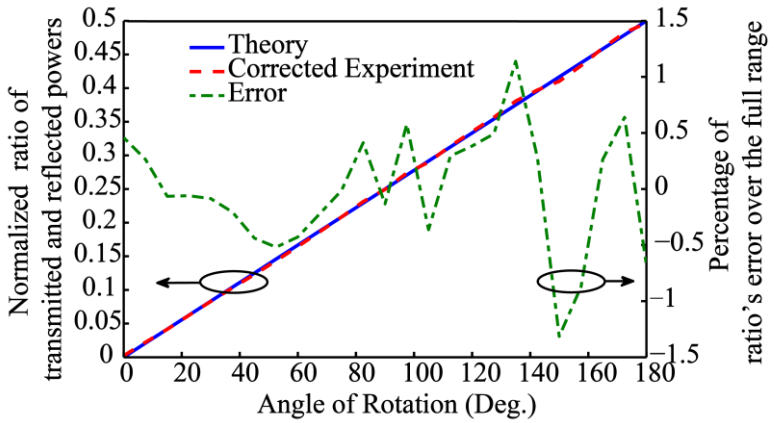

Figure 4.11. The ratio of transmitted and reflected powers vs. rotation angle in theory and experiment, and percentage of error in the full range (0º-180º) after error correction. Vibration error is one of the sources of error at 150 degrees which is a random error and uncorrectable as long as a faulty fixed power is added to the reflected power because of a slot with a length bigger than the width of the ring. Note that the sensor response is obtained from the division of transmitted power to the reflected power in which the error of reflected power, in the denominator, is more effective than the transmitted power, in the numerator, especially when the reflected power is low at high angles.

More accurate sensing is possible by reducing errors of design and experiment. Errors from design, induced from the slot width and non-uniformity of the source, can be decreased by selecting a slot with a smaller width and having more patterned-rings in the design. For example, if eight-patterned-rings and a slot with the width of $200\mu m$ are used, the error of design decreases to 0.1% over the full range. Moreover, experimental errors, from installation errors and vibration of the shaft in motor, can be reduced by covering the area outside the ring by a black material, which can absorb the light added to the reflected power because of having a beam with a length bigger than the ring's width. However the thickness of this material would be a challenge as it blocks incident and reflected lights. For example, if its thickness is 2µm, error would be 0.06% over the full range. Eventually, by applying these suggestions in design and experiment, the overall error could be reduced to 0.16%, 0.1% from design and 0.06% from experiment, over the full range. We suppose that the fabrication error is negligible if fabrication technology with the precision in nanometer range is used. A prototype rotary senor in its own housing will be presented in Chapter 6. Based on references [4], [5], the definition of smart sensor is a combination of a sensor, an analog circuit,

analog to digital convertor (ADC), and a bus interface in a single housing; while a traditional sensor only provides raw signal. The prototype of our sensor includes all parts determined in the definition of smart sensor

Sensor stability by source fluctuation:

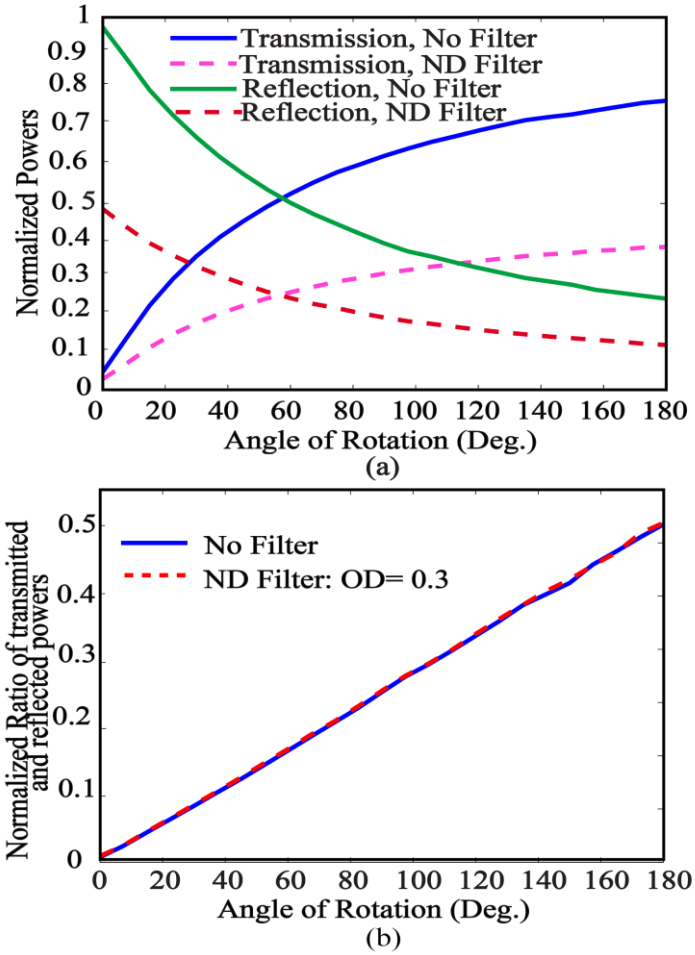

Figure 4.12 (a) Measured normalized transmitted and reflected powers without and with an absorptive Neutral Density Filter (b) ratio of transmitted and reflected powers without and with Neutral Density Filter. Optical density, OD, of the filter is 0.3 which lets 50% of power to be transmitted.

To test the stability of sensor by source fluctuations, we test the sensor response by adding an absorptive neutral density filter with Optical Density (OD) of 0.3 which transmits 50% of light. Figure 4.12 (a) shows normalized transmitted and reflected powers, with and without an absorptive neutral density (ND) filter. The measured transmitted and reflected light powers with the filter

inserted into the setup decreases to half of power without the filter. The measured ratio of transmitted and reflected light powers with and without the ND filter remains the same, as shown in Figure 4.12 (b).

Note that we use the same numbers in the Error Correction section - *A*, *B*, and *C* - to correct the error of ratio curves in Figure 4.12 (b) in which the input powers are not the same.

4.6 Summary

In this Chapter, an analog self-referencing rotary displacement sensor for avionic application was designed, fabricated and tested. To achieve high reliable device, a ratio-metric design was used in which the ratio of transmitted and reflected light powers specifies the rotation angle independent of the intensity fluctuation of the source. Consequently, a variation of the source power affects both powers equally and they cancel each other in the ratio-metric measurement. Another distinguishing aspect of our design is the multi-section pattern of the encoder and simulation results showed that this design makes the sensor robust and independent of a non-uniform source. A rotation displacement sensor was fabricated on a small AR coated glass window with the outer diameter of 27mm. Aluminum with the thickness of ~100nm was deposited on the glass and then etched according to a six-patterned-rings design. The experimental results showed the error of 1.24% over the full range. Inclination and offset error correction was performed to reduce the error of ratio of transmitted and reflected powers and achieve the accuracy of 0.53% over the full range of 0º to 180º. It was also experimentally showed that the sensor response is stable with the change in the source power which makes it highly reliable for the avionic application. As explained at the end of subsection Error Correction, with further optimization of the design and experiment, the error could be reduced to 0.16% over the full range. The related work was published in [17], [67].

In the next chapter, the second rotary encoder design for operating a range of 0º to 365.5º will be presented. Chapter 5 also includes the different error analysis and experimental results.

4.7 Future works related to this design

4.7.1 Lower range with higher sensitivity

The design verified in this chapter works for the operating range of 0° to 180°. For lower operating ranges, the sensitivity and accuracy could be increased as there is a trade-off between operating range and sensor sensitivity.

Sensor sensitivity for operating range of 180° and a constant factor of K=1 will be as follows:

$$Sensitivity = \frac{ds}{d\theta} = k \times \frac{\pi}{180} = 17.5 mW / W / \deg \qquad \text{Eq. 4.15}$$

In lower operating range applications, the sensor sensitivity could be increased by increasing constant factor k. The designs for the operating ranges of 60° and 120° are shown in Figure 4.13 (a) and (b), respectively. In the former and the latter, k is selected as 3 and 2, respectively, resulting in the sensitivity of 52.5 $mWW^{-1}deg^{-1}$ and of 35 $mWW^{-1}deg^{-1}$.

Figure 4.13 (a) 60-degree pattern design with k=3 and (b) 120-degrees pattern design with k=2.

4.7.2 Optical linear displacement encoder

The same idea of the design procedure proposed in this chapter for the optical rotary displacement encoder could be used for an optical linear displacement encoder as shown in Figure 4.14. A strip with the width of d and length of R should be patterned to encode the displacement into the two areas of reflection and transmission. Supposing a uniform light source, the reflection and

transmission areas are proportional to the reflected and transmitted powers, respectively. Red rectangular with the width of *w* shows a beam cross section on the encoder at point *x*. Unknown curve, *y*(*x*), should be determined based on the sensor requirements explained in Section 3.2.2.

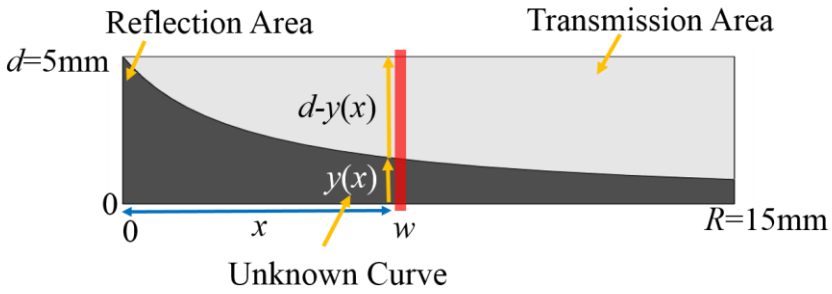

Figure 4.14 Linear displacement encoder.

Suppose that the sensor response should be extracted from the ratio of transmitted and reflected light powers, $P_t(x)$ and $P_r(x)$, respectively:

$$s(x) = \frac{P_t(x)}{P_r(x)} = k_1.x \qquad \text{Eq. 4.16}$$

where k_1 is a constant and x is the linear displacement. Reflected and transmitted powers are calculated as follows supposing light distribution with the intensity of I_0:

$$P_r(x) = w.I_0.\mathrm{y(x)} \qquad \text{Eq. 4.17}$$

$$P_t(x) = w.I_0.(d - y(x)) \qquad \text{Eq. 4.18}$$

Substituting Eq. 4.17 and Eq. 4.18 in Eq. 4.16, we will have

$$s(x) = \frac{P_t(x)}{P_r(x)} = \frac{w.I_0.(d - y(x))}{w.I_0.\mathrm{y}(x)} = k_1.x \qquad \text{Eq. 4.19}$$

Therefore, the curve needed to divide the rectangular with the length of *R* and width of *d* into two areas of reflection and transmission in polar coordinates, *y*(*x*), is as Eq. 4.20:

$$y(x) = \frac{d}{1 + k_1.x} \qquad \text{Eq. 4.20}$$

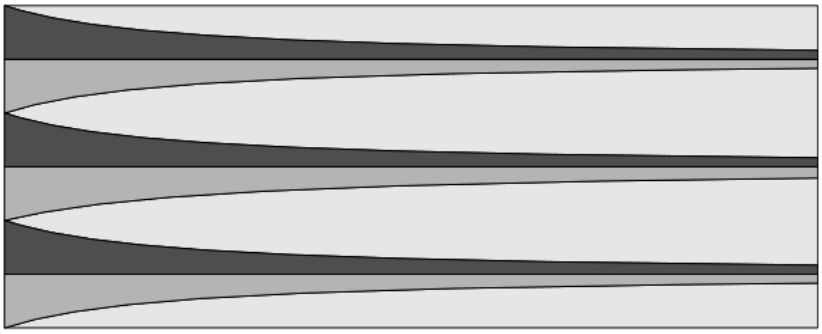

Figure 4.15 multi-patterned-encoder for linear displacement sensor, *K*=1/3 for the operating range of 15 mm.

To compensate for the non-uniform source, a multi-patterned-encoder with the following equations should be designed, as shown in Figure 4.15.

$$y_{2i-1}(x) = (2i-1)\frac{d}{6} - \frac{d/6}{1+k_1.x}(i=1,2,3). \qquad \text{Eq. 4.21}$$

$$y_{2i}(x) = (2i-1)\frac{d}{6} + \frac{d/6}{1+k_1.x}(\mathrm{i}=1,2,3). \qquad \text{Eq. 4.22}$$

K is determined based on the operating range. For a maximum operating range of *R*=15mm, *K* is selected as 1/3 to deliver the smallest width of 227µm (Eq. 4.23) which is more than 6.5µm to avoid diffraction.

$$w_i(x) = y_{2i} - y_{2i-1} = \frac{d/3}{1+k_1.x}(i=1,2,3). \qquad \text{Eq. 4.23}$$

In this encoder sensor, again there is a trade-off between sensor sensitivity (proportional to *K*) and the operating range (Proportional to 1/*K*). Sensitivity is calculated as:

$$Sensitivity = \frac{ds}{dx} = k_1 = 333mW/W/\mathrm{mm} \qquad \text{Eq. 4.24}$$

CHAPTER 5 ANALOG OPTICAL ROTARY ENCODER (0º TO 356.5º)

5.1 Introduction

In this Chapter, we present a self-referenced broad range optical rotary sensor (ORS) for avionics applications. To achieve the high reliability required for aerospace use, the rotary encoder operates ratio-metrically to make it insensitive to source light power variation. This sensor has a higher operating range than rotary variable differential transformers (RVDTs) currently used in fly-by-wire aircraft. The ORS encoder is fabricated on an anti-reflection coated glass substrate with a reflective aluminum coating. Experimental results show that the sensor accuracy is 0.8% over the full rotation range from 0° to 356.5°. The proposed ORS has better accuracy and an operating range of at least twice that of RVDTs, which have an accuracy of 1% over a full range of only 80°. We also test the insensitivity of the sensor to source fluctuations which confirms that the sensor is self-referencing.

This chapter is organized as follows. In Section 5.2, the theory, the design procedure, and the design error analysis are proposed. Next, the experimental results and the analysis are presented in Section 5.3. In the first and second experiments, sensor response - accordingly sensor sensitivity and accuracy - and sensor operating range are examined. In the third experiment, independency of the sensor from source fluctuation or self-reference property is verified. Next, sources of error are analyzed. At the end of Section 5.3, we compare our rotary sensors presented in this Chapter and in Chapter 4 with each other and with RVDTs and optical sensors. Finally, one can find conclusions and the future works related to this design in Sections 5.4 and 5.5, respectively.

5.2 Rotary encoder

In this section, the principle of operation, the theory of the optical sensor and design procedure of rotary encoder are examined, accompanied by design error analysis.

5.2.1 Theory

Figure 5.1 represents the rotary encoder in which the hatched ring with a width of d is divided into two spirals, reflecting and transmitting, by means of a curve which changes with the rotation angle, $r(\theta)$. The yellow one (shaded area), is covered by a reflective material to reflect the light and the

white area is transparent to transmit the light. A light beam with an incident angle of 45° is projected on to the hatched ring (Figure 5.1). The sampling light beam on the rotary encoder has a rectangular cross section with a small width of w and length of 1.1d, so that the ring width of d is completely illuminated by light. Hence, the light applied to the rotary encoder is sampled according to the rotary encoder design and consequently reflected partially with the remaining light being transmitted. The reflected and transmitted light powers are captured by two photo-detectors through plano-convex lenses. The design of the rotary encoder is done in such a way that the reflected and transmitted powers, as well as the ratio of difference and sum of these two powers, have a linear relation as a function of the rotation angle.

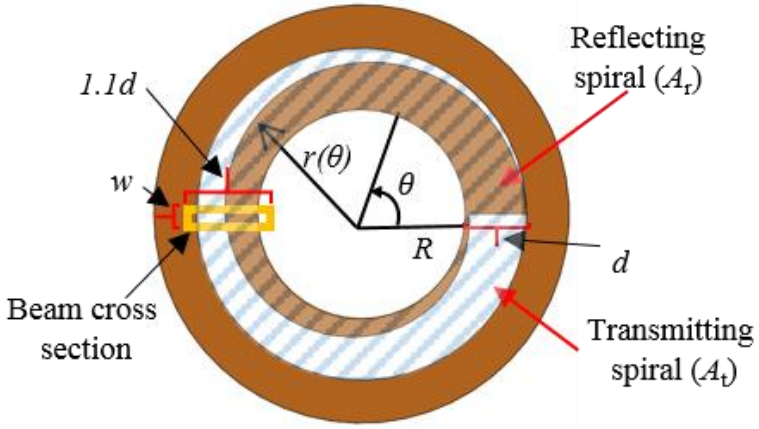

Figure 5.1 the rotary encoder design with the one-ring pattern.

5.2.2 Device design

The target of the design is to achieve a sensor response with the following characteristics:

- A one to one linear relation is required for the transmitted and reflected powers as a function of rotation angle.
- A one-to-one linear relation is needed between the sensor response and the rotation angle [17], [63].
- Ratio-metric function to result in a self-referenced sensor

In Chapter 4, we proposed an optical rotary sensor (ORS) for avionics applications in which the sensor response is obtained from the ratio of transmitted and reflected powers. Although the sensor response has a linear relation with the rotation angle, the transmitted and reflected powers changed nonlinearly vs. the rotation angle. Hence, the accuracy of power measurement diminished

significantly with increasing angle as the error of fabrication increase vs. angle because of the need to make patterns with higher accuracy. Since the fabrication error has a nonlinear relation vs. rotation angle and increases for higher angles (Note that the fabrication error is proportional to $(1+\theta)^2$ as per Eq. 4.11), resulting in a sensor with a severely restricted operating range of <180°.

In the new design, to increase the operating range of the sensor, linear patterns (and accordingly linear transmission and reflection powers) vs. the rotation angle are used to reduce the impact of fabrication errors. Hence, a linear sensor response with linear transmission and reflection powers is created when we select the sensor response as the ratio of the difference to the sum of two powers as per Eq. 5.1. Hence, the effect of source attenuation on the difference of reflected and transmitted powers in the numerator is canceled by the sum of two powers in the denominator of Eq. 5.1.

$$s(\theta)=\frac{\Delta P}{\sum P}=\frac{P_t(\theta)-P_r(\theta)}{P_t(\theta)+P_r(\theta)} \qquad \text{Eq. 5.1}$$

Following our earlier work in Chapter 4, we briefly introduce the analysis of the transfer function of the new design. Assuming a uniform source with the optical intensity of I0, the reflected and transmitted powers are proportional to the reflection and transmission areas, respectively. Hence, the sensor response is defined as Eq. 5.2:

$$s(\theta)=\frac{P_t(\theta)-P_r(\theta)}{P_t(\theta)+P_r(\theta)}= \frac{I_0.A_t(\theta)-I_0.A_r(\theta)}{I_0.A_t(\theta)+I_0.A_r(\theta)}=\frac{A_t(\theta)-A_r(\theta)}{A_t(\theta)+A_r(\theta)} \qquad \text{Eq. 5.2}$$

where $A_r(\theta)$ and $A_t(\theta)$ are the reflection and transmission areas, respectively, and θ is the angle of rotation. As total sampled area of the reflection and transmission is $A_r(\theta)+A_t(\theta)=w.d$, the sensor response has a linear relation with the reflection area as Eq. 5.3.

$$s(\theta)=\frac{(w.d-A_r(\theta))-A_t(\theta)}{w.d}=1-\frac{2}{w.d}.A_r(\theta) \qquad \text{Eq. 5.3}$$

In addition, the reflection area has a linear relation with $r(\theta)$ since it is calculated as $A_r(\theta)=(r(\theta)-R).w$. Consequently, the sensor response, $s(\theta)$, has a linear relation with the

rotation angle if $r(\theta)$ has a linear relation with respect to the rotation angle. Therefore, $r(\theta)$ is selected as Eq. 5.4 which divides the hatched ring in Figure 5.1 into reflection and transmission regions.

$$r(\theta) = R + d - K.d.\theta \qquad \text{Eq. 5.4}$$

$$A_r(\theta) = (r(\theta) - R)w = w.d(1 - K.\theta) \qquad \text{Eq. 5.5}$$

$$A_t(\theta) = (R + d - r(\theta))w = w.d.K.\theta \qquad \text{Eq. 5.6}$$

Assuming ideal conditions, i.e. a uniform light beam with a negligible width, and no transmission or reflection losses, the reflected and transmitted powers are proportional to the reflection and transmission areas, as follows:

$$P_r(\theta) = P_0(1 - K.\theta) \qquad \text{Eq. 5.7}$$

$$P_t(\theta) = P_0.K.\theta \qquad \text{Eq. 5.8}$$

Where P_0 is the total power in the area $w.d$ and equal to P_t+P_r. Hence, the sensor response is calculated as:

$$\begin{aligned} s(\theta) &= \frac{\Delta P}{\sum P} = \frac{P_t(\theta) - P_r(\theta)}{P_t(\theta) + P_r(\theta)} \\ &= \frac{P_0.K.\theta - P_0(1 - K.\theta)}{P_0.K.\theta + P_0(1 - K.\theta)} = \frac{P_0.(2K.\theta - 1)}{P_0} \\ &= 2K\theta - 1 \end{aligned} \qquad \text{Eq. 5.9}$$

Eq. 5.9 depicts a linear correlation between the sensor response and the angle of rotation which demonstrates that the characteristic of the sensor is a one-to-one linear function without hysteresis between measurand and the response of sensor [17], [63]. Moreover, reliability, which is an important factor for avionics applications has also been met as the effect of source fluctuation, the changes in P_0, in the numerator and the denominator, cancel each other automatically, as shown in Eq. 5.9.

Figure 5.2 shows the normalized reflected and transmitted powers (left axis) and the sensor response (right axis) in the ideal conditions, assuming a uniform light beam with a negligible width.

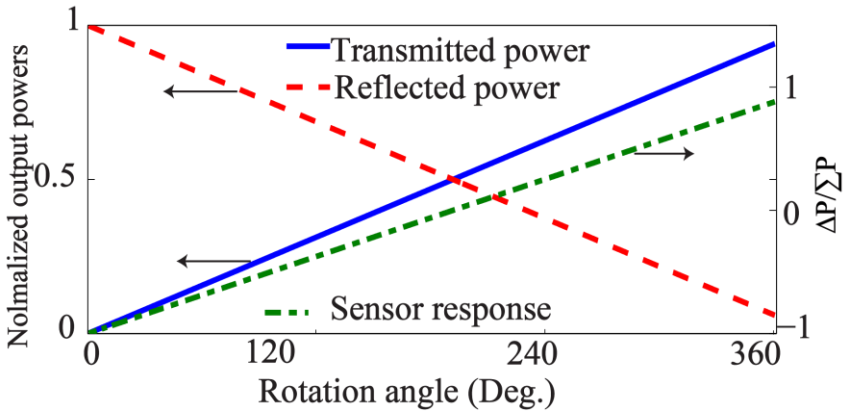

Figure 5.2 Normalized output powers (left axis), and the sensor response, $\Delta P/\sum P$, defined as per Eq. 5.9 (right axis).

Although a uniform optical source has been assumed in the calculation of Eq. 5.7 and Eq. 5.8, real sources are non-uniform and the distribution of light on the rotary encoder is therefore not uniform either. Light power distribution is normally found to be Gaussians in 2D. In the case of our sensor, an angle exists between the propagation direction of the Gaussian beam and rotary encoder; therefore, this source is henceforth called an expanded Gaussian source. Hence, the non-uniform source results in a nonlinear error although a one-to-one linear relation is needed between the sensor response and the rotation angle [63]. To exclude the non-linearity in the sensor response, applying a multi-ring pattern leads to a good approximation of a uniform source in each sampling ring, which samples the source in different spatial regions.

In this scenario, and based on the principle of insensitivity to power variations, the hatched ring in Figure 5.1 should include several patterned-rings to sample the beam at spatially different locations transversely. Based on the theoretical analysis, the minimum number of patterned-rings must be six to reduce the error of the source non-uniformity on the sensor response as will be discussed in Design error analysis subsection 5.2.3. C. Moreover, to decrease the error of fabrication, the reflected areas of each two neighboring rings are connected to each other as per six-ring pattern depicted in Figure 5.3 (a). In this approach, the number of etching edges reduces from 12 to 8. From the unwound the patterned-ring design in this paper and Chapter 4, respectively as shown in Figure 5.3 (b) and (c), one can apparently see the difference between these two designs. Patterns

of Chapter 4 changes nonlinearly (Figure 5.3 (c)) whereas the patterns in this Chapter change linearly vs. rotation angle (Figure 5.3 (b)).

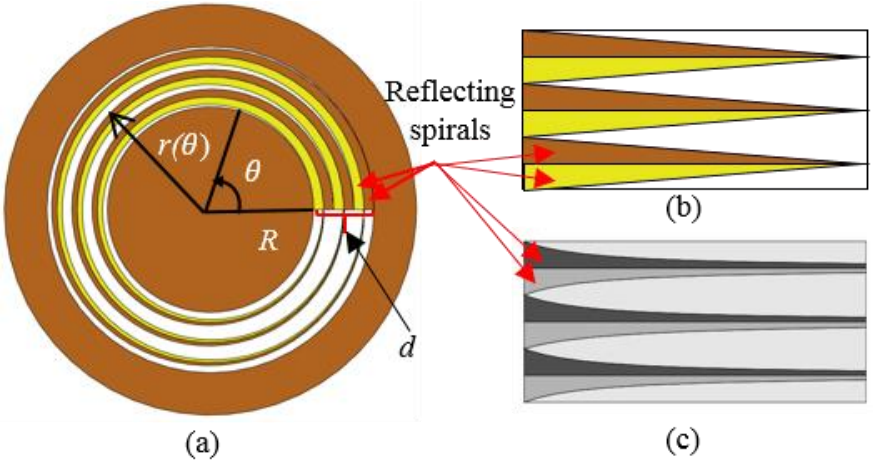

Figure 5.3 (a) Rotary encoder design with a six-ring pattern to solve the nonlinearity error coming from the non-uniform source, (b) Opened multi-patterned-ring design in this paper, and (c) Opened multi-patterned-ring design in Chapter 4.

Figure 5.3 (a) is named as six-ring pattern design since it has six alternating curves with rotation angle as Eq. 5.10 and Eq. 5.11, respectively, for j=1,2,3.

$$r_{2j-1}(\theta) = R + (j-1).\frac{d}{3} + K.\frac{d}{6}.\theta \qquad \text{Eq. 5.10}$$

$$r_{2j}(\theta) = R + j.\frac{d}{3} - K.\frac{d}{6}.\theta \qquad \text{Eq. 5.11}$$

The curvature constant, K, should be selected in such a way that the patterns starting at 0° cover the smallest width at 360° to have the full operating range. In fact, the operating range is inversely proportional to K, and consequently, K should have a minimum value to achieve the maximum operating range. In addition, the smallest width of the patterns over 360° should have a dimension many times larger than the operating optical wavelength to avoid diffraction effects. By selecting K=0.15, the smallest width of the pattern at the rotation angle of 360° is 60μm, 92 times larger than the operating wavelength of 633nm.

However, the sensor sensitivity is proportional to K which is calculated by differentiating Eq. 5.9 with respect to θ:

$$Sensitivity = \frac{ds(\theta)}{d\theta} = 2.K.\frac{\pi}{180}. = 5.2\text{mW/W / deg}. \qquad \text{Eq. 5.12}$$

Note that the unit W/W (referring to the optical powers) is equal to the unit V/V (referring to the electric voltages) as the electric voltage is proportional to the optical power at a given wavelength by the gain of $\mathrm{R}.\Re$ as per Eq. 5.13:

$$V = \mathrm{R}.I_{\mathrm{ph}} = \mathrm{R}.(\Re.P) \qquad \text{Eq. 5.13}$$

where I_{ph} is the produced photocurrent in the photodiode, $\Re$ is the responsivity of photodiode [68], P is the optical power, V is the electric voltage and R is the gain of the trans-impedance amplifier. Hence, when two optical powers are converted to electric voltages with the same gain of $\mathrm{R}.\Re$, the sensor response and accordingly the sensitivity is 5.2mV/V/deg.

In [69], the sensitivity of RVDT is reported as 1.4 mV/V/deg., 3.7 times less than the sensitivity of our sensor, 5.2mV/V/deg. Additionally, the reported sensitivity of RVDTs from Mouser Electronics Company [70] is 2.2mV/V/deg. proving our sensor is 2.3 times more sensitive. In summary, there is a trade-off between the operating range and the sensitivity of the sensor and we sacrifice sensitivity to have the full operating range. However, the sensitivity of our sensor is 5.2mV/V/deg. which is more than twice the sensitivity of RVDTs.

5.2.3 Design error analysis

As described in the section on Device design, because of the expanded Gaussian distribution of optical sources; a multi-ring pattern scheme is employed to obtain approximate uniformity in power distribution of each patterned ring. However, a non-uniform source with a multi-ring pattern design brings slight errors in the angle measurement. Hence, the analyses are made for the error in the rotation angle resulting from the expanded Gaussian sources and two designs: one-ring pattern (Figure 5.1) and six-ring pattern, Figure 5.3 (a). The *Error* is calculated as:

$$Error = (\theta_{\mathrm{EGS}} - \theta_{\mathrm{i}}).\frac{180}{\pi}.\frac{100}{Range} \qquad \text{Eq. 5.14}$$

where θ_{EGS} and θ_i are rotation angles assuming an expanded Gaussian beam and an ideal source, demonstrated in Eq. 5.15 and Eq. 5.16, respectively. To convert radians to degrees and to calculate the full range percentage error, 180/π and 100/*Range*, respectively, are multiplied into *Error*.

$$\theta_{EGS} = (s_{EGS}(\theta)+1)/2K \qquad \text{Eq. 5.15}$$

$$\theta_i = (s_i(\theta)+1)/2K \qquad \text{Eq. 5.16}$$

where $s_{EGS}(\theta)$ and $s_i(\theta)$ are the sensor responses for expanded Gaussian and ideal source, respectively. Hence, the full range error in percentage is calculated as:

$$Error = \frac{18000}{2.\pi.K.Range}\left[s_{EGS}(\theta) - s_i(\theta)\right] \qquad \text{Eq. 5.17}$$

The number of patterned rings is increased to the point that the error of non-uniform source is reduced to 0.2% over the full range, five times less than the total acceptable error, 1% over the full range. In fact, we keep the non-uniform source error much lower than the total acceptable error because of the need to accommodate other sources of error, mechanical and fabrication.

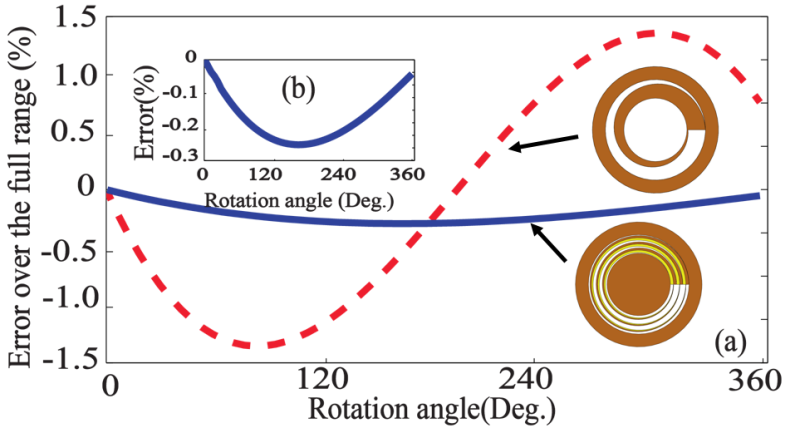

Figure 5.4 (a) Error of non-uniform source (expanded Gaussian source) vs. rotation angle for two designs: one-ring pattern and six-ring pattern. (b) The error of non-uniform source for the six-ring pattern is zoomed.

Figure 5.4 (a) shows the error of a non-uniform source (expanded Gaussian source) vs. rotation angle for two designs: one-ring pattern and six-ring pattern. The six-ring pattern design error with the expanded Gaussian source is zoomed in Figure 5.4 (b). The full range RMS error of the non-

uniform source for the one-ring pattern design and the six-ring pattern design are 1% and 0.2%, respectively. The six-ring pattern design error with the non-uniform source (0.2%) is five folds smaller than RVDT's error (1%). The error of non-uniform source could be decreased by increasing the number of multi-ring pattern design. For instance, eight-patterned-rings design introduces a full range error of just 0.1%. Please note that the diffraction effect does not introduce an error into the measurement as the smallest width of the patterns are much larger than the operating wavelength and the lenses in the detection sides are very close to the rotary encoder.

Another source of error is the width of beam cross section. It is worth noting that the width of beam cross section is the same as the slot width and the length of beam cross section is ~1.4 times the slot width, as there is an angle of 45° between the slot and rotary encoder. The width of the beam cross section adds power to the transmitted power and subtracts it from the reflected power as the encoder pattern in the width of w. To have a better understanding of that, note that at 0°, the transmitted power should be zero based on the theory presented in Figure 5.2, while in practice, a small amount of power is added to the transmitted power because of the width of beam cross section. The power added to/subtracted from transmitted/reflected powers is constant versus rotation angle as the patterns described in Eq. 5.10 and Eq. 5.11 change linearly with the rotation angle. Moreover, the length of beam cross section, $1.1d$, is larger than ring width, d, adding constant power to the reflected power. The constant errors introduced by width and length of beam cross section can be easily corrected by subtracting constant numbers from the normalized transmitted and reflected powers. The constant number for correction of the transmitted power is calculated as the transmitted power at 0° normalized to P_0. The constant number for the correction of the reflected power is calculated as a subtraction of P_0 from the total power after the slot normalized to P_0.

The width of the beam cross section also limits the operating range of the sensor because of high error (full range error of more than 1%) at angles just before reaching 360°. Figure 5.5 shows the error resulting from the width of beam cross section vs. rotation angle, from 355° to 360°. This error happens when one edge of the beam cross section is at an angle smaller than 360° while its other edge is at an angle beyond 360°, as shown at the bottom of Figure 5.5. With a beam cross section of width 500μm, its edge enters the angle beyond 360° (i.e. >0°) while its other edge is at 356.5° where the error increases substantially thereafter. Hence, the operating range of the sensor is from 0° to at 356.5°.

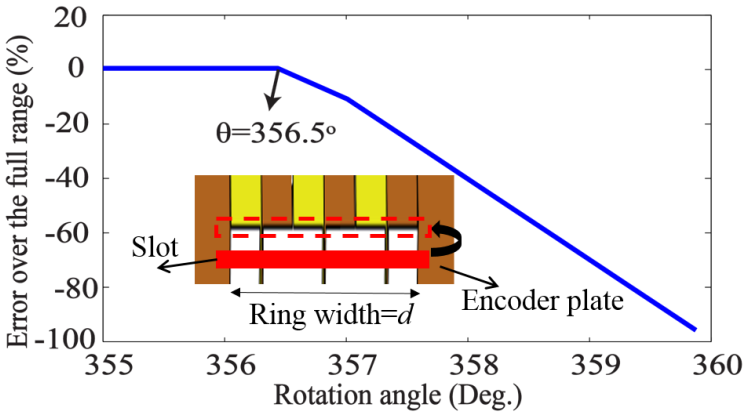

Figure 5.5 Error of width of beam cross section vs. rotation angle.

In terms of diffraction, the width of beam cross section (slot) was selected to be 0.5mm or 500µm which is many times larger than the operating wavelength of the source laser, 0.633 µm, and accordingly does impact the measurements.

5.3 Results and analysis

In this section, one can find the experimental setup used for three experiments to verify the sensor response, the operating range, and the sensor independence from source power fluctuations. Next, the sources of error are analyzed. Finally, various specifications of the rotary sensor proposed in this work are compared with our previous design [17] and with RVDTs and optical sensors in the market.

5.3.1 Experimental setup

The 3-dimensional test setup (The same as the setup used in Chapter 4) is shown in Figure 5.6. The source is a HeNe laser which is followed by two cylindrical lenses for manipulation of the beam diameter in the horizontal direction. The produced collimated beam has the semi-major and semi-minor axes of 4mm and 0.4mm, respectively, which covers the rectangular slot of 3.9mm x 0.5mm. The source power after the slot is 1.5mW. The light arriving at the rotary encoder is reflected and transmitted as per Eq. 5.6 and Eq. 5.7, respectively. Reflected and transmitted light powers are directed by two plano-convex lenses (PCX) onto the photo-detectors (PDs).

Specifications of different parts of the rotary sensor including the rotary encoder and slot are summarized in Table 5.1.

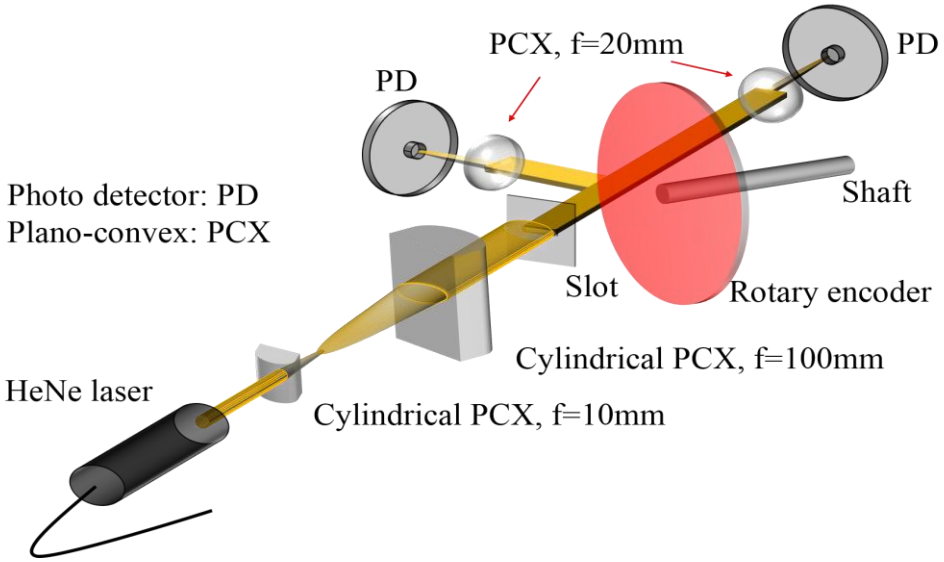

Figure 5.6 Examination setup to test the ORS. An elliptically collimated beam is produced by means of two cylindrical lenses and passed through a slot. Reflecting/transmitting from/to OSR encoder, the light powers are captured and launched into PDs.

Table 5.1 Rotary sensor specification

Parameter	Value
Inner radius of ring in rotary encoder	R=8.5mm
Width of ring in rotary encoder	d=5mm
Thickness of rotary encoder substrate	1mm
Curvature coefficient	K=0.15
Rotary encoder substrate material	B270
Reflective material deposited partially on the rotary encoder	Aluminum
Angle of input (AOI) of the beam to the rotary encoder	45°
Length of light beam cross section	1.1d=5.5 mm
Width of light beam cross section	w=0.5mm
Length of slot	1.1d×cos(AOI)=3.9 mm
Width of slot	w=0.5mm
Slot material	Ceramic

In the prototyping of our sensor into a small housing, we use a small laser diode with 5.6mm package type, small photodiodes with 10mm package type, and plano-convex lenses with the focal

length of 12mm. The related circuits of two PDs and micro-controller will be integrated into a single printed circuit board (PCB) resulting in a very small housing.

5.3.2 Sensor response

Figure 5.7 (a) shows the reflected and transmitted light powers vs. rotation angle in the experiment. It also illustrates the sensor response, $\Delta P/\sum P$, calculated from measured data. Figure 5.7 (b) shows the calculated angle of rotation and percentage error vs. rotation angle.

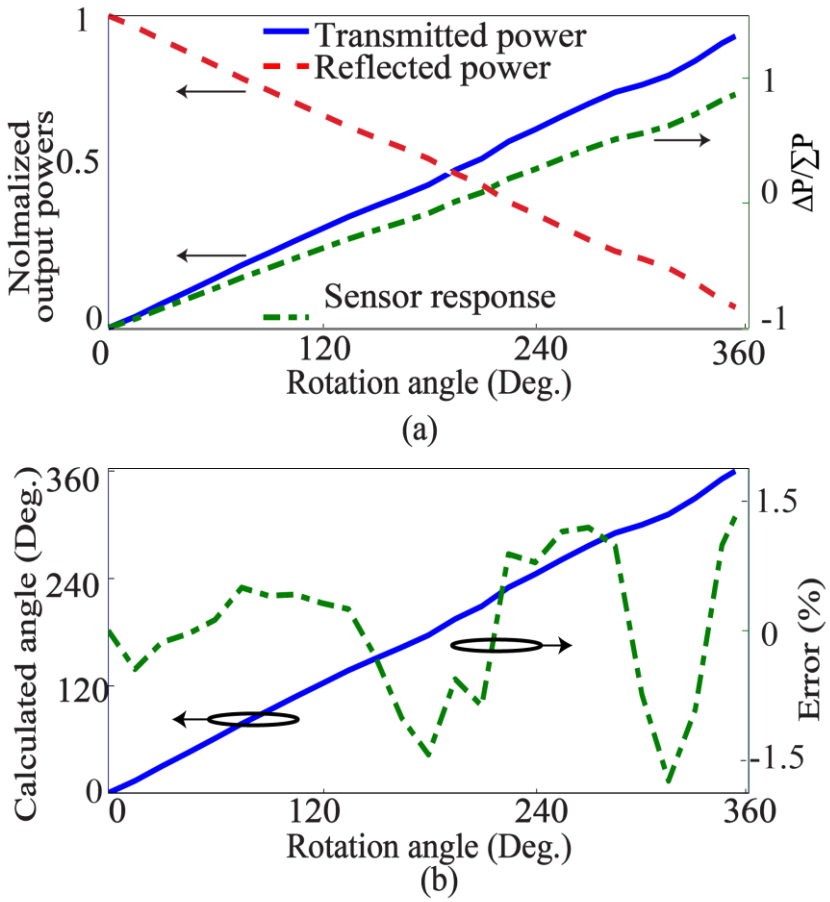

Figure 5.7 (a) Normalized output powers in the experiment (left axis) and ΔP/∑P vs. rotation angle (right axis) and (b) calculated angle of rotation (left axis) and percentage of error (right axis) vs. rotation angle.

The error is calculated as:

$$Error = (\theta_{EXP} - \theta_i).\frac{180}{\pi}.\frac{100}{Range} \qquad \text{Eq. 5.18}$$

where θ_{EXP} and θ_i are rotation angles in the experiment, and under ideal condition, as Eq. 5.19 and Eq. 5.20, respectively.

$$\theta_{EXP} = (s_{EXP}(\theta) + 1) / 2K \qquad \text{Eq. 5.19}$$

$$\theta_i = (s_i(\theta) + 1) / 2K \qquad \text{Eq. 5.20}$$

where $s_{EXP}(\theta)$ and $s_i(\theta)$ are the sensor responses in the experiment and under ideal condition, respectively. Hence, the full range % error is:

$$Error = \frac{18000}{2.\pi.K.Range}\left[s_{EXP}(\theta) - s_i(\theta)\right] \qquad \text{Eq. 5.21}$$

The full range RMS error is calculated to be 0.8%. Sources of error will be analyzed in subsection 5.3.5, Error analysis.

To determine the sensitivity of the sensor, the slope of the sensor response curve is calculated from the curve in Figure 5.7 (a) (on the right y-axis) and found to be 5.2mV/V/deg. Compared to RVDTs in [70] and [69], our sensor is 2.3 and 3.7 times more sensitive, respectively.

5.3.3 Operating range

To specify the sensor's operating range, one needs to measure the reflected and transmitted light powers from 355° to 360° with small changes to determine where the error in the angle measurement exceeds the threshold of 0.8% over the full range. Figure 5.8 presents the reflected and transmitted light powers vs. Rotation angle from 355° to 360° and error in the measurement of the rotation angle. As the full range error after 356.5° exceeds 0.8%, the operating range of the sensor is determined from 0° to 356.5°.

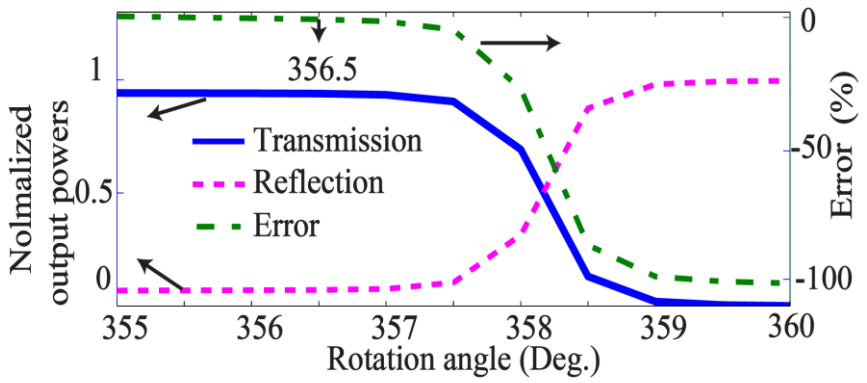

Figure 5.8 Normalized reflected and transmitted light powers (left-axis) and error (right-axis) in the measurement of rotation angle vs. rotation angle from 355° to 360°. This shows that the error after 356.5° is very high which results in the limitation of range to 356.5°.

5.3.4 Self-referencing property

Examining the sensor stability vs. beam power fluctuations, the sensor response is assessed by adding two absorptive neutral density filters into the optical setup. The optical densities (OD) of filters are 0.1 and 0.2 which transmit 79% and 63% of light, respectively.

Figure 5.9 (a)-(c) shows reflected and transmitted light powers, the sensor response and the calculated angle of rotation vs. the measured rotation angle, respectively, for three setup cases: without a filter, OD=0.1, and OD=0.2.

The measured output powers with OD=0.1 and OD=0.2 are reduced to 79% and 63% of the output power in the case no filter, respectively. Figs. 9 (b) shows that the sensor is independent of the source power fluctuation, as the effect of the loss in the input power affects the reflected and transmitted light powers equally and their effect are canceled in the ratiometric sensor response as Eq. 5.9. Figure 5.9 (c) shows the full range % error for three cases: no filter, OD=0.1, and OD=0.2.

Full range RMS error for the three cases remains at 0.8%. The small difference between the errors of three cases come from mechanical errors: upward/downward linear/angular displacement. Another justification for the small increase in the error by OD=0.1 and OD= 0.2 is due to the noise (such as dark noise) in low signal measurement.

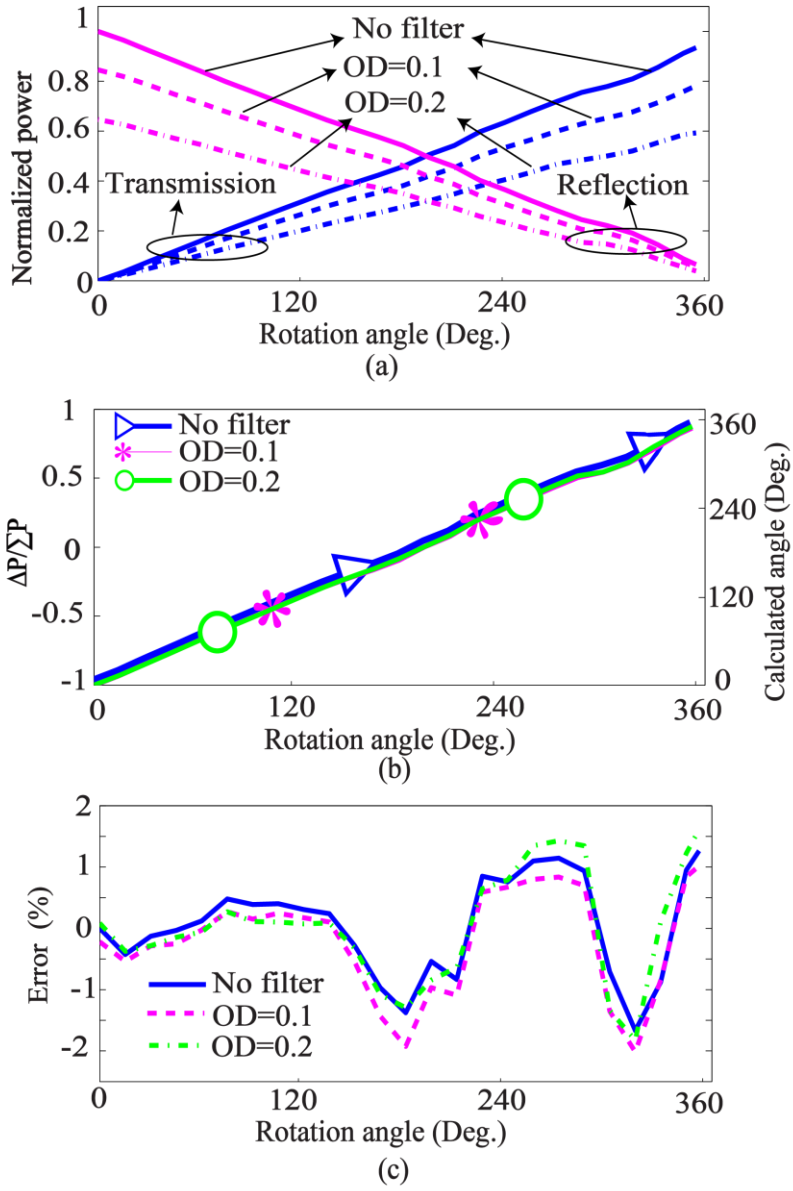

Figure 5.9 For different input powers on the rotary encoder: (a) Reflected and transmitted light powers vs. rotation angle, (b) sensor response: ΔP/∑P and calculated angle of rotation vs. angle of rotation, and (c) full range error in percentage vs. rotation angle.

5.3.5 Error analysis

Sources of error are through the non-uniform source, mechanical displacements, and fabrication imperfections. As explained in subsection 5.2.3, Design error analysis, 0.2% of error comes from the non-uniform source and thus 0.6% of error comes from mechanical displacements and fabrication imperfection.

Mechanical errors are analyzed in two parts resulting from linear and angular displacements. We estimate that rotational eccentricity of the sensor mask is not significant; however, it is possible that the mask may be displaced at most by ±100 microns from the light beam, or that the mask could be tilted by as much as ±0.1°. The influence of each misalignment is now calculated in turn.

Figure 5.10 (a) and (b) show the full range % error for 100μm of upward and downward linear displacements. Figure 5.10 (c) and (d) show the full range error in percentage for 0.1° of upward and downward angular displacements. In the case without displacement, a constant power is added to the reflected power as the length of beam cross section is larger than the ring width, *d*, which is corrected by subtracting the normalized reflected power by a constant number. By linear up and down displacement of the rotary encoder the added power to the reflected power changes because of a relative shift in the Gaussian beam, as shown at the top of Figure 5.10 (a) and (b). However, this error is very low as it increases the full range error by only 0.01% which shows that normally expected linear displacement does not decrease the accuracy of the sensor. By the angular displacement of the rotary encoder (Tilt as shown in Figure 5.10 (c) and (d)), the added power to the reflection changes not only because of the shift in the Gaussian beam but also because of the expansion of Gaussian beam with a new angle. The full range error is altered by 0.1% induced from this mechanical misalignment. Comparing Figure 5.9 (c) and Figure 5.10 it is seen that the position of the rotary encoder in the case of OD=0.1 compared to no filter case is angularly displaced downward and the position of the rotary encoder in the case of OD=0.2 compared to OD=0.1 is angularly displaced upward. The mechanical error may be eliminated by covering the outside edge of the ring patterns in Figure 5.3 (a) by an absorptive coating to avoid the addition of extra power in reflection from arriving at the PD. The classical way to make an absorptive structure is to use black absorbing layers with the thickness of few hundred micrometers. In comparison, metal-dielectric structures can be made with the thickness of few hundred nanometers [71], [72]. For example, a black film composed of 4 layers of metal and dielectric with the total thickness of 270nm results in reflectance of less than 1% for normal incidence [71]. We can select SiO2/Cr/SiO2/Al as dielectric and metal layers and optimize their thickness for an input angle of 45° and operating wavelength of red light using OpenFilter software [66]. The black film of SiO2/Cr/SiO2/Al with the thicknesses of 113nm/7nm/123nm/100nm, respectively, will result in the absorption of 99.7%. The mechanism of light loss is due to the reflectance and absorbance of metal layers and the dielectric layers adjust the phases of the reflected light. Please note that the

transmittance of the black film is zero as the thickness of Al layer is 100nm [66]. The thickness of this filter blocks the transmitted power which results in a negligible full range error of 0.001%.

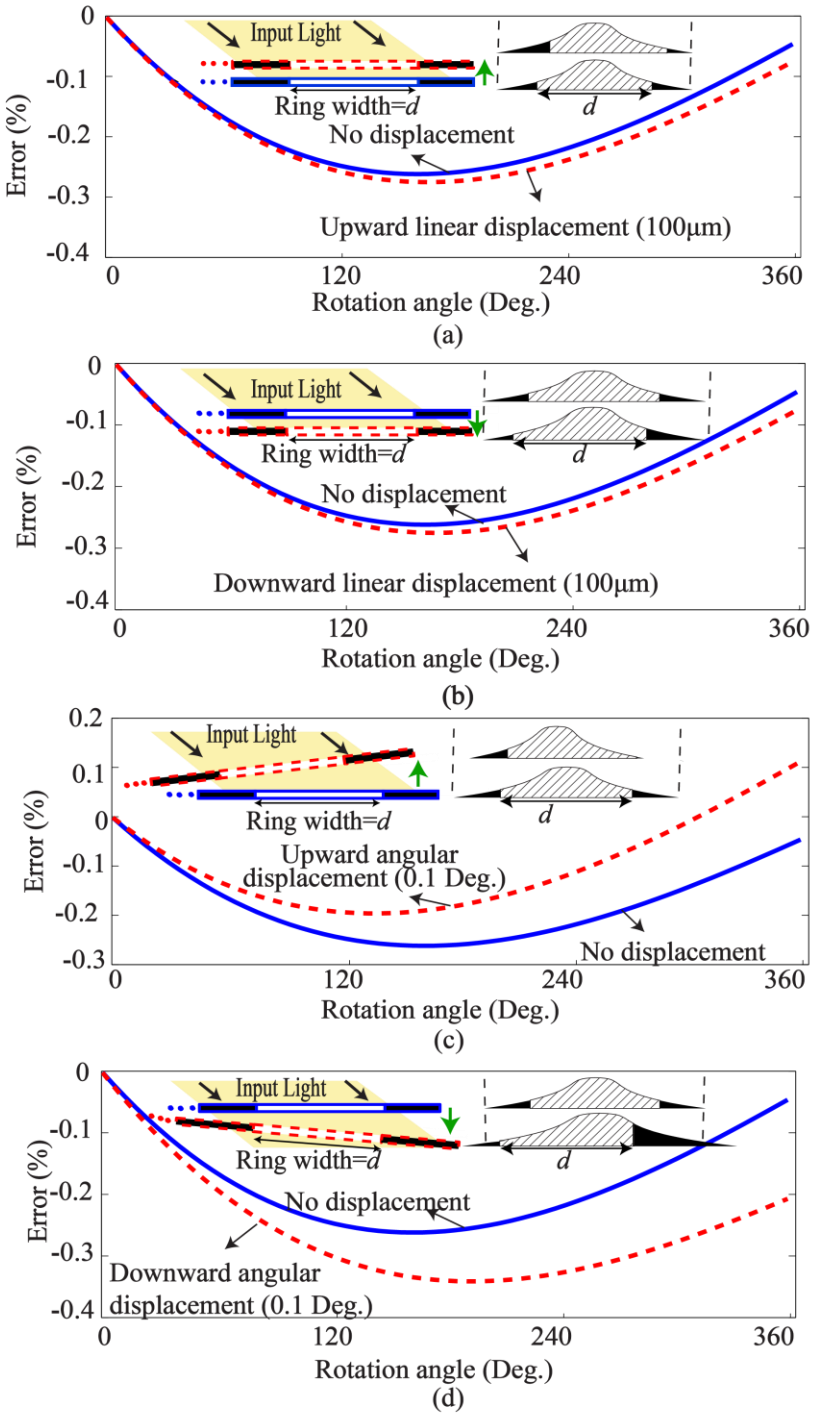

Figure 5.10 Full range error for (a) upward linear displacement, (b) downward linear displacement, (c) upward angular displacement, and (d) downward angular displacement.

The remaining error of 0.5%, comes from fabrication imperfections which include the low resolution of fabrication of the patterns shown in Figure 5.3 (a). To calculate the resolution of the fabricated rotary encoder based on micro-fabrication accuracy, we differentiate the width of each pattern, $w_j(\theta) = r_{2j}(\theta) - r_{2j-1}(\theta) = d.(1 - K.\theta)/3$, with respect to the angle of rotation as Eq. 5.22 for j=1,2,3:

$$\frac{dw_j(\theta)}{d\theta} = \frac{d\left\{r_{2j}(\theta) - r_{2j-1}(\theta)\right\}}{d\theta} = K.\frac{d}{3}.\frac{\pi}{180} \qquad \text{Eq. 5.22}$$

where K=0.15 and d=*5mm* and the conversion to degrees has been made in $d\theta$. Hence, the full range error of 0.5% shows that the resolution of fabrication, dw_j, is 7.7μm using Eq. 5.22. In other words, the width of patterns of Figure 5.3 (a) are fabricated with the error of 7.7μm. This means the etching accuracy of each edge is 3.8μm which was confirmed by verifying the fabricated mask under the microscope.

5.3.6 Comparison with the design of Chapter 4

In Chapter 4, the curve, $r(\theta)$, to divide the ring with width d into areas of reflection and transmission, changes nonlinearly with the rotation angle. Therefore, the reflected and transmitted light powers have a nonlinear relation to the rotation angle. Although this nonlinear curve results in a linear sensor response, it leads to a nonlinear error resulting from the width of the beam cross section and consequently needs correcting for offset and inclination of the sensor. Additionally, fabrication of nonlinear curves results in further accuracy reduction with rotation angle which consequently limits the operating range of the sensor to 180°.

In this work, the curve, $r(\theta)$, to divide the ring with width d into two areas of reflection and transmission, changes linearly with the rotation angle. This not only results in a linear sensor response but also leads to the constant fabrication accuracy and constant error coming from the beam width cross section. Constant fabrication accuracy allows the fabrication of a rotary sensor with a broad operating range from 0° to 356.5°. Moreover, because of the constant beam width cross section error, a constant power is added to the transmitted power and subtracted from the reflected power. This error can be easily corrected by subtracting/adding a constant number to the normalized transmitted/reflected powers.

Table 5.2 Comparison of two designs, in Chapter 4 and in this paper.

Parameter	Chapter 4	New Design (This work)
Pattern formula, $r(\theta)$	$R+d/(1+\theta)$	$R+d-0.15d.\theta$
Transmitted power, $P_t(\theta)$	$P_0.\theta/(1+\theta)$	$0.15P_0.\theta$
Reflected power, $P_r(\theta)$	$P_0/(1+\theta)$	$P_0(1-0.15.\theta)$
Sensor response, $s(\theta)$	$P_t(\theta)/P_r(\theta)=\theta$	$\Delta P/\sum P=0.3\theta-1$
Error of beam width cross section	Nonlinear error vs. rotation angle	Constant error vs. rotation angle
Full range error of non-uniform source	0.2% over 180°	0.2% over 356.5°
Sensitivity, $ds(\theta)/d\theta$	17.5mV/V/deg.	5.2mV/V/deg.

The advantage of the previous design [17] vs. the new design is its higher sensitivity in which the former has a sensitivity of 17.5mV/V/deg. and the latter has the sensitivity of 5.2mV/V/deg. Different parameters of our new and previous rotary encoder design [17] are summarized in Table 5.2.

5.3.7 Comparison of our sensor, RVDTs, and optical sensors

Providing high reliability for avionics applications, the proposed ORS and the RVDT both are designed ratio-metrically in which the sensor response is calculated as the ratio of two powers/voltages to remain independent of the source power/voltage variations.

RVDTs have the operating range of -40° to +40° with the full range error of 1%. However, the proposed rotary sensors in Chapter 4 and in this work have a much higher operating range, of 180° and 356.5° with an accuracy of 0.5% and 0.8% over the full range, respectively. In addition, the highest sensitivity of RVDTs is less than 2.2mV/V/deg., while the sensitivity of our previous and new designs are 17.5mV/V/deg. and 5.2mV/V/deg., respectively. Specifications of our rotary sensors, RVDTs, and optical sensors are summarized in Table 5.3.

Optical sensors found in the literature are very sensitive, accurate and have full operating range. Note that the sensitivity of digital sensors is closely related to the resolution [73]. However, they work are based on only reflected or transmitted powers [10], [12], [14], [52], [53], [65], [74] where there is no reference signal to correct for the nonlinearity of sensor response from the non-

uniformity and power variations of the light source. Their inability to be independent of the source instability or degradation make them unreliable for avionics applications, as optical sources degrade over long periods of time.

Table 5.3 Comparison of our sensors, RVDT, and optical sensors.

Parameter	Reliability	Accuracy	Range	Sensitivity	A/D
RVDT	Ratio-metric sensor response	1%	80º	<2.2 mV/V/deg.	A
Chapter 4	Ratio-metric sensor response	0.53%	180º	17.5 mV/V/deg.	A
This paper	Ratio-metric sensor response	0.8%	365.5º	5.2 mV/V/deg.	A
Optical sensors	Work just based on transmission or reflection	Better than 1%	360º	30bits	D
A: Analog, D: Digital					

5.4 Summary

In this Chapter, we designed, fabricated and tested an absolute full range rotation sensor for aerospace applications. Delivering high reliability for avionics applications, it was designed in such a way that the ratio of the difference and sum of reflected and transmitted powers determines the sensor response. Therefore, the effect of source fluctuation is canceled in the numerator and denominator making the sensor independent from the source. To fabricate the rotary encoder, a circular glass substrate with the diameter of 27mm was used and then coated by anti-reflection layers of Ti3O5 and SiO2 to provide transmission of more than 98% for an input angle of 45° with a bandwidth of 50-nm for a wavelength span from 620nm to 670nm. Micro-fabrication technology was employed to deposit aluminum on the coated substrate. Experimental results showed that the operating range of the sensor is from 0° to 356.5° with an accuracy of 0.8% over the full range.

Moreover, it was shown that the sensor is self-referencing and that variation of the input source power does not affect the sensor response. Comparison of our two works, the previous and new designs, shows that the former is more sensitive, whereas the latter has a larger operating range. Finally, the comparison of our sensor with RVDTs which are currently used in the aviation industry was presented showing that our sensor is twice as sensitive and has a 4x larger operating range. In addition, the comparison of our sensor with the optical sensors in the literature shows that our optical sensor is potentially more reliable as it works on a ratiometric principle. The related work was submitted to [75], [76].

5.5 Future works related to this design

5.5.1 Lower range with higher sensitivity

The design verified in this chapter works for the operating range of 0° to 356.5°. For lower operating ranges, the sensitivity and accuracy could be increased as there is a trade-off between operating range and sensor sensitivity. Sensor sensitivity for operating range of 356.5° and a constant factor of K=0.15 was calculated as 5.2 $mWW^{-1}deg^{-1}$. In lower operating range applications, the sensor sensitivity could be increased by increasing constant factor K. The designs for the operating ranges of 60° and 120° are shown in Figure 5.11 (a) and (b), respectively. In the former and the latter, K is selected as 0.9 and 0.45, respectively, resulting in the sensitivity of 31.2 $mWW^{-1}deg^{-1}$ and of 15.6 $mWW^{-1}deg^{-1}$.

Figure 5.11 (a) 60-degree pattern design with K=1.8 and (b) 120-degrees pattern design with K=0.9.

5.5.2 Optical linear displacement encoder

The same idea of the design procedure proposed in this chapter for the optical rotary displacement encoder could be used for an optical linear displacement encoder as shown in Figure 5.12. A strip with the width of *d* and length of *R* should be patterned to encode the displacement into the two areas of reflection and transmission. Supposing a uniform light source, the reflection and transmission areas are proportional to the reflected and transmitted powers, respectively. Red rectangular with the width of *w* shows a beam cross section on the encoder at point *x*. Unknown curve, *y*(*x*), should be determined based on the sensor requirements explained in Section 3.2.2.

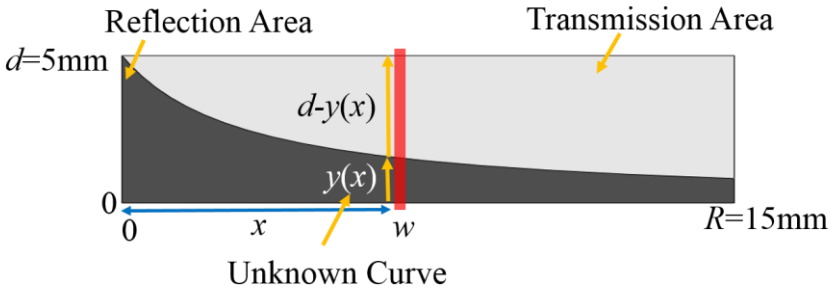

Figure 5.12 Linear displacement encoder.

We selecting a linear curve, *y*(*x*), as Eq. 5.23:

$$y(x) = d(1 - K_1.x) \qquad \text{Eq. 5.23}$$

Suppose that the sensor response should be extracted from the ratio of subtraction to the summation of transmitted and reflected light powers, $P_t(x)$ and $P_r(x)$, respectively:

$$s(x) = \frac{P_t(x) - P_r(x)}{P_t(x) + P_r(x)} \qquad \text{Eq. 5.24}$$

Reflected and transmitted powers are calculated as follows supposing light distribution with the uniform intensity of I_0:

$$P_r(x) = w.I_0.\mathrm{y(x)} \qquad \text{Eq. 5.25}$$

$$P_t(x) = w.I_0.(d - y(x)) \qquad \text{Eq. 5.26}$$

We will have

$$s(x)=\frac{P_t(x)-P_r(x)}{P_t(x)+P_r(x)}=\frac{w.I_0.(d-2y(x))}{w.I_0.d}=2K_1.x-1 \qquad \text{Eq. 5.27}$$

To compensate for the non-uniform source, a multi-patterned-encoder with the following equations should be designed, as shown in Figure 5.13.

$$y_{2i-1}(x)=(2i-1)\frac{d}{6}-\frac{d}{6}(1-K_1.x)(i=1,2,3). \qquad \text{Eq. 5.28}$$

$$y_{2i}(x)=(2i-1)\frac{d}{6}+\frac{d}{6}(1-K_1.x)(\mathrm{i}=1,2,3). \qquad \text{Eq. 5.29}$$

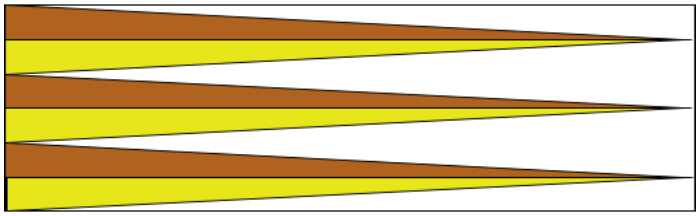

Figure 5.13 multi-patterned-encoder for linear displacement sensor, K_1=0.13, for the operating range of 15mm.

K_1 is determined based on the operating range. For a maximum operating range of R=15mm, $2K_1$ is selected as 0.13 to deliver the smallest width of 41µm (Eq. 4.23) which is more than 6.5µm to avoid diffraction.

$$w_i(x)=y_{2i}-y_{2i-1}=\frac{d}{6}(1-K_1.x)(\mathrm{i}=1,2,3).. \qquad \text{Eq. 5.30}$$

In this encoder sensor, again there is a trade-off between sensor sensitivity (proportional to K_1) and the operating range (Proportional to $1/K_1$). Sensitivity is calculated as:

$$Sensitivity=\frac{ds}{dx}=2K_1=130mW/W/\mathrm{mm} \qquad \text{Eq. 5.31}$$

CHAPTER 6 PROTOTYPE OF SMART OPTICAL ROTARY SENSOR

6.1 Introduction

In this Chapter, a first prototype smart optical rotary sensor is demonstrated for fly-by-wire applications to detect cockpit inceptors or flight control surface movement. A rotary encoder, optical setup, electronic circuits, and a microcontroller with built-in analog-to-digital converters, are packed into a single housing with dimensions of 80mm x 80mm x 50mm to propose a smart sensor. To simulate cockpit inceptors or flight control surface-displacement, an actuator is rotated by a computer controlled driver and the output voltages are sent to the computer using a universal serial bus. Signal processing is done in two steps: software filtering followed by optical powers extraction from the measured digitized voltages. Experimental results show that the sensor has the sensitivity of 17.5 $mWW^{-1}deg^{-1}$. and an accuracy of 0.5% over the full range of 180°. Moreover, we test the sensor's reliability by examining the sensor response while varying the input power of the light source and we demonstrate that the sensor is highly reliable, a vital requirement for avionic applications. The sensor not only meets the requirements for avionic applications but it is also smart which leads to less maintenance, less electromagnetic interference, and significant weight reduction.

Smart concept has affected various technologies including telephones [77], buildings [78], [79], health monitoring devices [80], [81], transportation [82], [83], and power systems [84], [85]. The smart concept also influences the future trend of flight control systems of Fly-by-wire (FBW) aircrafts where sensors are controlled and monitored by computers [2]. The definition of a smart sensor, based on references [4], [5], is a combination of a sensor, an analog circuit, an analog-to-digital converter (ADC), and a bus interface in a single housing; while a traditional sensor only provides raw signals [86].

Conventional flight-control systems apply hydraulic actuators and control valves controlled by cables that pass the length of the airframe, from the cockpit area to the surfaces to be controlled [2]. The disadvantage of this hydraulic cable-controlled system is the weight of long cables which

result in a large payload for the aircraft. FBW aircrafts use electronic displacement sensors in which the analog signals from the sensor are directly sent to the flight control computer (FCC) interface. Hence, the demodulation and digitizing processes of analog signals are done in the FCC interface which consumes many of connector pin and circuit board surface. A solution to this challenge is a smart sensor in which the corresponding electronics for demodulation and the digitizing processes for the analog signals is removed from the FCC interface and located with the sensor itself in a compact box as shown in Figure 6.1[3], [87]. In FBW system, there are ~30 displacement sensors in the cockpit each has usually 5 wires [3]. Replacing these wires with only 4 buses [3] results in less maintenance, less electromagnetic interference (EMI) as buses are less sensitive to EMI, lower weight and accordingly less fuel consumption, longer range, and hence lower operating cost.

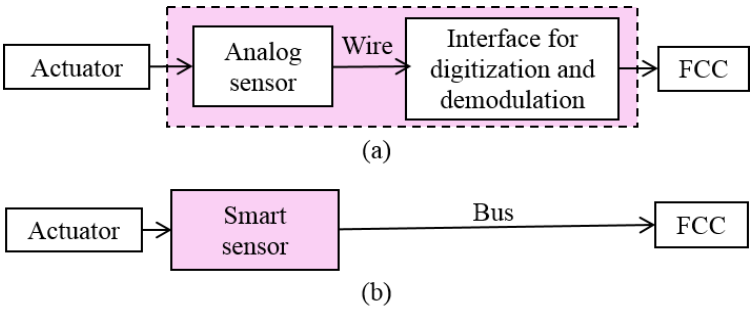

Figure 6.1 Replacing (a) traditional sensor with (b) smart sensor in FBW aircrafts. FCC: flight control computer.

In [67], we tested the previously implemented optical rotary encoder using a HeNe laser and two cylindrical lenses as the source and a photodetector for detection resulting in a large, non-packable layout. In this paper, we propose a smart optical rotation sensor as its first prototype. Diminishing the sensor size and weight, which are critical parameters in avionic applications, we use a small laser diode (LD) instead of a large HeNe laser. We benefit not only from its small size but also from its elliptical beam cross-section as it allows the use of only one spherical lens to make a collimated beam with an elliptical cross-section to illuminate the slot with a rectangular form, used in an earlier demonstration prototype [67]. Moreover, we use photodiodes (PDs) to produce an analog current signal from the amplitude modulated (AM) light power. Trans-impedance amplifier circuits are used to amplify the photo-currents and produce analog voltages.

These circuits include a low-pass filter to remove the high-frequency noise. The analog signals are digitized by ADCs which are built-in, in a 32-bit ARM Cortex-M4 microcontroller. The digitized

signals are sent to the computer by USB cable. To propose a smart sensor, we place the rotary encoder, optical setup, electronic circuits, and the micro-controller board in a single housing with the outer dimensions of 80mm x 80mm x 50mm. To test the sensor, we rotate the actuator by a computer-controlled driver to simulate the movement of flight control surfaces or inceptors in the cockpit - such as sidesticks, rudder pedals, spoiler handle, and flap handle - and collect digital voltages at the output of the sensor in the computer through a USB cable. The signal processing is performed in two steps: software filtering and extraction of the signal voltage from the optical power. The ratio of powers – transmission and reflection – determines the sensor response.

The remainder of this Chapter includes the following sections. In section 6.2, prototype development, three blocks of optical rotation sensor - mechanical, optical, and electrical - are proposed. In section 6.3, signal processing steps, including moving average (MA) filter and the power extraction (PE) process from electric voltages, are discussed. In section 6.4, prototype testing, test setup and sensor tests and discussions are presented.

6.2 Prototype development

6.2.1 Concept

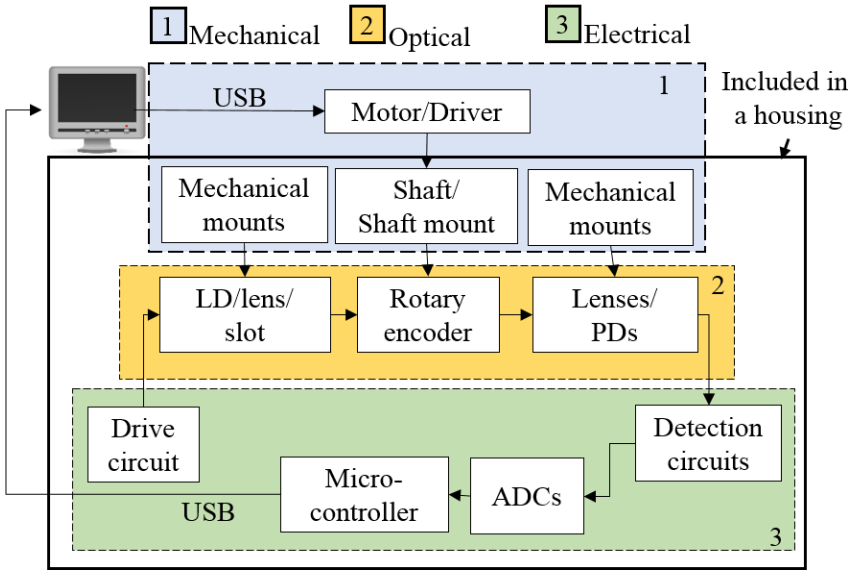

Figure 6.2 Block diagram of the rotary sensor system including mechanical, optical, and electrical blocks which are included in the ultimate housing of sensor. LD: Laser diode, PD: Photodiode, USB: Universal serial bus, ADC: Analog to digital converter.

The main concept of sensor prototype in the block diagram format, shown in Figure 6.2, is composed of three blocks: mechanical, optical, and electrical. The mechanical assembly includes an actuator, its driver, and mounts for optical and optoelectronic components, and a shaft. The optical setup includes the LD, lenses, PDs and rotary encoder. The electrical module incorporates a drive circuit for the LD, detection circuits for the PDs, ADCs, and micro-controller blocks. Note that the actuator follows the commands from the computer-controlled driver and the data read by the microcontroller is collected by the computer. All blocks except the actuator and the driver are included in a single housing as the first prototype of proposed sensor is shown in Figure 6.2. The three blocks - mechanical, optical, and electrical - are explained in the following sections.

6.2.2 Mechanical assembly

Figure 6.3 shows the parts of the mechanical assembly of the rotary sensor including its housing.

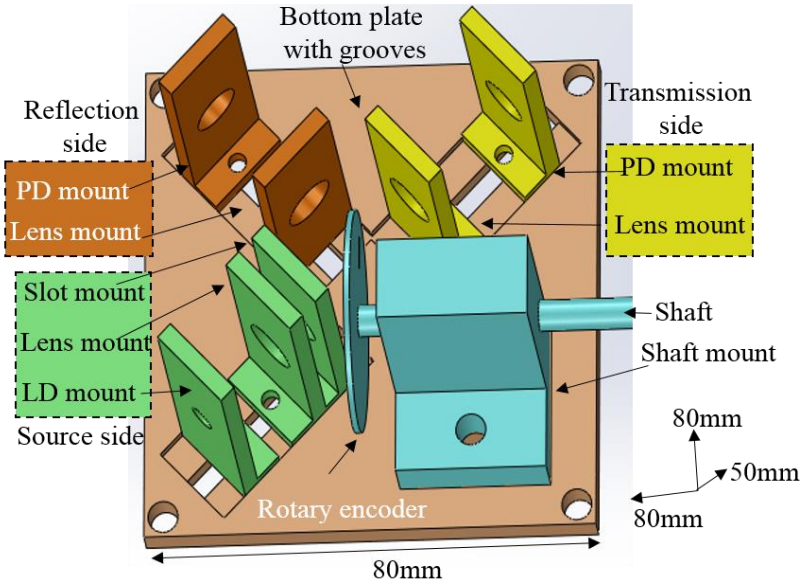

Figure 6.3 Mechanical assembly: mounts for LD, PDs, lenses in the reflection and transmission sides, and shaft mount. The sizes of final housing are 80mm x 80mm x 50mm. LD: Laser diode, PD: Photodiode.

The source and mounts for the LD, lens, and slot are considered. As the distance between the LD and lens must be adjusted, they have separate mounts. However, the distance of lens and slot can be fixed and thus their mounts come together. For detection, reflection and transmission, mounts for PDs and lenses are shown which are in the separate mounts to adjust their positions. Moreover,

it includes the shaft mount to prevent it from bending to decrease mechanical errors. Note that because of the alignment grooves on the bottom plate of the housing and identical height mounts for the optical components, each mount needs to be adjusted only in one direction. In addition, grooves assist in adjusting the input angle of the beam to 45 degrees towards the rotary encoder. After adjustment, they are fixed using bolts. Also, aluminum plates were used to fabricate the ceiling and two L-shaped walls of the housing to protect the sensor from dust. One of the walls has a hole to insert the shaft. All mechanical parts are sprayed with the black paint to absorb unwanted light powers. Specifications of the mechanical assembly are summarized in Table 6.1.

Table 6.1 Specifications of the mechanical assembly

Parameter	Type/Value
Bottom surface area	80mm x 80mm
Height	50mm
Material	Aluminum covered with black paint
Shaft diameter	4.75mm

6.2.3 Optical setup

In the optical setup Figure 6.4, the optical setup of the source and detection and the rotary encoder design are briefly explained.

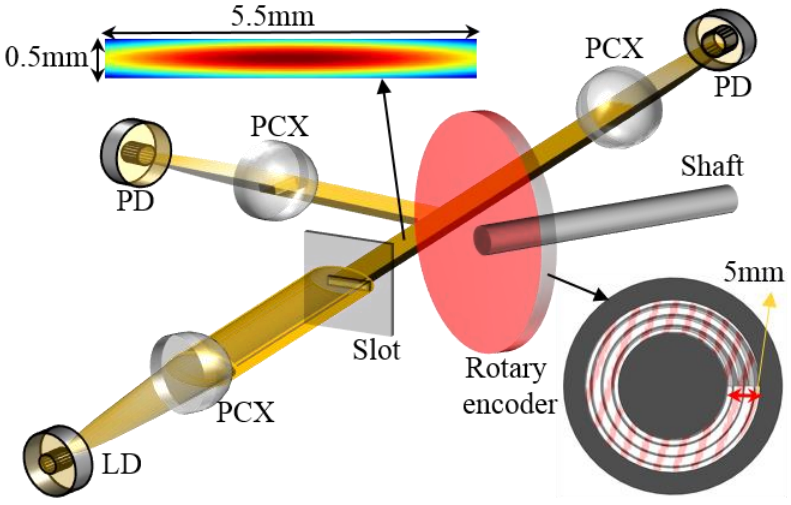

Figure 6.4 Optical setup, beam cross section on the rotary encoder is shown on the top.

An LD at 650 nm is used instead of a bigger HeNe laser to reduce the size of the sensor. Additionally, we benefit from the elliptical beam cross-section of LD to illuminate the rectangular slot used with the encoder by using just one Plano-convex (PCX) lens with the focal length of 12mm to collimate the light. The lens and the LD are placed on the mounts and then fixed with the help of small amount of epoxy glue. The rectangular slot is installed parallel to the lens. For detection, transmission and reflection, two PCX lenses with the focal length of 12mm are used to focus the light into the PDs. We selected silicon PDs because of their high performance in the visible spectral region. The overall length of this optical setup is around 80mm in the longest much smaller than our earlier works [67].

At the heart of the sensor, a glass rotary encoder (shown on the bottom right of Figure 6.4) with the outer diameter of 27mm is designed as discussed in Chapter 4 to deliver the transmission and reflection powers as per Eq. 6.1 and Eq. 6.2, respectively.

$$P_{\mathrm{t}}^{\mathrm{i}}(\theta) = \frac{P_0.\theta}{1+\theta} \qquad \text{Eq. 6.1}$$

$$P_{\mathrm{r}}^{\mathrm{i}}(\theta) = \frac{P_0}{1+\theta} \qquad \text{Eq. 6.2}$$

where P_0 is the total power in the patterned area of the encoder and θ is the rotation angle. In the calculation of Eq. 6.1 and Eq. 6.2, we assume that the beam cross-section width (shown on the top of Figure 6.4) is very small and beam cross section length is the same as the 5mm width of the patterned ring. The sensor response, $s^{\mathrm{i}}(\theta)$, is calculated as the ratio of transmission and reflection powers as per Eq. 6.3.

$$s^{\mathrm{i}}(\theta) = \frac{P_{\mathrm{t}}^{\mathrm{i}}(\theta)}{P_{\mathrm{r}}^{\mathrm{i}}(\theta)} = \frac{P_0.\theta \,/\, 1+\theta}{P_0 \,/\, 1+\theta} = \theta \qquad \text{Eq. 6.3}$$

Eq. 6.3 shows a linear relation between the sensor response and the angle of rotation and demonstrates that the requirement of the sensor, a single-valued linear function without hysteresis between measurand (rotation angle) and the response of sensor [63], has been met. Another important issue could be easily understood from Eq. 6.3 that it is independent of P_0, making it an

excellent sensor for avionic applications where high reliability is needed. Specifications of the optical setup are summarized in Table 6.2.

Table 6.2 Optical setup specifications

	Parameter	Size/type
Rotary encoder	Outer diameter	27mm
	Width of patterned ring	5mm
	Substrate thickness	1mm
	Substrate material	Soda lime
	Reflective material	Aluminum
Beam cross section	Length	5.5 mm
	Width	0.5mm
PCX Lenses	Focal length	12mm
	Outer diameter	9mm
	Type	Spherical plano-convex

6.2.4 Electrical module

In the electrical module, a driver circuit for the LD, detection circuits for the PDs in the transmission and reflection sides, and ADCs requirements are discussed in the following sections.

Driving LD with the typical output power of 5mW at the typical input current of 40mA, we made fixed a voltage source of 1.25V by means of a regulator and then used a resistance to yield the required input current of 40mA. To manage the space in the housing, this circuit is installed on the wall between source and reflection directions.

Detection circuits are required for the reflected and transmitted light. The generated photocurrent, I, in the PD is proportional to the optical power, P, and as per Eq. 6.4, [4], [88] is:

$$I = \Re.P \qquad \text{Eq. 6.4}$$

where $\Re$ is the responsivity of PD in the operating wavelength. A trans-impedance amplifier circuit with the gain of R_L is used to convert the PD current to the output voltage as per Eq. 6.5:

$$V = I.R_L = \Re.P.R_L \qquad \text{Eq. 6.5}$$

The value of resistance is selected to be 14 kΩ to not exceed the acceptable voltage, 3.3V, as an input for ADC. In parallel to the resistor, a capacitor of 1μF is used to filter the frequencies higher than 10Hz.

Two ADCs are needed to convert the analog voltages in the transmission and reflection directions to digital. They are selected based on the required resolution and sampling frequency. Resolution of the ADC is at least 14 bits, based on [3]. The sampling rate of the ADC more than 2x of the sensor bandwidth, to satisfy the Nyquist criterion. Having a very low bandwidth of less than 1Hz, the sampling rate of 1 kHz would keep the signal resolution for analog to digital conversion. The analog signals are digitized by built-in ADCs and read by Arduino software connected to the microcontroller Board.

A 32 bit ARM Cortex-M4 microcontroller on a Teensy 3.2 board with built-in ADCs is used. Two built-in ADCs have the maximum clock frequency of 12 MHz (maximum sampling frequency of 467 kHz) at a resolution of 16 bit. The small size of the Teensy board (35mm x 18mm) enables us to be placed it between two detection circuits on the PCB shown in Figure 6.5.Two analog outputs on the top of the PCB are installed to track the source of error before digitization. To manage the space in the housing, this PCB is installed on the wall between transmission and reflection directions.

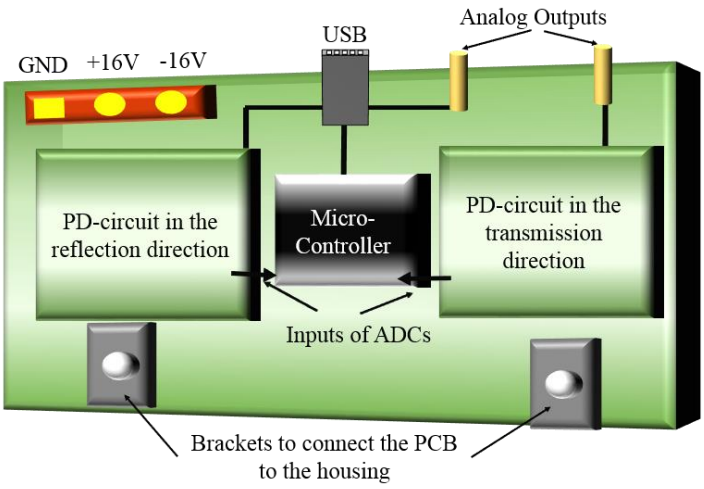

Figure 6.5 Electrical module: PCB design in which photodiode circuits and microcontroller board are integrated (with the size of 65mm x 40mm).

Specifications of the electrical module are summarized in Table 6.3.

Table 6.3 Electrical module specifications.

LD	Parameter	Size/Type
	Wavelength	650 nm
	Operating current	40mA
	Optical output power	5mW continuous wave
PD	Wavelength	400-1100 nm
	Package type	5.6mm
	Material	Silicon
	Responsivity at 650nm	$\Re$ =0.45

6.3 Signal processing

Signal processing is performed in two steps as shown in Figure 6.6 (a): MA filter and PE process. In MA filter, shown in Figure 6.6 (b), a number of points, *M*, from the input signal is averaged to produce each point in the output signal [89].

In equation form, this is written as follows:

$$\begin{cases} \overline{V}_{\mathrm{t}}^{\mathrm{EXP}}(\mathrm{i}) = \dfrac{1}{M}\sum_{j=i}^{i+M-1} V_t^{\mathrm{EXP}}(j) \\ \overline{V}_{\mathrm{r}}^{EXP}(\mathrm{i}) = \dfrac{1}{M}\sum_{j=0}^{i+M-1} V_r^{\mathrm{EXP}}(j) \end{cases} \qquad \text{Eq. 6.6}$$

where $V_{\mathrm{t}}^{\mathrm{EXP}}(V_{\mathrm{r}}^{\mathrm{EXP}})$ and $\overline{V}_{\mathrm{t}}^{\mathrm{EXP}}(\overline{V}_{\mathrm{r}}^{\mathrm{EXP}})$ are the voltages in the transmission (reflection) direction, before and after filtering, respectively. To determine *M*, the length of sampling window, one should find the optimum number of averaged samples. The block diagram of PE is shown in Figure 6.6 (c). The measured voltages after MA filter in the transmission and reflection directions are presented in Eq. 6.7 and Eq. 6.8, respectively:

$$\overline{V}_{\mathrm{t}}^{\mathrm{EXP}} = P_0(\tau_1 \Re_1 R_{\mathrm{L1}})\left\{\frac{\theta}{1+\theta} + \alpha_1\right\} \qquad \text{Eq. 6.7}$$

$$\overline{V}_{\mathrm{r}}^{\mathrm{EXP}} = P_0(\rho_{\mathrm{Al}}\tau_2\Re_2 R_{\mathrm{L2}})\left\{\frac{1}{1+\theta}+\alpha_2\right\} \qquad \text{Eq. 6.8}$$

All parameters (apart from α_1 and α_2) in Eq. 6.7 and Eq. 6.8 are specified in Table 6.4.

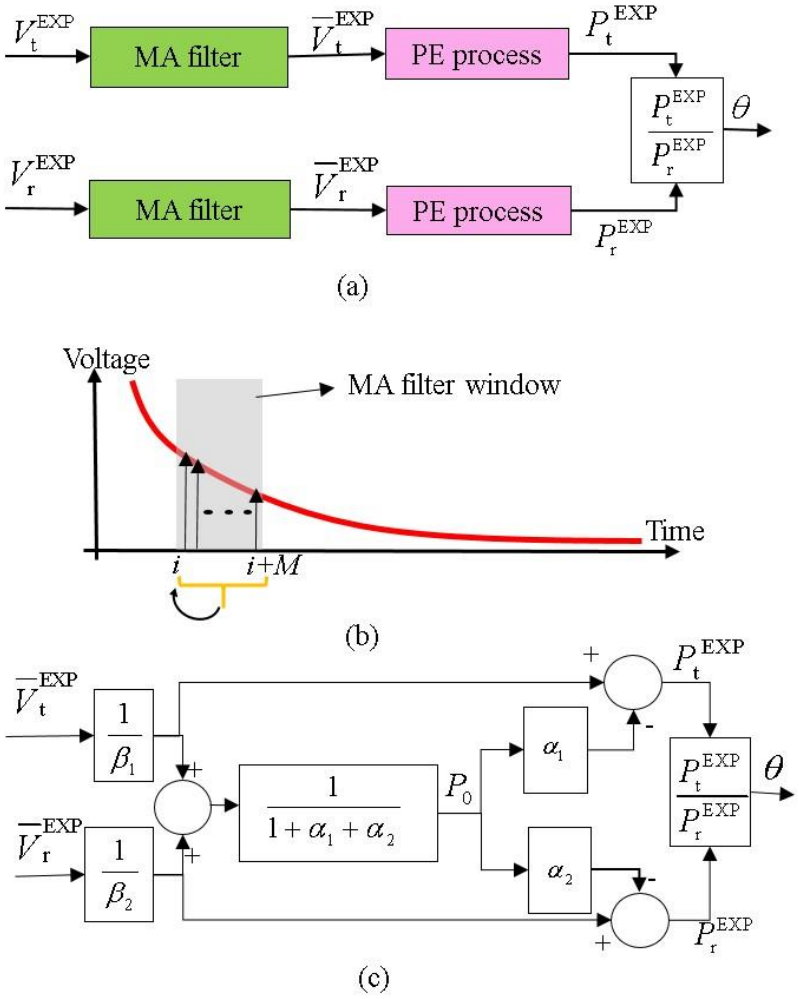

Figure 6.6 (a) Signal processing procedure, (b) Moving average (MA) filter, and (c) Power extraction (PE) in the reflection and transmission directions from the measured voltages.

Two parameters α_1 and α_2 come from the non-ideal width and length of the beam cross section, respectively, and obtained from Eq. 6.9 and Eq. 6.10.

$$\alpha_1 = P_1 / P_0 \qquad \text{Eq. 6.9}$$

$$\alpha_2 = P_2 / P_0 \qquad \text{Eq. 6.10}$$

Three powers of P_0, P_1 and P_2 are specified using Figure 6.7.

Beam cross section and the patterned area of the rotary encoder are shown in Figure 6.7 (a) and (b), respectively. Figure 6.7 (c) depicts powers P_0, P_1, and P_2 which have the following definitions:

P_0: The total power on the patterned area of the ring with the width of 5mm.

P_1: A constant power added to the transmission power because the width of beam cross section is not zero.

P_2: A constant power added to the refection power because the length of beam cross section (~5.5mm) is larger than the width of the patterned area (5mm).

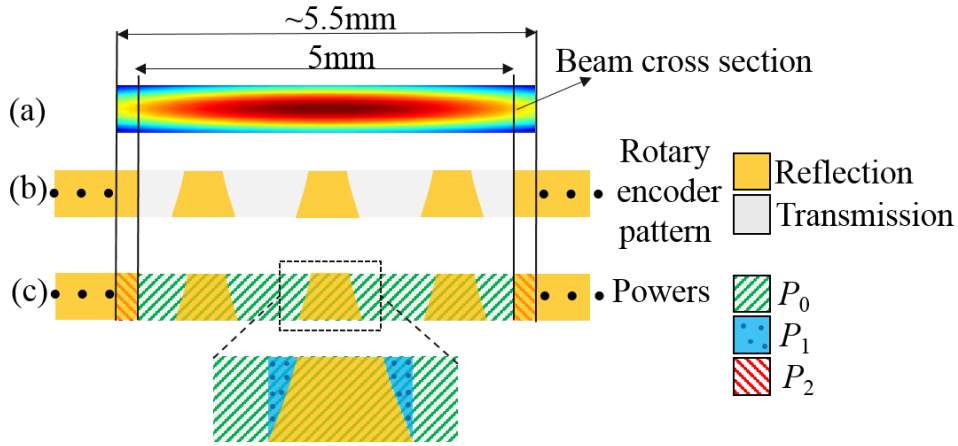

Figure 6.7 (a) Beam cross section on the rotary encoder, (b) The patterned area on the rotary encoder in which reflective and transmissive areas are shown in orange and gray, respectively, and (c) P_0, P_1 and P_2 calculations.

Assuming $\beta_1 = \tau_1 \Re_1 R_{L1}$ and $\beta_2 = \rho_{Al} \tau_2 \Re_2 R_{L2}$, we have:

$$\overline{V}_t^{EXP} = P_0.\beta_1 \left\{ \frac{\theta}{1+\theta} + \alpha_1 \right\} \qquad \text{Eq. 6.11}$$

$$\overline{V}_r^{EXP} = P_0.\beta_2 \left\{ \frac{1}{1+\theta} + \alpha_2 \right\} \qquad \text{Eq. 6.12}$$

Note that the parameters α_1, α_2, β_1, and β_2 are constants.

Table 6.4 Constant parameters in the reflection and transmission directions.

	Parameter	Definition
Transmission	τ_1	Transmittance of anti-reflection coated glass, the lens, and PD
	$\Re_1$	PD responsivity
	R_{L1}	Trans-impedance gain
	β_1	$\tau_1 \Re_1 R_{L1}$
Reflection	τ_2	Transmittance of the lens and PD
	ρ_{Al}	Aluminum reflection
	$\Re_2$	PD responsivity
	R_{L2}	Trans-impedance gain
	β_2	$\rho_{Al} \tau_2 \Re_2 R_{L2}$

According to Figure 6.6 (c), the total power on the patterned area of the rotary encoder, P_0, is obtained from the two measured voltages in the transmission and reflection directions as follows:

$$P_0 = \frac{1}{1+\alpha_1+\alpha_2}\left\{\frac{\overline{V}_t^{EXP}}{\beta_1}+\frac{\overline{V}_r^{EXP}}{\beta_2}\right\} \qquad \text{Eq. 6.13}$$

Next, the transmitted and reflected powers are extracted as Eq. 6.14 and Eq. 6.15.

$$P_t^{EXP} = \overline{V}_t^{EXP} \big/ \beta_1 - \alpha_1 . P_0 \qquad \text{Eq. 6.14}$$

$$P_r^{EXP} = \overline{V}_r^{EXP} \big/ \beta_2 - \alpha_2 . P_0 \qquad \text{Eq. 6.15}$$

In the PE process, the total power in the ring's width, P_0, is obtained from two measured transmitted and reflected signals. The transmission and reflection powers are extracted from the correction of the measured voltages. This process shows that if the source power fluctuates, P_0 and accordingly P_t and P_r are updated. The sensor response is calculated as:

$$s^{EXP} = \frac{P_t^{EXP}}{P_r^{EXP}} \qquad \text{Eq. 6.16}$$

6.4 Prototype testing

To test the sensor, we use an actuator to simulate the airplane inceptor in the cockpit. We use a computer-controlled driver connected to its related software to operate the actuator. It is rotated with the constant velocity of 6°-s^{-1} for a jog step size of more than 180° and begun at an angle below 0° to be sure that the actuator has no acceleration in the range of 0° to 180°.

6.4.1 Test setup

The test setup overview is shown in Figure 6.8 (a). LD (5mW) is driven with the drive circuit and produce a diverging beam with an elliptical cross-section. Hence, one spherical lens is used to yield a collimated beam with an elliptical cross-section to illuminate rectangular slot. After the slot, the light with rectangular cross section arrives at the rotary encoder where a portion of the light is transmitted and the rest is reflected, as per Eq. 6.1 and Eq. 6.2, respectively. The transmitted and reflected light are directed by two lenses and focused into PDs which are connected to trans-impedance amplifier circuits to convert the light to a voltage less than 3.3V, ADC limit. The generated voltages are digitized by the ADCs and sent to the computer via USB cables. The digitized voltages are read by Arduino software. The first prototype of the sensor is shown in Figure 6.8 (b). Specifications of actuator and driver are listed in Table 6.5.

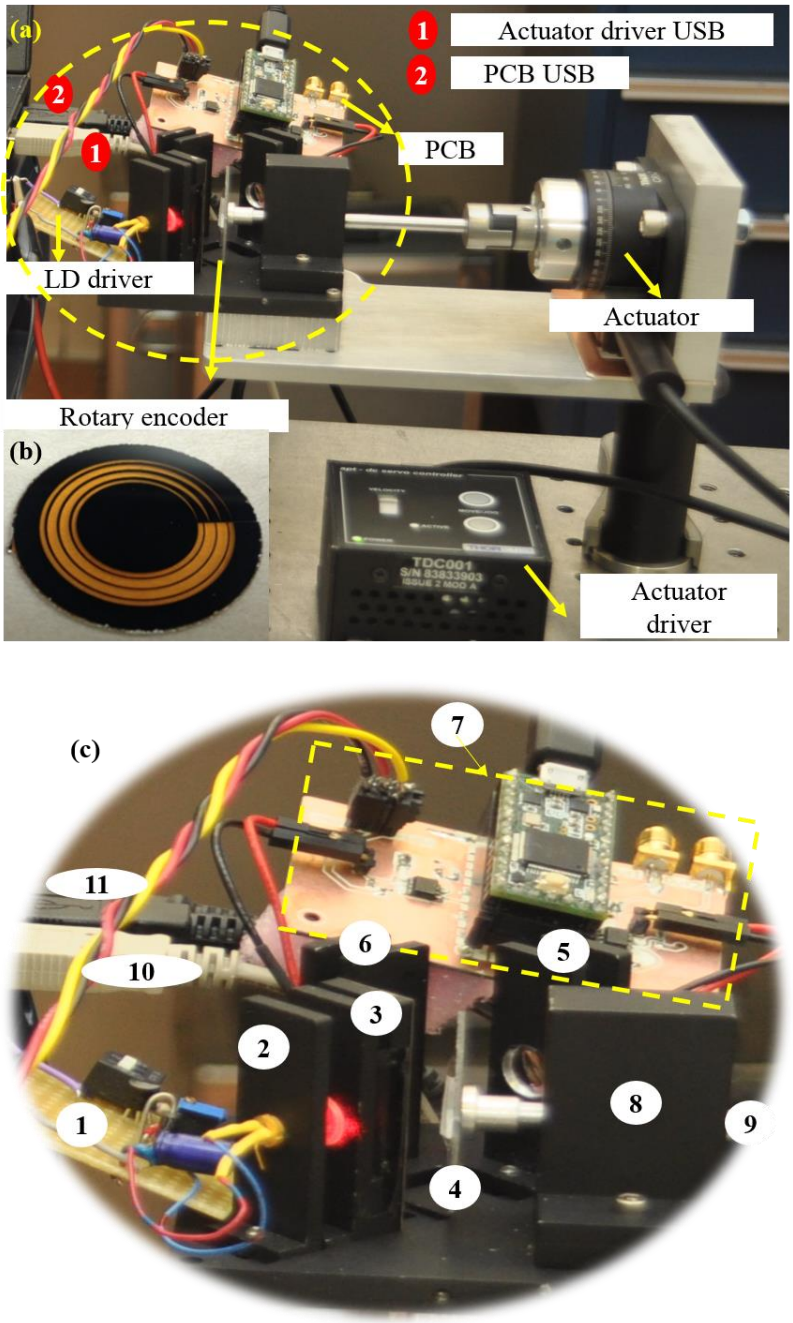

Figure 6.8 (a) Test setup overview, (b) fabricated rotary encoder, and (c) Zoom of sensor prototype including all mechanical, optical, and electrical module: 1- LD driver, 2- LD, 3- PCX (Source side) and slot, 4-Rotary encoder, 5- PCX and PD (Transmission side) 6- PCX and PD (Reflection side), 7- Detection circuits and microcontroller integrated in one PCB, 8- Shaft bearing, 9-Shaft, 10- Actuator driver USB, 11- PCB USB

Table 6.5 Actuator and driver specifications.

	Parameter	Type/Value
Actuator /drive	Driver	TDC001 Dc servo drive*, controlled through Thorlabs apt software
	Actuator stage	CR1-Z7*
	Velocity	6 deg./sec.
	Acceleration	0 (from 0º to 180º)
	Jog step size	More than 180°
	*Note: bought from Thorlabs	

6.4.2 Sensor tests

Sensor response is calculated as the ratio of transmitted and reflected powers. Hence, the MA filter is used to filter high-frequency noise of the measured voltages. Next, the powers are extracted from a filtered voltage as explained in Section 6.3, signal processing.

The measured transmitted and reflected signal voltages ($V_{\mathrm{t}}^{\mathrm{EXP}}$ and $V_{\mathrm{r}}^{\mathrm{EXP}}$) are plotted vs. time in Figure 6.9 (a) normalized to 2^{16} -1, where the number of digitization bits is 16.

The two voltages are zoomed from 4.8 to 5 sec. showing the high-frequency noise Figure 6.9 (b) and (c). Using MA filter to filter this noise, an optimum length for the averaging window is selected through a trial and error process. Filtered voltages ($\overline{V}_{\mathrm{t}}^{\mathrm{EXP}}$ and $\overline{V}_{\mathrm{r}}^{\mathrm{EXP}}$) for 40 and 10 points MA filter are shown in Figure 6.9(d)-(g). As the number of points increases, the noise becomes lower, however, the voltages get an offset resulting in an error in the sensor response calculation. Hence, the optimum length of the filter is selected to be 10, which allows meeting the targeted error.

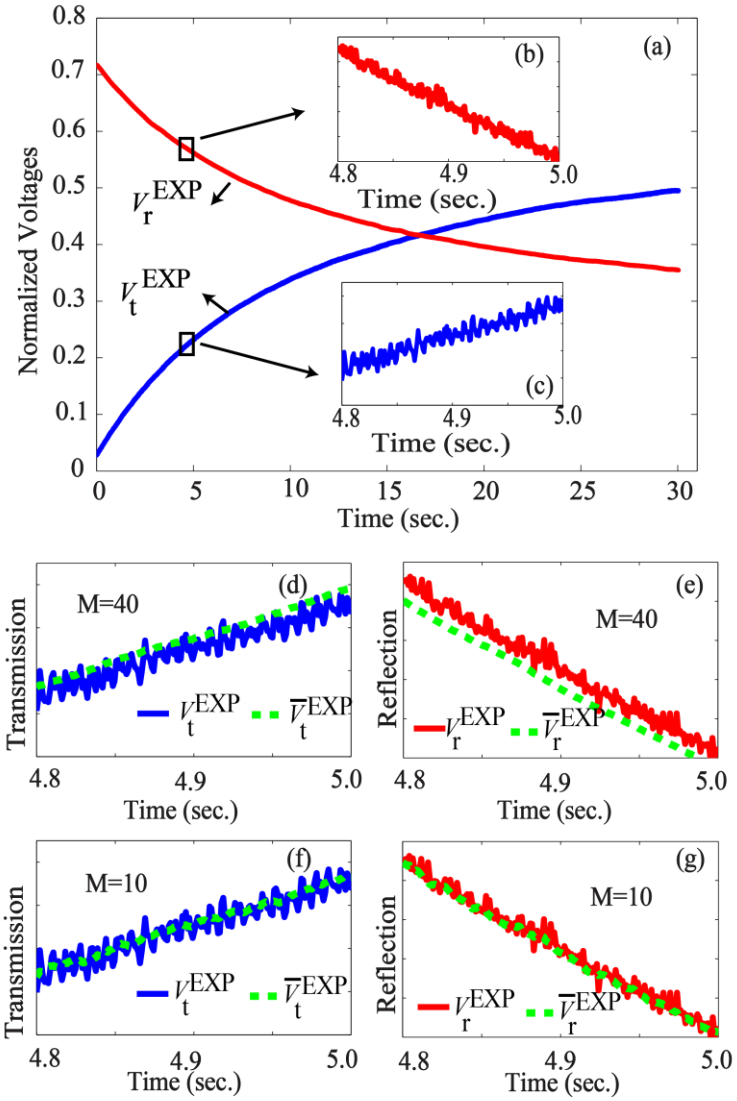

Figure 6.9 (a) Measured voltages in transmission and reflection directions vs. time (b)-(c) zoomed from 4.8 sec. to 5 sec. and (d)-(g) the voltage signals before and after MA filter for a different length of MA filter window.

The extracted powers (P_t^{EXP} and P_r^{EXP}) are shown in Figure 6.10 (a). To draw the response vs. rotation angle (x-axis on the top of the figure with a full range of 0-180º), the velocity of the actuator, 6°-s-1. We use the curves of Figure 6.10 (a) in an experiment to calculate the sensor response, the ratio of two powers, as shown in Figure 6.10 (b). This shows a linear relation between the sensor response and the rotation angle which demonstrates that our sensor has the requirement of linearity between measurand (rotation angle) and measured (ratio of voltages in transmission and reflection directions) [63].

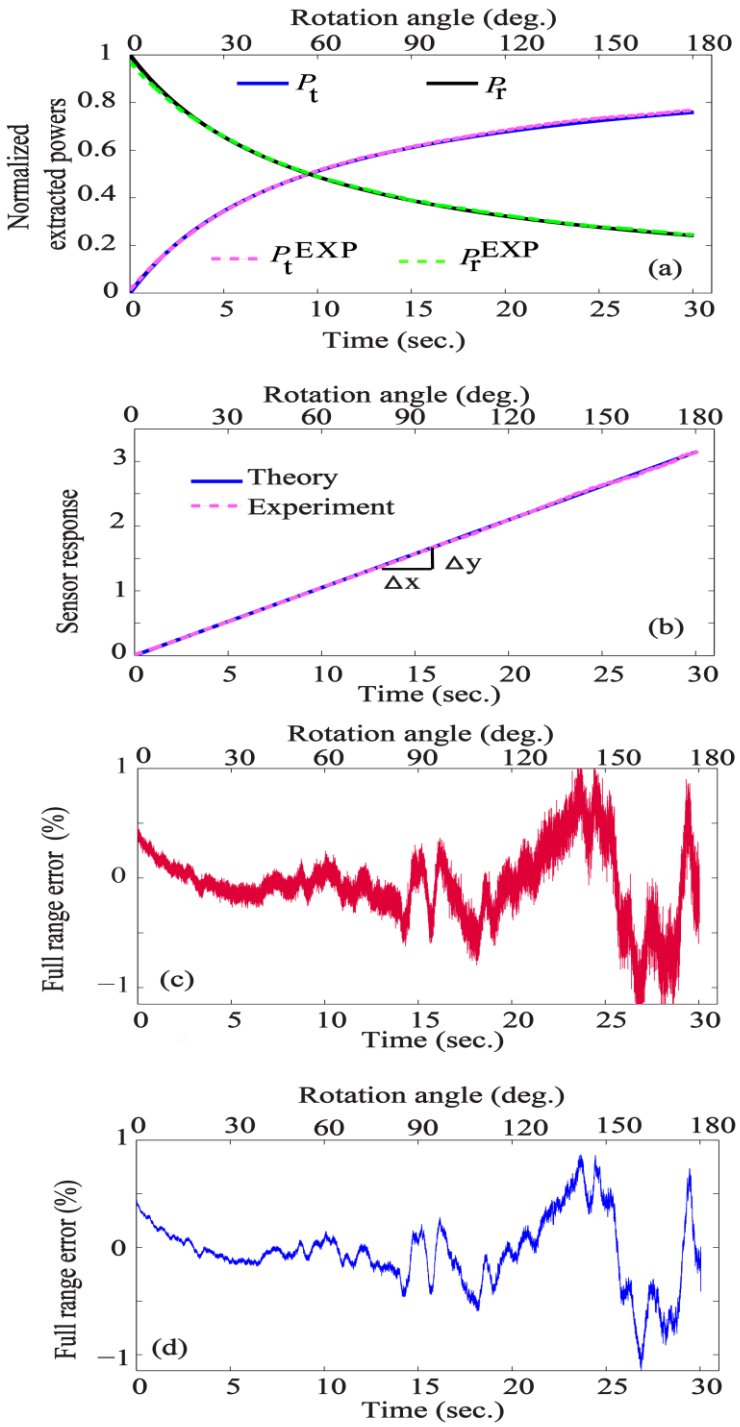

Figure 6.10 (a) normalized transmission and reflection powers in theory and experiment, (b) sensor response, ratio of transmission and reflection powers in theory and experiment, (c) full range error in percentage without MA filter, and (d) full range error in percentage with MA filter. Note: The sensor response is equal to θ, hence is scaled to π.

To determine the sensitivity of the sensor, the slope of sensor response curve, the ratio of two measured reflected and transmitted signal voltages vs. rotation angle, as drawn in Figure 6.10 (b) are calculated. The sensitivity is determined as per Eq. 6.17:

$$Sensitivity = \Delta y / \Delta x \qquad \text{Eq. 6.17}$$

where Δy and Δx are small changes of measured and measurand, respectively. It shows the sensitivity of 17.5mWW^{-1}-deg^{-1}. Comparing with the Rotary Variable Differential Transformers (RVDTs) from Mouser Electronics with the sensitivity of less than 3mV-V^{-1} deg^{-1}, our sensor is several times more sensitive.

Testing the accuracy of the sensor, we need to calculate the error. The percentage of full range error is calculated as:

$$Error = (\theta^{EXP} - \theta^{i}).\frac{180}{\pi}.\frac{100}{Range} \qquad \text{Eq. 6.18}$$

where θ^{EXP} and θ^{i} are rotation angles in the experiment, and under ideal condition, as per Eq. 6.19 and Eq. 6.20, respectively.

$$\theta^{EXP} = s^{EXP}(\theta) \qquad \text{Eq. 6.19}$$

$$\theta^{i} = s^{i}(\theta) \qquad \text{Eq. 6.20}$$

where $s^{EXP}(\theta)$ and $s^{i}(\theta)$ are the sensor responses in the experiment and under ideal condition, respectively. Hence, the full range % error is:

$$Error = \frac{18000}{2.\pi.K.Range}\left[s^{EXP}(\theta) - s^{i}(\theta) \right] \qquad \text{Eq. 6.21}$$

The percentage of error over the full range of 180 vs. time and rotation angle is shown in Figure 6.10 (c) and (d), without and with the MA filter, respectively. The full range RMS error is 0.5%. Sources of error are from the optical beam cross section width, optical beam non-uniformity, and mechanical and experimental errors. They were excessively discussed in Chapter 4.

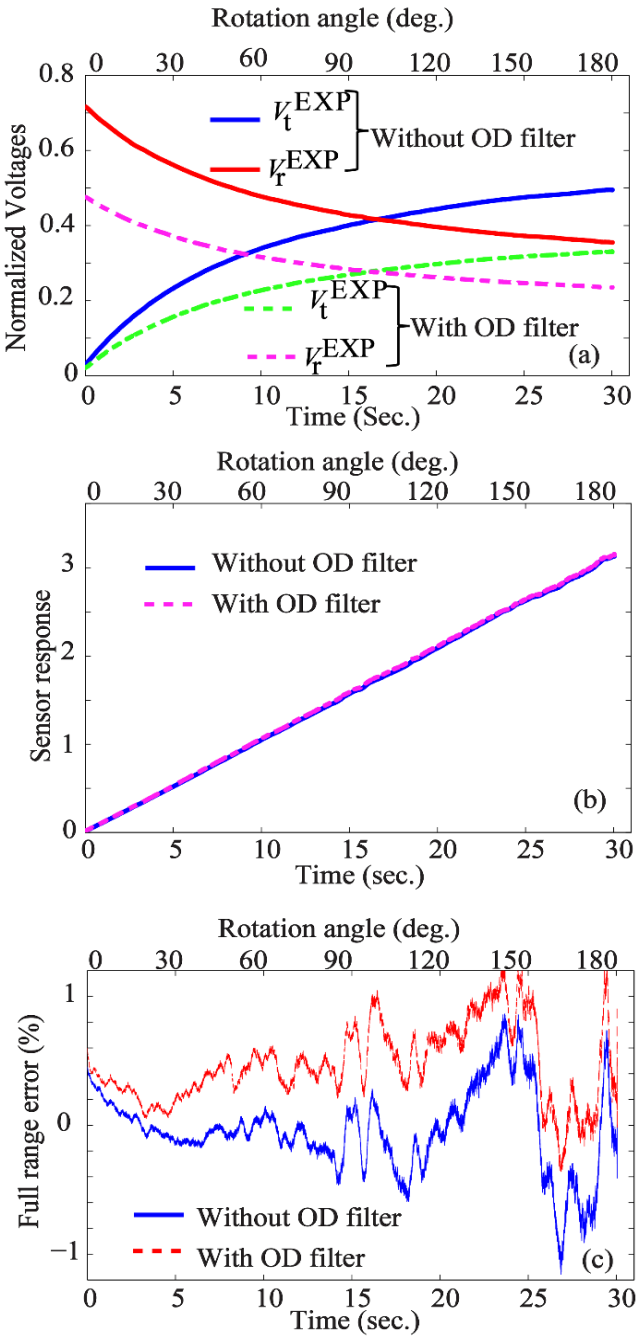

Figure 6.11 (a) Measured voltages in transmission and reflection directions vs. time and rotation angle, (b) sensor response, and (c) full range error for two cases of with and without optical density (OD) filter.

To test the reliability of sensor, we measure two voltages in the reflection and transmission directions for two cases, without and with neutral density filter with optical density (OD) of 0.3 which let 63% of LD power to be transmitted.

Figure 6.11 (a) shows the measured transmitted and reflected signal voltages vs. time and rotation angle, with and without the OD filter. With the decrease in the input power, transmitted and reflected powers are both reduced. Figure 6.11 (b) and (c) show the sensor response and full range error vs. time and rotation angle which confirm that with the reduction in the input power (such as aging), sensor response does not change. The error shown in Figure 6.11 (c) mostly comes from the fabrication error resulting in an error in the width of fabricated patterns. The shift between the errors in two cases come from mechanical errors.

The parameters of our sensor, optical sensors, and RVDTs are summarized in Table 6.6, in terms of EMI interference, resolution/accuracy, temperature range, operating range, operation speed, and size. Three sensors have the same approximate size and work within the required temperature range (-40°C to +55°C) for avionic applications. Optical sensors with high accuracy and speed are used for the applications where these requirements are vital, such as automotive manufacturing [10], robotics, and motion capture systems. However, such accuracy and speed are not compatible with the avionic requirements. RVDTs not only have a limited operating range of 80° but also are sensitive to EMI. Our sensor is compatible with the required accuracy and operating speed for avionic applications. The last not least, our sensor is proposed within the requirements of a smart sensor, in which analog sensor and the digitizing parts are packed into a single housing.

Table 6.6 Comparison of our sensor with optical sensors and RVDT.

Parameter/ sensor type	Optical encoder[21], [23]	RVDT [22]	This work
EMI	Not sensitive	Sensitive	Not sensitive
Resolution/ Accuracy	17 bits	1% over the full range	0.5% over the full range
Temperature range (°C)	-40 to 70	-55 to 70	-40 to 70
Operating range (deg.)	360°	-40° to +40°	0° to 180°
Operation speed*	High speed	Low speed	Low speed
Size (mm)	58-116	72	80
* High speed means more than 100kHz Note: Avionic requirements: Accuracy: 1% over the full range, temperature range: -40 °C to +55°C, and operation speed: low			

6.5 Summary

In this Chapter, we fabricated and tested the first prototype of our smart rotary sensor. Having smart sensor, mechanical, optical, and electrical blocks (including analog and digital parts) were packed in a single housing with the size of 80mm x 80mm x 50mm. To test the sensor, the actuator was rotated by a computer controlled driver to simulate the movement of cockpit inceptors (such as sidesticks, rudder pedals, spoiler handle, and flap handle) or flight control surfaces and the voltages on the detection side were sent to the computer via a USB. Signal processing was made by MA filtering and then power extraction from the measured voltages. Experimental results showed that the sensor sensitivity is 17.5 $mWW^{-1}deg^{-1}$ and sensor accuracy is 0.5% over the full range of 180^{o}, matching with the specifications for avionic applications. Moreover, we tested the sensor reliability with examining the sensor response when changing the input power of the light source and we demonstrated that the sensor is highly reliable, the indispensable requirement for avionic applications. Besides of being consistent with the requirements for avionic applications, our sensor is smart which leads to less maintenance, lower EMI, and potentially, lighter aircrafts. The related works were submitted/published in [87], [90]–[92].

CHAPTER 7 CONCLUSIONS AND FUTURE WORKS

7.1 Conclusions

The scope of this dissertation is in the design and fabrication of optical rotation sensors (ORSs) for FBW applications. In the design procedures, to achieve high reliable devices, ratiometric sensor responses were used in which the ratio of transmitted and reflected light powers or the ratio of the difference to the sum of reflected and transmitted powers specified the angle of rotation. Therefore, the effect of source fluctuation is canceled in the numerator and denominator of sensor response making the sensor independent of the source fluctuations. Another distinguishing aspect of our design is the multi-section pattern of the encoder and simulation results showed that the designs make the sensors robust and independent of a non-uniform source. The ORS encoders were fabricated on small AR coated glass substrates with the outer diameter of 27mm. Aluminum with the thickness of ~100nm was deposited on the glass and then etched according to a multi-patterned rings designs.

Experimental results showed that the sensor has the accuracy of 0.53% over the full operating range of 180º and sensitivity of 17.5 $mVV^{-1}deg^{-1}$, in the first design and the accuracy of 0.8% over the full operating range of 356.5º and sensitivity of 5.2 $mVV^{-1}deg^{-1}$., in the second design. Moreover, it was shown that these sensors are self-referenced and that variation of input power does not affect the sensor response.

Comparison of our two works in Chapter 4 and 5, showed that the former is more sensitive and the latter has a larger operating range. Compared to RVDTs which are currently used in the aviation industry, our sensors have the broader operating ranges and sensitivities for the same accuracy. Compared to optical rotation sensors in the market, our sensors have a simpler design, lower number of parts, and are designed for low-frequency applications. In addition, our optical sensor is more reliable as it works on a ratiometric principle.

Finally, the first prototype of our smart rotary sensor was fabricated and tested. Mechanical, optical, and electrical subsystems (including analog and digital parts) were packed in a single housing with the size of 8cm by 8cm by 5cm. To test the sensor, the actuator was rotated by a computer controlled driver to simulate the movement of cockpit inceptors (such as sidesticks, rudder pedals, spoiler handle, and flap handle) or flight control surfaces and the voltages in the detection side were sent

to the computer via a USB. Signal processing was done by moving average filtering and then power extraction from the measured voltages. Experimental results (for the first design as in Chapter 4) showed that the sensor sensitivity is 17.5 $mWW^{-1}deg^{-1}$ and sensor accuracy is 0.5% over the full range of 180°, matching with the specifications for avionic applications. Moreover, we tested the sensor reliability with examining the sensor response when changing the input power of the light source and we demonstrated that the sensor is highly reliable, the indispensable requirement for avionic applications. Besides of being consistent with the requirements for avionic applications, our sensor is smart which leads to less maintenance, less EMI, and lighter aircraft.

7.2 Future works - Fabrication improvements

General: Two future works were proposed in Section 4.7 and Section 5.5 related to two designs in Chapter 4 and Chapter 5, respectively. Following is another suggestion for the future work related to fabrication of rotary encoder.

Two improvements could be applied in the fabrication procedure of rotary encoder. Firstly, a layer of SiO2 (10nm) could be deposited on Al to protect it from oxidation and corrosion. In addition, a highly absorptive material could be deposited on the rotary encoder outside the patterned rings to absorb unwanted lights outside the patterned rings.

Metal protection: Most of the metals are protected by dielectric coatings to overcome limitations of chemical (silver) or mechanical stability (aluminum, silver, gold). Silver and aluminum could be coated by SiO2 dielectric films [93].

Highly absorptive layer: Outside the patterned-ring could be filled by an absorptive material to absorb the unwanted light power on the reflection side. Making a black absorptive layer, different solutions exist. Firstly, a black dye or carbon black is used to make a black absorbing layer. However, the resulting black layer has the thickness of a few hundred micrometers which is not appropriate for our application as it blocks the input light into the rotary encoder that results in an error to the transmitted power. Secondly, aluminum/gold could be anodized to make different colors including black color. However, the resulting layer has the thickness of some micrometers. Anodized aluminum in different colors is shown in Figure 7.1.

Figure 7.1 Anodized aluminum.

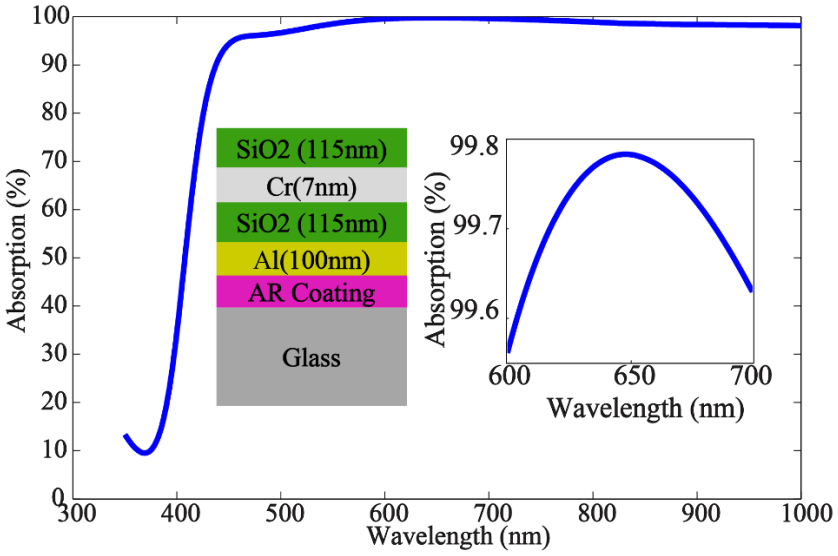

Figure 7.2 Absorption of metal-dielectric multilayer filter which is more than 99.7% at the operating wavelength. The thickness of absorptive layer causes 0.01% error over the full range.

Finally, the black metal-dielectric film could be used. With this solution, a black film with the thickness of 300nm would absorb more than 99.7% of input power [71]. In this structure, two absorbing layers of metal, aluminum, and chromium and two phase matching/compensation layers of SiO2 are used. The thickness of each layer is calculated as follows:

Al layer: It should be thick enough to be sure that the transmission is zero. Hence, 100nm of Al is thick enough to be able to suppose that no power passer aluminum.

Dielectric layers: The thickness of dielectric layers should be λ/4 to have the total distance of λ/2 in one round trip and hence having 180 degrees out of phase. For operating wavelength of 650nm and input angle of 45, the thickness of this layer will be λ/4×cos(45)=115nm.

Cr layer: As the absorption coefficient of Cr is $9\times10^{5}\times$ cm^{-1}, the skin depth of Cr will be 11nm. Having input angle of 45 degrees, it will decrease to 7.7nm. To have high absorption by Cr, its thickness should be less than 7.7nm. Hence, 7nm is selected for the thickness of Cr.

The absorption of a black film of SiO2/Cr/SiO2/Al on the anti-reflected glass vs. wavelength is shown in Figure 7.2. This simulation is done using the OpenFilter software. The final thickness of the film is 337nm brings the negligible error of 0.01% over the full range.

Final Design: The cross section of the final rotary encoder structure is shown in Figure 7.3.

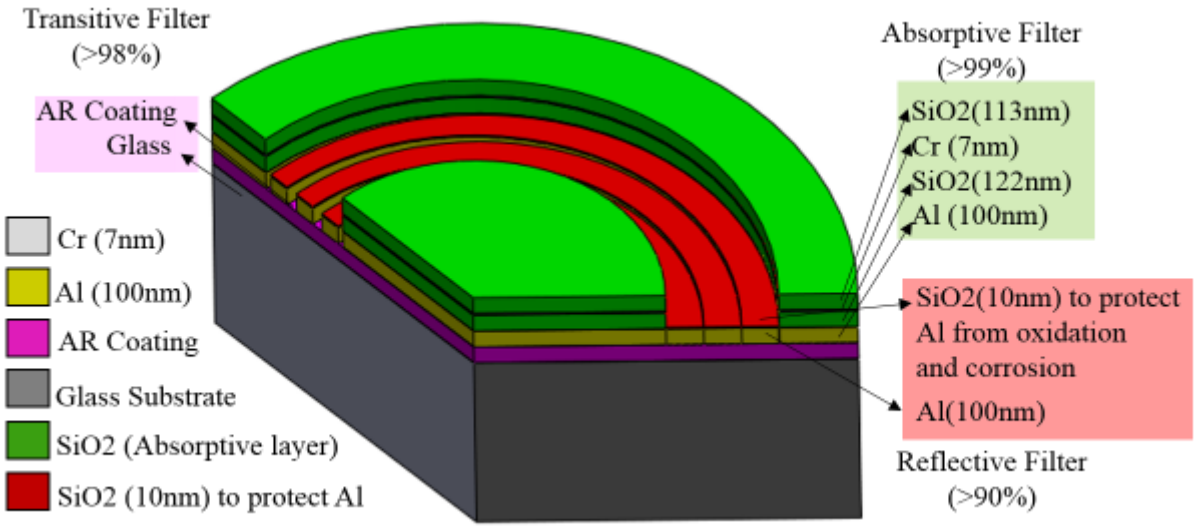

Figure 7.3 Rotary encoder fabrication structure with the details of absorptive, reflective, and transitive layers.

To fabricate the rotary encoder, three filters are required: absorptive, transitive, and reflective. Transitive and reflective filters are needed for transmission and reflection areas, respectively. Additionally, the absorptive filter is required to absorb unwanted light outside the patterned rings. Up view of the rotary encoder and three filters are shown in Figure 7.4. The trasnitive filter is composed of anti-reflection coating layers, SiO2 and Ti3O5, on the glass substrate which transmits light for more than 98%. For the reflective filter, aluminum is deposited on the AR-coated glass to reflect the light for more than 90% and covered by 10nm of SiO2 to protect it from oxidation

and corrosion. Finally, the absorptive filter is a black film composed of 4 layers of SiO2/Cr/SiO2/Al [71] on AR coated glass which absorbs more than 99% of the input light.

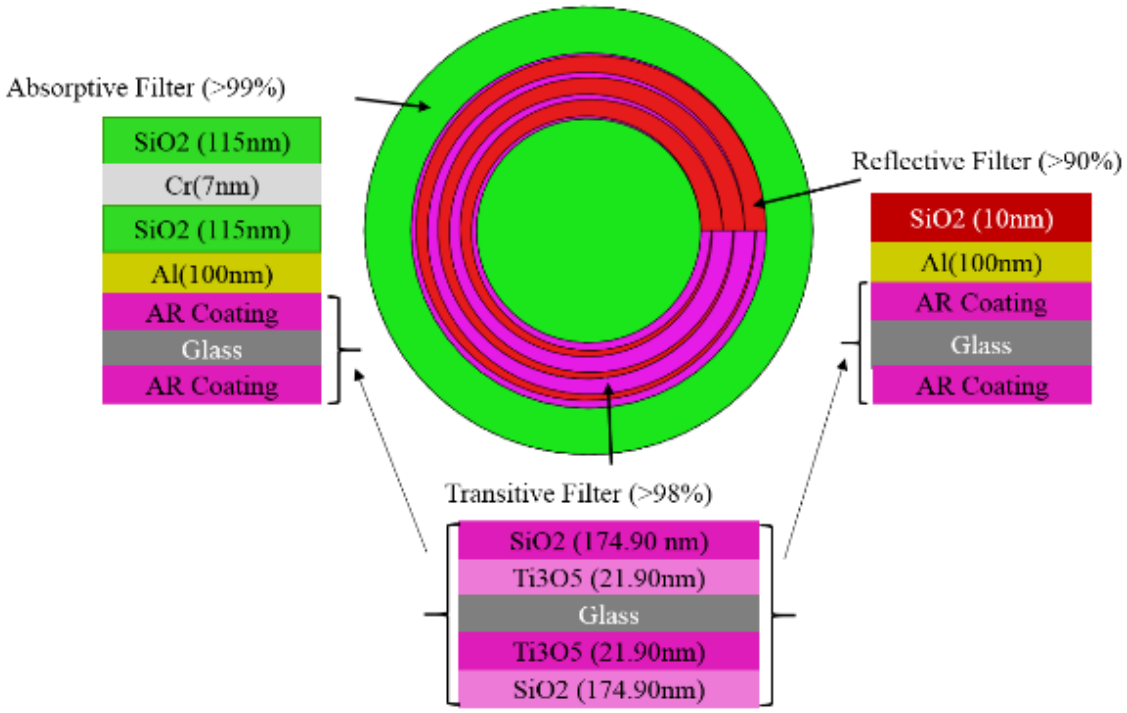

Figure 7.4 Top-view of the rotary encoder with absorptive, transitive, and reflective filters.

BIBLIOGRAPHY

[1] R. W. Pratt, *Flight control systems: practical issues in design and implementation*. 2000.

[2] C. R. Spitzer, *The Avionics Handbook*. CRC Press, 2001.

[3] F. Gansmandel, F. Clement, and P. Molaret, "CRIAQ Project AVIO402/NSERC CRD: Requirement of Smart Sensor prepared by Thales Group," 2010.

[4] G. C. M. Meijer, *Smart Sensor Systems*, 1st Ed. Delf: Wiley, 2008.

[5] A. Ukil, "Towards networked smart digital sensors: A review," in *Proceedings - 34th Annual Conference of the IEEE Industrial Electronics Society, IECON 2008*, 2008, pp. 1798–1802.

[6] Boeing Company, "Boeing History Chronology (1910-2010)," 2010.

[7] A. Garg, R. I. Linda, and T. Chowdhury, "Evolution of Aircraft Flight Control System and Fly-By-Light Flight Control System," *Int. J. Emerg. Technol. Adv. Eng.*, vol. 3, no. 12, pp. 60–64, 2013.

[8] R. G. P. Collinson, *Introduction to Avionics Systesm*, Third Ed., vol. 53, no. 9. London, 2011.

[9] D. McLean, *Automatic Flight Control System*. 1990.

[10] Y. Sugiyama, Y. Matsui, H. Toyoda, N. Mukozaka, A. Ihori, T. Abe, M. Takabe, and S. Mizuno, "A 3.2 kHz, 14-Bit Optical Absolute Rotary Encoder With a CMOS Profile Sensor," *IEEE Sens. J.*, vol. 8, no. 8, pp. 1430–1436, Aug. 2008.

[11] G. Orengo, A. Lagati, and G. Saggio, "Modeling Wearable Bend Sensor Behavior for Human Motion Capture," *IEEE Sens. J.*, vol. 14, no. 7, pp. 2307–2316, Jul. 2014.

[12] V. Liberali, F. Cherchi, L. Disingrini, M. Gottardi, S. Gregori, G. Torelli, and S. Member, "A Digital Self-Calibration Circuit for Absolute Optical Rotary Encoder Microsystems," *IEEE, Trans. Instrum. Meas.*, vol. 52, no. 1, pp. 149–157, 2003.

[13] K. Antonelli, R. O. Claus, D. Dayton, H. Eren, R. M. Hyatt, N. Karlsson, and A. Kholkine, "Chapter 6: Displacement Measurement , Linear and Angular," in *The Measurement, Instrumentation and Sensors Handbook on CD-ROM*, 1999.

[14] D. Hopp, C. Pruss, W. Osten, J. Seybold, K. Fritz, T. Botzelmann, V. Mayer, and H. Kück, "Diffractive incremental and absolute coding principle for optical rotary sensors," *Appl. Opt.*, vol. 50, no. 26, pp. 5169–5177, 2011.

[15] K. Tobita, T. Ohira, M. Kajitani, C. Kanamori, M. Shimojo, and a. Ming, "A Rotary Encoder Based on Magneto-Optical Storage," *IEEE/ASME Trans. Mechatronics*, vol. 10,

no. 1, pp. 87–97, Feb. 2005.

[16] S.-H. Jeong, S.-H. Rhyu, B.-I. Kwon, and B.-T. Kim, "Design of the Rotary Magnetic Position Sensor With the Sinusoidally Magnetized Permanent Magnet," *IEEE Trans. Magn.*, vol. 43, no. 4, pp. 1837–1840, Apr. 2007.

[17] T. Ahmadi Tameh, M. Sawan, and R. Kashyap, "Self-Referencing Ratio-Metric Optical Rotation Sensor for Avionic Application," in *Advanced Photonics, Bacelona, Spain*, 2014.

[18] J. S. Wilson, *Sensor Technology Handbook*. Elsevier, 2005.

[19] H. Zumbahlen, "Chapter 3: Sensors," in *Basic Linear Design: Analog devices*, 2007.

[20] J. Fraden, *Handbook of Modern Sensors: Physics, Designs, and Applications*, 4th ed. Springer, 2010.

[21] S. Wu, J. Chen, and S. Wu, "A Rotary Encoder With an Eccentrically Mounted Ring Magnet," *IEEE Trans. Instrum. Meas.*, vol. 63, no. 8, pp. 1907–1915, 2014.

[22] Z. Zhang, F. Ni, Y. Dong, C. Guo, M. Jin, and H. Liu, "A novel absolute magnetic rotary sensor," *IEEE Trans. Ind. Electron.*, vol. 46, pp. 1–11, 2014.

[23] Honeywell, "Hall Effect Sensing and Application," in *Sensing and Control*, 2011, p. 126.

[24] M. C. G. Inc., *Synchro and Resolver Engineering Handbook*. 2004.

[25] A. Ergun, G. Yaralioglu, O. Oralkan, and B. Khuri-Yakub, *MEMS/NEMS Handbook Techniques and Applications*, vol. 1–5. Los Angeles: Springer, 2006.

[26] D. M. Ma, J. K. Shiau, I. Chiang Wang, and Y. H. Lin, "Attitude determination using a MEMS-based flight information measurement unit," *Sensors*, vol. 12, no. 1, pp. 1–23, 2012.

[27] D. Piyabongkarn, R. Rajamani, and M. Greminger, "The development of a MEMS gyroscope for absolute angle measurement," *IEEE Trans. Control Syst. Technol.*, vol. 13, no. 2, pp. 185–195, 2005.

[28] W. A. Clark, "Micromachined z-axiz vibratory rate gyroscope," 5992233, 1999.

[29] T. K. Sethuramalingam and A. Vimalajuliet, "Design of MEMS based capacitive accelerometer," in *ICMET -International Conference on Mechanical and Electrical Technology, Proceedings*, 2010.

[30] M. N. Armenise, C. Ciminelli, F. Dell'Olio, and V. M. N. Passaro, *Advances in Gyroscope Technologies*. 2010.

[31] K. Taguchi, K. Fukushima, a. Ishitani, and M. Ikeda, "Optical inertial rotation sensor using semiconductor ring laser," *Electron. Lett.*, vol. 34, no. 18, p. 1775, 1998.

[32] C. Y. Chi and T. L. Cheny, “MEMS gyroscope control systems for direct angle measurements,” in *Proceedings of IEEE Sensors*, 2009.

[33] J. Lapointe, M. Gagné, A. Harhira, and R. Kashyap, “Optical fiber tissue elasticity sensor,” in *7th workshop on Fibre and Optical Passive Components (WFOPC)*, 2011.

[34] A. Shenhav, Z. Brodie, Y. Beiderman, J. Garcia, V. Mico, and Z. Zalevsky, “Optical sensor for remote estimation of alcohol concentration in blood stream,” *Opt. Commun.*, vol. 289, pp. 149–157, Feb. 2013.

[35] M. a Zawawi, S. O’Keeffe, and E. Lewis, “Plastic optical fibre sensor for spine bending monitoring,” *J. Phys. Conf. Ser.*, vol. 450, p. 12004, Jun. 2013.

[36] W. Shirbeeny and W. E. Mahmoud, “Synthesis and characterization of transparent optical gas sensor device made of indium oxide pyramid like nanoarchitectures,” *Sensors Actuators B Chem.*, vol. 191, pp. 102–107, Feb. 2014.

[37] Y. Tanaka, T. Nakamoto, and T. Moriizumi, “Study of highly sensitive smell sensing system using gas detector tube combined with optical sensor,” *Sensors Actuators B Chem.*, vol. 119, no. 1, pp. 84–88, Nov. 2006.

[38] M. Shao, X. Qiao, H. Fu, H. Li, J. Zhao, and Y. Li, “A Mach–Zehnder interferometric humidity sensor based on waist-enlarged tapers,” *Opt. Lasers Eng.*, vol. 52, pp. 86–90, Jan. 2014.

[39] M. Sierakowski, T. R. Woliński, and A. W. Domański, “Optical dust sensor for mining industry,” vol. 5064, pp. 122–127, 2003.

[40] J. Paulo, J. T. Gondek, G. Rafael, C. Possetti, M. Muller, J. Luís, and R. C. Kamikawachi, “Optical sensor based on etched fiber Bragg gratings for assessment of biodiesel quality,” pp. 458–460, 2011.

[41] M.-D. Baiad, S. M. Tripathi, A. Kumar, N. Galina, and R. Kashyap, “Integrated optical bio-sensor based on pure surface plasmon-polariton excited by a waveguide grating,” in *7th International Workshop on Fibre and Optical Passive Components*, 2011.

[42] M. N. Trutzel, K. Wauer, D. Betz, L. Staudigel, O. Krumpholz, H.-C. Muehlmann, T. Muellert, and W. Gleine, “Smart Sensing of Aviation Structures with Fiber-Optic Bragg Grating Sensors,” vol. 3986, pp. 134–143, Jun. 2000.

[43] M. S. Rao, M. V. Nageswara Rao, and R. Renuka, “An efficient classification of fiber optic sensors application to avionics,” *Proc. IEEE 1992 Natl. Aerosp. Electron. Conf. 1992*, pp.

1104–1109, 1992.

[44] M. Ciminello, A. Concilio, D. Flauto, and F. Mennella, “FBG sensor system for trailing edge chord-wise hinge rotation measurements,” in *Sensors and smart structures technologies for civil, mechanical, and aerospace systems*, 2013.

[45] Y. Matsuzoe, “High-performance absolute rotary encoder using multitrack and M-code,” *Opt. Eng.*, vol. 42, no. 1, p. 124, Jan. 2003.

[46] S. Nagao, F. Oohira, M. Hosogi, G. Hashiguchi, and A. Composition, “Rotary comb drive actuator with an optical fiber encoder,” in *IEEE conference*, 2006.

[47] K. Engelhardt and P. Seitz, “High-resolution optical position encoder with large mounting tolerances,” *Appl. Opt.*, vol. 36, no. 13, pp. 2912–2916, May 1997.

[48] T. Dziwi, “A Novel Approach of an Absolute Encoder Coding Pattern,” *IEEE Sens. J.*, vol. 15, no. 1, pp. 397–401, 2015.

[49] T. Kojima, Y. Kikuchi, S. Seki, and H. Wakiwaka, “Study on high accuracy optical encoder with 30 bits,” *8th IEEE Int. Work. Adv. Motion Control. 2004. AMC ’04.*, pp. 493–498, 2004.

[50] Company of Tamagawa, “Rotary encoders,” 2017. [Online]. Available: http://www.tamagawa-seiki.com/english/encoder/.

[51] Y. Tokunaga, I., and Shimojima, “Reflection type optical rotary encoder,” Patent no. 4650995, 1987.

[52] M. Tresanchez, T. Palleja, M. Teixido, and J. Palacin, “The optical mouse sensor as an incremental rotary encoder,” *Sensors Actuators A Phys.*, vol. 155, no. 1, pp. 73–81, Oct. 2009.

[53] M. Tresanchez, T. Pallejà, M. Teixidó, and J. Palacín, “Using the image acquisition capabilities of the optical mouse sensor to build an absolute rotary encoder,” *Sensors Actuators A Phys.*, vol. 157, no. 1, pp. 161–167, Jan. 2010.

[54] M. Taniguchi, M., and Aochi, “Optical Rotary Encoder,” Patenet no. 6255644, 2001.

[55] J. Chass, “Rotary Variable Differential Transformers,” Patent no. 5701114, 1977.

[56] Company of BEI Sensors, “Choosing the Right Sensor Technology,” 2017. [Online]. Available: http://www.beisensors.com/technical-support-bei-choosing-the-right-sensor-technology.html.

[57] Company of Honeywell, “Aerospace: Position Measurement,” 2017. [Online]. Available: http://sensing.honeywell.com/products/aero-rvdt?N=0.

[58] X. L. Yuan, Q. A. Huang, and X. P. Liao, “Analysis of electromagnetic interference of a capacitive RF MEMS switch during switching,” *Micro Syst. Technol.*, pp. 349–360, 2008.

[59] Company of STMicroelectronics, “Gyroscopes,” 2017. [Online]. Available: http://www.st.com/web/en/catalog/sense_power/FM89/SC1288.

[60] Company of National Instruments, “How to Choose the Right Sensor for Your Measurement System,” 2017. [Online]. Available: http://www.automation.com/pdf_articles/ni/how_to_choose_a_sensor.pdf.

[61] Baumer, “Productfinder Tachogenerators/Resolvers,” 2017. [Online]. Available: http://www.baumer.com/us-en/products/productfinder/?tx_baumerproductfinder_pf%5Burl%5D=%2Fpfinder_motion%2Fscripts%2Flevel2.php%3Flanguage%3Den%26header%3D%26cat%3DTachogeneratoren%26psg%3DPG_Tachogeneratoren%257CMC_Web_Resolver%26pid%3D%26ptk%3D%26viewmo.

[62] C. of I. Technology, “iPhone 4 Carries Bill of Materials of $187.51, According to iSuppli,” 2017. [Online]. Available: https://technology.ihs.com/388916/iphone-4-carries-bill-of-materials-of-18751-according-to-isuppli.

[63] R. Kashyap, *Fiber Bragg Gratings*. Academic Press, 1999.

[64] K. Kalantar-zadeh, *Sensors: An introductory course*. Springer, 2013.

[65] D. Jucius, I. Grybas, V. Grigaliūnas, M. Mikolajūnas, and a. Lazauskas, “UV imprint fabrication of polymeric scales for optical rotary encoders,” *Opt. Laser Technol.*, vol. 56, pp. 107–113, Mar. 2014.

[66] S. Larouche and L. Martinu, “OpenFilters: open-source software for the design, optimization, and synthesis of optical filters,” *Appl. Opt.*, vol. 47, no. 13, p. C219, Jan. 2008.

[67] T. Ahmadi Tameh, M. Sawan, and R. Kashyap, “Novel Analog Ratio-Metric Optical Rotary Encoder for Avionic Applications,” *IEEE Sens. J.*, 2016.

[68] S. O. Kasap, *Optoelectronics and photonics : principles and practices*, 2nd ed. New Jersey: PEARSON, 2013.

[69] J. Lee, Y. Ko, and S. Lee, “Calibration Technique for Sensitivity Variation in RVDT Type Accelerator Position Sensor,” in *2013 IEEE International Instrumentation and Measurement Technology Conference (I2MTC)*, 2013.

[70] C. of M. Specialties, “R36AS – AC Operated RVDT for Harsh Environments,” 2015.

[Online]. Available: http://www.mouser.com/ds/2/418/R36AS-710495.pdf.

[71] S. Cho, M. Seo, and J. Kang, “A black metal-dielectric thin film for high-contrast displays,” *J. Korean Phys. Soc.*, vol. 55, no. 2, pp. 501–507, 2009.

[72] M. Choi, G. Kang, D. Shin, N. Barange, C. Lee, D. Ko, and K. Kim, “Lithography-Free Broadband Ultrathin-Film Absorbers with Gap- Plasmon Resonance for Organic Photovoltaics,” *Am. Chem. Soc.*, vol. 8, pp. 12997–13008, 2016.

[73] J. Parker, “Sensor and Actuator Characteristics,” in *Mechatronic Systems, Sensors, and Actuators: Fundamentals and Modeling*, 2002.

[74] T. Mizuno, M. Doi, T. Shima, M. Fujimaki, and K. Awazu, “Optical-disk-based imaging system to be used as an optical microscope,” *Jpn. J. Appl. Phys.*, vol. 55, 2016.

[75] T. Ahmadi Tameh, R. Kashyap, and M. Sawan, “Self-referenced broad range optical rotation sensor for flight control application,” *Submitt. to IEEE Sensors J.*, 2017.

[76] T. Ahmadi Tameh, M. Sawan, and R. Kashyap, “Analog Optical Rotary Encoders : Operating Range-Sensitivity Trade-Off,” in *Submitted to Photonic North, Ottawa, Canada*, 2017.

[77] J. Lapointe, M. Gagné, M.-J. Li, and R. Kashyap, “Making smart phones smarter with photonics.,” *Opt. Express*, vol. 22, no. 13, pp. 15473–83, 2014.

[78] Q.-S. Jia, Q. Zhao, H. Darabi, G. Huang, B. Becerik-gerber, H. Sandberg, and K. H. Johansson, “Smart Building Technology,” *IEEE Robot. Autom. Mag.*, no. JUNE, pp. 18–20, 2014.

[79] M. Magno, T. Polonelli, L. Benini, and E. Popovici, “A Low Cost , Highly Scalable Wireless Sensor Network Solution to Achieve Smart LED Light Control for Green Buildings,” *IEEE Sens. J.*, vol. 15, no. 5, pp. 2963–2973, 2015.

[80] S. C. Mukhopadhyay, “Wearable Sensors for Human Activity Monitoring : A Review,” vol. 15, no. 3, pp. 1321–1330, 2015.

[81] N. Alshurafa, S. Member, and H. Kalantarian, “Recognition of Nutrition Intake Using Time-Frequency Decomposition in a Wearable Necklace Using a Piezoelectric Sensor,” *IEEE Sens. J.*, vol. 15, no. 7, pp. 3909–3916, 2015.

[82] C. Barrios, Y. Motai, and D. Huston, “Trajectory estimations using smartphones,” *IEEE Trans. Ind. Electron.*, vol. 62, no. 12, pp. 7901–7910, 2015.

[83] A. Almagambetov and S. Velipasalar, “Autonomous tracking of vehicle taillights and alert

signal detection by embedded smart cameras," *Distrib. Embed. Smart Cameras Archit. Des. Appl.*, vol. 62, no. 6, pp. 121–150, 2014.

[84] K. Wang, X. Qiu, S. Guo, and F. Qi, "Mechanism for Overhead Transmission Line in Smart Grid," *IEEE Sens. J.*, vol. 15, no. 3, pp. 1982–1991, 2015.

[85] Y.-J. Kim, D. Ha, W. J. Chappell, and P. P. Irazoqui, "Selective Wireless Power Transfer for Smart Power Distribution in a Miniature-Sized Multiple-Receiver System," *IEEE Trans. Ind. Electron.*, vol. 63, no. 3, pp. 1853–1862, 2016.

[86] Y. Zhang, Y. Gu, V. Vlatkovic, and X. Wang, "Progress of Smart Sensor and Smart Sensor Networks," in *IEEE 5th world congress on intelligent control and automation*, 2004.

[87] T. Ahmadi Tameh, M. Sawan, and R. Kashyap, "A Smart Optical Rotary Sensor for Pilot Input Control Applications," in *Advanced Photonics, Vancouver, Canada*, 2016.

[88] S. O. Kasap, "Optoelectronics and Photonics: Principles and Practices," 2001.

[89] S. W. Smith, "Moving Average Filters," in *The Scientist and Engineer's Guide to Digital Signal Processing*, 1991.

[90] T. Ahmadi Tameh, M. Sawan, and R. Kashyap, "Smart Integrated Optical Rotation Sensor Incorporating a Fly-by-Wire Control System," *Submitt. to IEEE Trans. Ind. Electron.*, 2017.

[91] T. Ahmadi Tameh, M. Sawan, and R. Kashyap, "Prototype optical rotation sensor using small optoelectronic devices," in *7th International Conference on Optical, Optoelectronic and Photonic Materials and Applications (ICOOPMA), Montreal, Canada*, 2016.

[92] T. Ahmadi Tameh, M. Sawan, and R. Kashyap, "Fly-By-Wire Flight Control Smart Optical Rotary Sensor for Aircrafts," in *Photonic North*, 2016.

[93] A. Morales and A. Duran, "Sol-gel protection of front surface silver and aluminum mirrors," *J. Sol-Gel Sci. Technol.*, vol. 457, no. 8, pp. 451–457, 1997.

[94] T. Ahmadi Tameh, M. Sawan, and R. Kashyap, "Optical sensors for fly-by-light flight control system," in *Avionics And Vehicle Fiber-Optics And Photonics (AVFOP) Conference, Long Beach, USA*, 2016.

[95] A. a M. Saleh and J. M. Simmons, "All-Optical Networking - Evolution , Benefits , Challenges , and Future Vision," *Proc. IEEE*, 2012.

[96] D. E. Anderson and M. W. Beranek, "777 Optical LAN Technology Review," in *Electronic components and technology*, 1998.

[97] J. W. Ramsey, "Boeing 787: Integration's Next Step," 2005.

[98] J. Barton, M. Mašanović, and L. A. Johansson, "Tunable transceiver technologies for avionics applications," in *2012 IEEE Avionics, Fiber- Optics and Photonics Technology (AVFOP) Conference*, 2012.

[99] D. W. Prather, J. Murakowski, J. Garrett, C. Schuetz, and S. Shi, "Emerging millimeter wave photonics devices and integration platforms for avionic application," in *Avionics And Vehicle Fiber-Optics And Photonics (AVFOP) Conference,* 2014.

[100] W. Lyloc and D. C. Pattison, "Fly by wire or fly by light control system with manuel override," 1993.

[101] J. r. Todd, "Fly-by-light flight control system developement for transport aircraft," in *IEEE Digital Avionics Systems Conference,* 1996.

[102] Flightglobal: Aviation and Aerospace News, "Fly-by-light EC135 helicopter makes first flight," 2002. [Online]. Available: https://www.flightglobal.com/news/articles/fly-by-light-ec135-helicopter-makes-first-flight-142313/.

[103] SAE, "Aerospace Fly-by-Light Actuation Systems," *2014*. [Online]. Available: http://standards.sae.org/air4982a/.

[104] I. García, J. Zubia, G. Durana, G. Aldabaldetreku, M. A. Illarramendi, and J. Villatoro, "Optical Fiber Sensors for Aircraft Structural Health Monitoring.," *Sensors (Basel).*, vol. 15, no. 7, pp. 15494–519, 2015.

[105] J.-H. Kim, Y. Park, Y.-Y. Kim, P. Shrestha, and C.-G. Kim, "Aircraft health and usage monitoring system for in-flight strain measurement of a wing structure," *Smart Mater. Struct.*, vol. 24, no. 10, pp. 1–12, 2015.

[106] D. Barazanchy, M. Martinez, B. Rocha, and M. Yanishevsky, "A Hybrid Structural Health Monitoring System for the Detection and Localization of Damage in Composite Structures," *J. Sensors*, pp. 1–10, 2014.

[107] V. Kumar, B. C. Choudhary, and U. K. Tiwari, "FBG Temperature Sensor for Avionics Display," *Adv. Aerosp. Sci. Appl.*, vol. 3, no. 1, pp. 1–11, 2013.

[108] D. Gahan, S. Fasham, and A. Harpin, "High temperature fiber optic pressure sensors for engine dynamics and health monitoring," in *IEEE Avionics, Fiber-Optics and Photonics Technology (AVFOP) Conference*, 2009.

[109] T. Invited, "Sensor application opportunities for aerospace propulsion systems," in *IEEE Avionics, Fiber-Optics and Photonics Technology (AVFOP) Conference*, 2009.

APPENDIX A – OPTICAL SENSORS FOR FBL-FCS

Introduction: In 1990, telecommunication industry started looking for a network connection in the optical domain from its source to its destination and thus removing the intermediate electronics [95]. The all-optical network implemented in 2000 has achieved a great saving in cost and power consumption although its vision is not exactly the same as a quarter of a century ago [95]. In 1993, FBL was introduced in aerospace industry intending to reduce the weight of aircraft, obtain immunity to EMI, and provide a much broader transmission spectrum. Around the same time (Boeing in1995 and Airbus before 1987), FBW airplanes were implemented in widespread by Boeing and Airbus. In fact, when telecommunication industry was immigrating to all-optical network, aerospace industry was migrating from mechanical system to wired system while investigating optical systems too as shown in Figure A.1. The trend is expected to continue migration from wire based systems to optical fiber systems. Even, the migration is likely to happen from the mechanical system directly to optical fiber systems by bypassing FBW systems. The research is still ongoing to establish requirements and standards of optical systems in avionic.

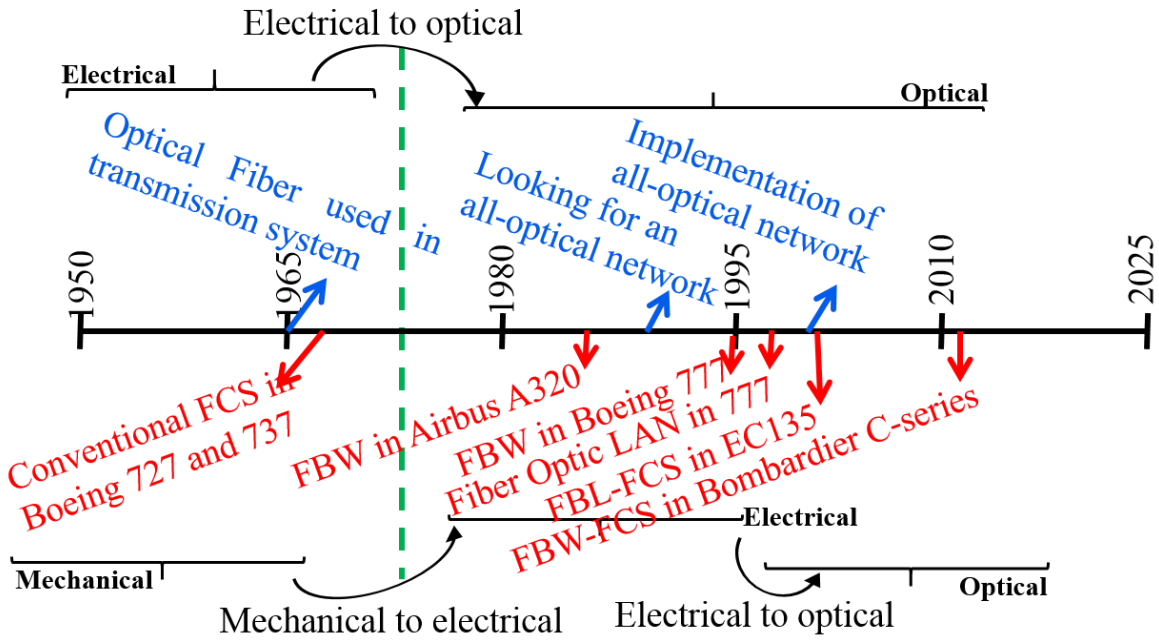

Figure A.1 : Comparison of migration of telecommunication and aerospace industries from mechanical systems to electrical systems and finally to optical systems

Ongoing applications of the optical fiber in avionic system: Fiber optic based local area networks were first implemented in Boeing 777 for onboard data communication in 1998. This brought the immense benefits of fiber optics, including immunity to EMI, reduced fire hazard, and compactness with reduced weight [96]. Additionally, the Boeing 787 Dreamliner has a fiber optic backbone containing several fiber links connecting various systems that need to communicate with each other [97]. Optics could be used not only in data communication among systems in the aircraft [98], [99] but also for various sensing and monitoring systems such as FCS.

The concept of FBL-FCS was first proposed in 1993 [100]. In 1996, McDonnell Douglas introduced FBL-FCS in the development program of the FBL advanced system hardware (FLASH) [101]. In 2002, Airbus helicopter (formerly Euro-copter Group) conducted the first flight of an EC135 based on an optical fiber control system, according to the report of Flightglobal news [102]. In 2014, Aerospace Information Report reported the FBL technology for controlling hydraulically operated air actuators [103]. This report does not establish standards but it was intended to provide a baseline or foundation for standards development for future FBL-FCS.

In the next section, the optical monitoring systems for various applications in the aircraft proposed in the literature are studied. Moreover, an optical rotary sensor for displacement measurement of flight control surfaces in FBL-FCS is proposed.

FBL aircraft: Figure A.2 shows an FBL aircraft system in which not only the backbone network is based on optical fiber, but also various systems are optical which could be connected to the optical network and consequently to the flight control computer (FCC). For example, a structural health monitoring system based on distributed optical fiber sensors could be connected directly to the fiber optic backbone network. In this system, fiber Bragg grating (FBG) sensors embedded in the wing could be used for health monitoring of the aircraft body [42], [104]–[106]. When an external force is applied to the wing of an aircraft, an FBG senses a change in strain. Hence, the Bragg grating in the wing is deformed resulting in a change in the reflected Bragg wavelength. In addition, distributed FBG sensors could be used for temperature sensing as the Bragg wavelength is proportional to the applied temperature [107]. Besides, other optical sensors resistant to high temperatures could be used for aircraft engine control [108], [109]. The strain sensing mechanism can be a Fabry-Perot interferometer in which a cavity is formed in a crystal sapphire membrane

with the melting point of 2053ºC. The applied pressure changes the cavity length and consequently is encoded into the intensity of reflected light.

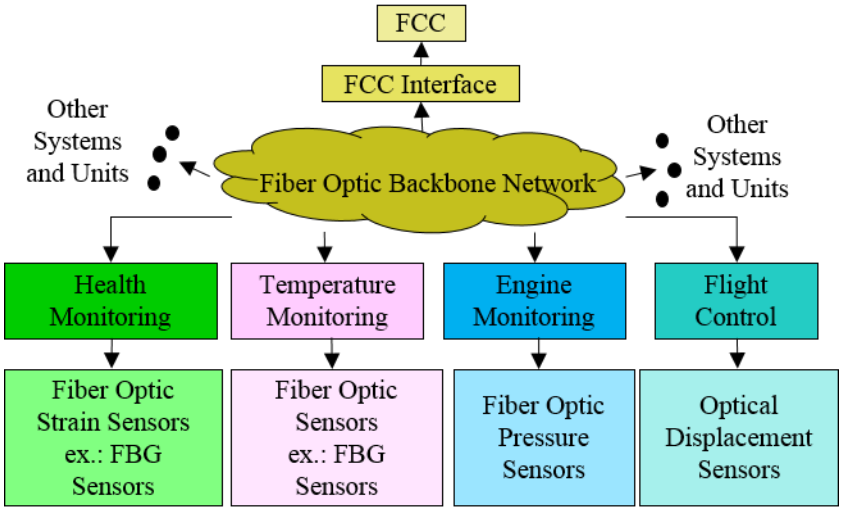

Figure A.2: All-optical aircraft including a fiber optic backbone network and monitoring systems. FCC: Fight Control Computer, Fiber Bragg Grating

FBL FCS: Another system in the aircraft which could be optical is the FCS. This system in the aircraft must control the actuators in flight control surfaces to adjust the aircraft's attitude in relation to the three axes: yaw, roll, and pitch [1]. The captain commands (via inceptors in the cockpit, such as sidesticks, conventional columns-wheels, rudder pedals, spoiler handle, and flap handle, etc.) are sent to the FCC and accordingly to the actuators in the wings or tail of the aircraft to adjust the position of flight control surfaces. Displacement sensors are needed to send the position of flight control surfaces to the FCC. The FCS as mechanical in conventional aircraft in which a system of cables and pulleys were used to transfer the captain's commands from the cockpit to the actuator in the flight control surfaces. Current aircraft with the most advanced technology use FBW where the mechanical system has been replaced by an electrical system and the signals are sent and received via wires rather than cables. Future aircraft are likely to migrate to the FBL method as fiber optics technology has met with overall approval in the telecommunications field.

In an FBW control system, signals between flight control surface sensors and the FCC are transmitted via wires while in FBL control systems, control signals are sent and received via optical fibers. Currently, rotary/linear variable differential transformer (RVDT/LVDT) are used in FBW-

FCS as depicted in Figure A.3 (a). To migrate from FBW-FCS to FBL-FCS, it would be significantly advantageous if the electrical sensor is replaced by an optical sensor [17] as shown in Figure A.3 (b). Hence, the optical signal in the output of the optical sensing system would be sent to the fiber optic backbone network without the need for electrical to optical conversion. The advantages of fully passive FBL control systems include immunity to EMI beside the significant weight and size reduction which will enable the upcoming development of demanding FCS.

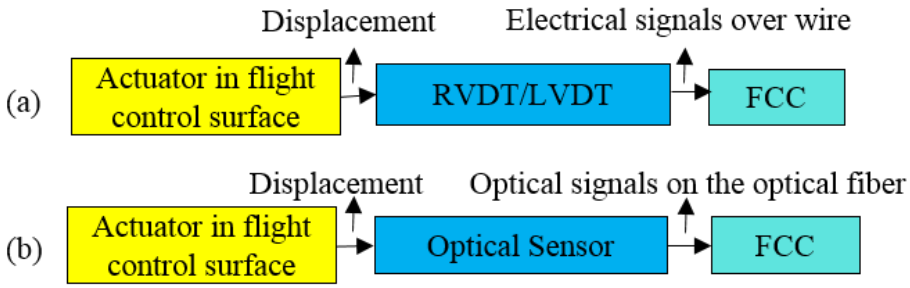

Figure A.3: Migration from (a) FBW-FCS to (b) FBL-FCS

Conclusions on this recommendation: Early aircraft employed conventional methods of mechanical/hydro-mechanical FCSs. Current aircraft with the highest technology are using FBW-FCS in which the mechanical system was replaced by electrical system and the signals are sent and received via wires rather than cables. Future aircraft are likely to migrate to fly-by-light (FBL) method [7] as fiber optics technology has met with overall approval in the telecommunications field. The advantages of FBL system versus FBW system include immunity to EMI, a much broader transmission spectrum which will enable future development of demanding flight control and mission systems, and low weight.

Until now, optical networks have been implemented inside the aircraft to connect different systems. In this recommendation, we presented that apart from the optical networks, several monitoring and controlling system in the aircraft could be optical. This helps the avionic industry to make lighter aircraft, immune to EMI, with no spark hazard.

This work was published in **[94]**.

APPENDIX B – LIST OF PUBLICATIONS & AWARDS

Journal papers

[J1] **T. Ahmadi Tameh**, M. Sawan, and R. Kashyap, "Smart Integrated Optical Rotation Sensor Incorporating a Fly-by-Wire Control System," submitted to *IEEE Trans. On Ind. Electron. J.*

[J2] **T. Ahmadi Tameh**, R. Kashyap, and M. Sawan, "Self-referenced broad range optical rotation sensor for flight control applications," submitted to *IEEE Sens. J.*

[J3] **T. Ahmadi Tameh**, M. Sawan, and R. Kashyap, "Novel Analog Ratio-Metric Optical Rotary Encoder for Avionic Applications," *IEEE Sens. J.*, vol. 16, no. July, pp. 6586–6595, 2016.

Conference papers

[C1] **T. Ahmadi Tameh**, M. Sawan, and R. Kashyap, "Analog optical rotary encoders: operating range-sensitivity trade-off," submitted to *Photonics North*, Ottawa,Canada, 2017.

[C2] **T. Ahmadi Tameh**, M. Sawan, and R. Kashyap, "Optical sensors for fly-by-light flight control systems," IEEE Avionics and vehicle fiber-optic and photonics (AVFOP) conference, California, USA, 2016.

[C3] **T. Ahmadi Tameh**, M. Sawan, and R. Kashyap, "A Smart Optical Rotary Sensor for Pilot Input Control Applications," in Advanced Photonics, Vancouver, Canada, 2016.

[C4] **T. Ahmadi Tameh**, M. Sawan, and R. Kashyap, "Prototype optical rotation sensor using small optoelectronic devices," in 7th International Conference on Optical, Optoelectronic and Photonic Materials, and Applications, ICOOPMA, Montreal, Canada, 2016.

[C5] **T. Ahmadi Tameh**, M. Sawan, and R. Kashyap, "Fly-By-Wire Flight Control Smart Optical Rotary Sensor for Aircraft" in Photonic North, Quebec City, Canada, 2016.

[C6] **T. Ahmadi Tameh**, M. Sawan, and R. Kashyap, "Self-Referencing Ratio-Metric Optical Rotation Sensor for Avionic Application," in *Advanced Photonics*, Barcelona, Spain, 2014.

Awards

[A1] NSERC-CREATE Integrated Sensor Systems (ISS) Graduate Training Program Award for two years, starting September 2013.

[A1] Winner of second prize of photo competition research project at Winter Networking Event of NSERC-CREATE Integrated Sensor Systems (ISS) Graduate Training Program at McGill University.